Fall 2014

Ultrashort laser pulse-matter interaction: Fundamentals and early stage plasma dynamics

Xin Zhao
Purdue University

Graduate School Form 30
(Revised 08/14)

PURDUE UNIVERSITY
GRADUATE SCHOOL
Thesis/Dissertation Acceptance

This is to certify that the thesis/dissertation prepared

By Xin Zhao

Entitled
ULTRASHORT LASER PULSE-MATTER INTERACTION: FUNDAMENTALS AND EARLY STAGE PLASMA DYNAMICS

For the degree of Doctor of Philosophy

Is approved by the final examining committee:

Yung C. Shin

Andrew M. Weiner

Galen B. King

Xiulin Ruan

To the best of my knowledge and as understood by the student in the Thesis/Dissertation Agreement, Publication Delay, and Certification/Disclaimer (Graduate School Form 32), this thesis/dissertation adheres to the provisions of Purdue University's "Policy on Integrity in Research" and the use of copyrighted material.

Yung C. Shin

Approved by Major Professor(s): _____

_____

Approved by: Ganesh Subbarayan 11/25/2014

Head of the Department Graduate Program Date

ULTRASHORT LASER PULSE-MATTER INTERACTION: FUNDAMENTALS AND EARLY STAGE PLASMA DYNAMICS

A Dissertation

Submitted to the Faculty

of

Purdue University

by

Xin Zhao

In Partial Fulfillment of the

Requirements for the Degree

of

Doctor of Philosophy

December 2014

Purdue University

West Lafayette, Indiana

Dedicated to my family

ACKNOWLEDGEMENTS

I would like to express my sincere gratitude to my academic adviser, Prof. Yung C. Shin, for his valuable advice, effective guidance, passionate encouragement, and kind support during my Ph.D study at Purdue. I also would like to thank Prof. Galen B. King, Prof. Andrew M. Weiner, and Prof. Xiulin Ruan for serving on my committee, with all my heart for their great help and insight for my study.

I am also thankful to my collaborators, Dr. Wenquan Hu, Dr. Alessandro Fortunato, Yunfeng Cao, and Qiong Nian, who worked together with me on different projects and inspired me by fruitful discussions.

I am very grateful to my other lab mates, Wenda Tan, Shaoyi Wen, Tylor Davis, Neil Bailey, Xiaoyang Ye, and so many other persons, who enriched my life at Purdue and, gave me a lot of help in many aspects.

Finally, I want to deeply thank my family, for their selfless love, support, and encouragement during my Ph.D study and in my whole life.

TABLE OF CONTENTS

Page

Page

Page

LIST OF TABLES

LIST OF FIGURES

Figure Page

Figure Page

Figure Page

Figure Page

Figure Page

Figure Page

ABSTRACT

Zhao, Xin, Ph.D., Purdue University, December 2014. Ultrashort Laser Pulse-Matter interaction: Fundamentals and Early Stage Plasma Dynamics. Major Professor: Shin, Yung C.

Despite extensive studies for many years, the detailed mechanisms of ultrashort laser pulse (USLP)-matter interaction are still not fully understood and further fundamental investigation is required. This study seeks to provide an improved understanding of the USLP-material interaction by both theoretical and experimental investigations and to find ways to enhance laser energy coupling with different materials.

A two-dimensional comprehensive hydrodynamic model for USLP ablation of metals and semiconductors is developed in this study. The model comprises a two-temperature model and a hydrodynamic model supplemented with a quotidian equation of state model, considering the relevant multiphysical phenomena during the laser-matter interaction. The models are capable of simulating the ablation process and the resultant plasma evolution in a wide range of laser intensity, and are valid both in air and in vacuum.

The developed model is applied to investigate the ablation of metals in various laser intensity ranges. The dependence of ablation rates on laser intensity in air and in vacuum is studied by the model and validated against the experimental data in literature. It is revealed that there appears to be a sudden increase of the ablation rate in the high intensity range in vacuum, due to switching of the dominant absorption mechanisms. On the other hand, much lower ablation efficiency at high laser intensity in air is caused by the strong early plasma absorption of incident laser beam energy. The evolutions of both

early plasma and plume plasma are measured by a shadowgraphic technique and a direct fluorescence method, respectively, and are analyzed by the numerical simulation. It is found that the electron emission process greatly affects the surface electron temperature.

The femtosecond laser ablation of silicon in air is also investigated by the integrated model. The numerical analysis results are validated and supplemented by the experimental measurements for the ablation rate and early plasma dynamics over a wide laser intensity range. It is found that ablation efficiency first increases with laser intensity, and then begins to drop in the high laser intensity range, because of the early plasma absorption of the laser beam energy. By investigating the ion expansion speed, electric field distribution, and velocity distribution of different ions, the occurrence of Coulomb explosion (CE) is demonstrated during the ablation of silicon at high laser intensity, which leads to a fast ion ejection from the target surface, thereby increasing the material removal rate at the early stage.

Next, double-pulse (DP) ablation of silicon is investigated by an integrated atomistic model, combined by molecular dynamics (MD), Monte Carlo (MC), particle-in-cell (PIC), and beam propagation (BP) methods. The plasma emission spectrum is measured by a spectrometer to calculate the plasma temperature and electron number density. It is observed that the double-pulse ablation could significantly increase the ablation rate of silicon, which is totally different from the case of metals. Electronic excitation and metallic transition of melted silicon are revealed to be responsible reasons of ablation enhancement at ultrashort (below 1 ps) and long (1 ps to 10 ps) pulse delays, respectively. At even longer pulse delay (over 20 ps), the plasma temperature and electron number density can be effectively increased, accompanied by the ablation rate suppression. The spatial analysis of plasma temperature shows that the second pulse energy is mainly absorbed by the front portion of the plasma, where the temperature is increased the most. The plasma reheating leads to a faster expansion of the plasma.

1. INTRODUCTION

Ultrashort laser pulse-matter interaction has attracted considerable attention in the past few decades, due to its competitive applications in the fields of precision micromachining, ultrafast dynamics, laser-induced breakdown spectroscopy, fast chemical reactions, ultrafast dynamics, and etc. Ultrashort laser pulses (USLP) refer to the laser pulses with the pulse duration in the order of femtosecond (1 fs == 10^{-15} s) to picosecond (1 ps = 10^{-12} s). Compared with the short (pulse duration in the order of nanosecond, 1 ns = 10^{-9} s) and long (pulse duration in the order of microsecond, 1 ms = 10^{-6} s) laser pulses, USLP shows unique characteristics and attractive advantages during its interaction with materials, including reduced heat affected zones by rapid pulse energy deposition, ignition of ultrafast electron dynamics, and fast creation of strong plasma. Therefore, it is very important to understand the underlying physics during the laser-material interaction, in order to improve the existing applications and develop new ones. However, despite the extensive studies in this realm, the physical mechanisms in different conditions are still not clearly understood due to the involved complicated multiphysical phenomena. Further studies are necessary to investigate the fundamental mechanisms of the USLP-matter interaction.

1.1 Overview of Ultrashort Laser-Matter Interaction

It has been observed and widely studied that the concentrated light energy could affect and ablate the irradiated material considerably. The invention of USLP provides a new era of fundamental research of unique physics mechanisms, as well as new regimes of promising applications. The interaction between materials and USLP is very different from that of longer laser pulses, and new physical mechanisms and unique characteristics are involved. First, USLP typically has the pulse duration shorter than the duration of

major relaxation processes, including the electron-lattice energy transfer, heat diffusion and hydrodynamics. It is shown in Figure 1.1 (Rethfeld et al., 2004) that electron heating and excitation occur in the range of femtoseconds. The electron-lattice heating and the lattice relaxation take place in the picosecond regime, after the end of laser pulse. The time scale of the resultant material removal could lasts up to the nanosecond regime. Therefore, the salient feature of USLP-matter interaction is that the laser pulses only excite the electrons inside the materials, leaving the lattice cool until the electron-lattice heat transfer starts. The extremely short period of laser irradiation promises a localized heat affected zone in the target material, leading to a precisely controlled ablated area, less melting area, and clean edge and surface. Chichkov et al. (1996) demonstrated the advantages of the USLP ablation over that of longer laser pulses. As illustrated in Figure 1.2a, the molten materials are obviously observed in nanosecond laser ablation, where the drilled hole has a rough surface and edge. In case of femtosecond laser ablation in Figure 1.2b, the drilled hole shows a sharp edge, a smooth side wall, and a very clean surface.

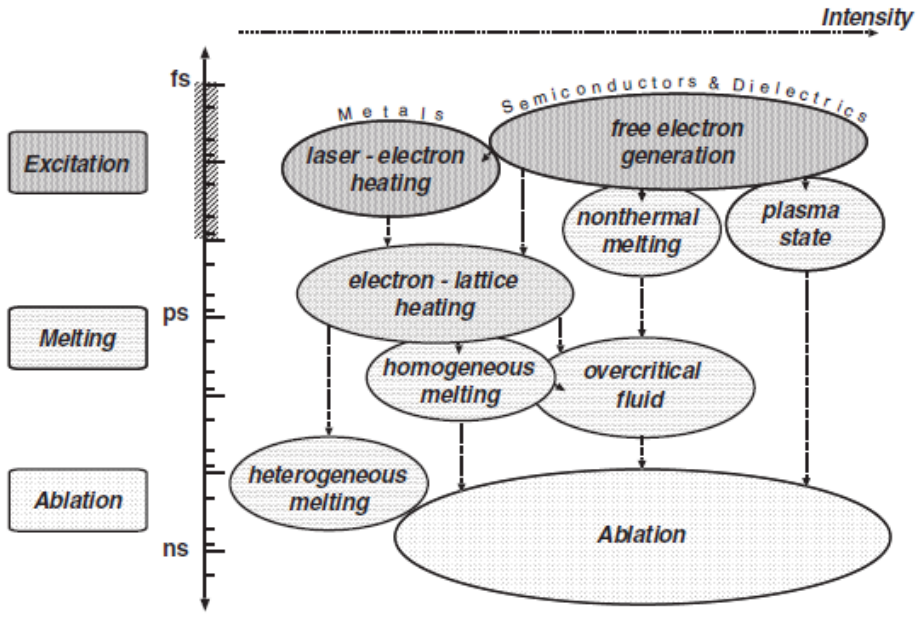

Figure 1.1 Typical timescales and intensity ranges of the phenomena during and after irradiation of a solid with an ultrashort laser pulse of about 100 fs duration. (Rethfeld et al., 2004)

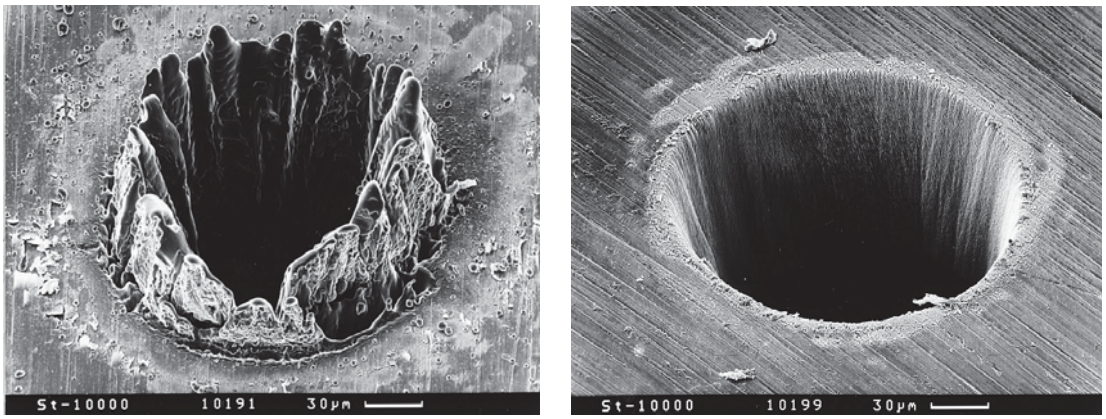

a) Nanosecond laser ablation b) Femtosecond laser ablation

Figure 1.2 SEM photographs of holes drilled in a 100 μm thick steel foil with a) nanosecond laser ablation, pulse duration: 3.3 ns, fluence: 4.2 J/cm2, and wavelength 780 nm, and b) femtosecond laser ablation, pulse duration: 200 fs, fluence: 0.5 J/cm^2, and wavelength 780 nm. (Chichkov et al., 1996)

Second, the extremely short pulse duration of USLP generates extremely high power density. The power density of USLP is typically higher than 10^{12} W/cm^2, and could possibly exceed 10^{20} W/cm^2. It is high enough to trigger nonlinear absorption, when a bonded electron can absorb several photons simultaneously, and then get excited to be free. With this unique feature, USLP can be used to process transparent materials directly even with a long wavelength (near infrared). USLP irradiation can be used to fabricate a wide variety of optical components, such as waveguides (Davis et al., 1996, Miura et al., 1997), power splitters (Nolte et al., 2003), couplers (Minoshima et al., 2002), and Bragg gratings (Marshall et al., 2006). It can also be used to drill microchannels for micro-fluidic application in micro-total analysis systems (μ-TAS) (Whitesides, 2006; Psaltis et al., 2006; Craighead; 2006, Zhao et al., 2010).

The USLP-matter interaction is a complicated process, involving multi-physical mechanisms. The schematic description of the interaction process is illustrated in Figure 1.3. When materials are irradiated by an USLP, the laser beam energy is mainly absorbed by electrons inside the target. Three major mechanisms dominate the absorption process: inverse bremsstrahlung absorption (IB), multiphoton absorption (MP), and collisionless absorption. By absorbing the incident laser beam energy, the electrons inside the target

are heated to an extremely high temperature ($\sim 10^4$ K) in a very short amount of time. Since the electron relaxation time (~10 fs) (Afanasiev et al., 2002b; Huttner, 2009) is much shorter than the electron–phonon relaxation time (10–100 ps) (Vinogradov and Faĭzullov, 1977; Itina et al., 2004; Colombier et al., 2005), the lattice remains cool during this process. When the electrons near the target surface gain enough energy, either from direct laser absorption or from coupling with other electrons, it is possible for them to overcome the attraction of the lattice and escape from the target surface (Bechtel et al., 1977; Mao et al., 1998; Rethfeld et al., 2004; Bulgakova et al., 2004; Bulgakova et al., 2005a; Bulgakova et al., 2005b). The ejected hot electrons are energetic enough to ionize the ambient gas, forming an early stage plasma in several or tens of femtoseconds (Bulgakova et al., 2007).

The generation of early stage plasma plays an important role in the USLP–material interaction process, which will reduce the energy deposited into the target by absorbing laser energy, and interact with the target during its expansion. The energy of hot electrons will be transferred to the lattice by electron–phonon coupling, finally reaching local thermal equilibrium in 10–100 ps (Vinogradov and Faĭzullov, 1977; Afanasiev et al., 2002b; Itina et al., 2004; Colombier et al., 2005; Huttner, 2009). The chemical bonds among atoms will be broken at a high enough temperature, and the atoms and ions near the surface will escape from the target bulk, forming the plume plasma. The material removal process can be driven either by thermal ablation, such as spallation, phase explosion, critical-point phase separation, fragmentation, and vaporization, or by non-thermal mechanisms such as Coulomb explosion. For ultrashort laser ablation processes, the laser absorption by the plume plasma can be neglected, since it is usually generated after the end of laser pulse.

To fully understand the USLP ablation of matters, all the physical mechanisms mentioned above should be considered and studied under different conditions. Numerous theoretical and experimental investigations have been conducted on USLP ablation processes of various kinds of materials. The following sections will review the previous studies in laser absorption, laser ablation mechanisms, and plasma dynamics, including both physical mechanisms and numerical model developments.

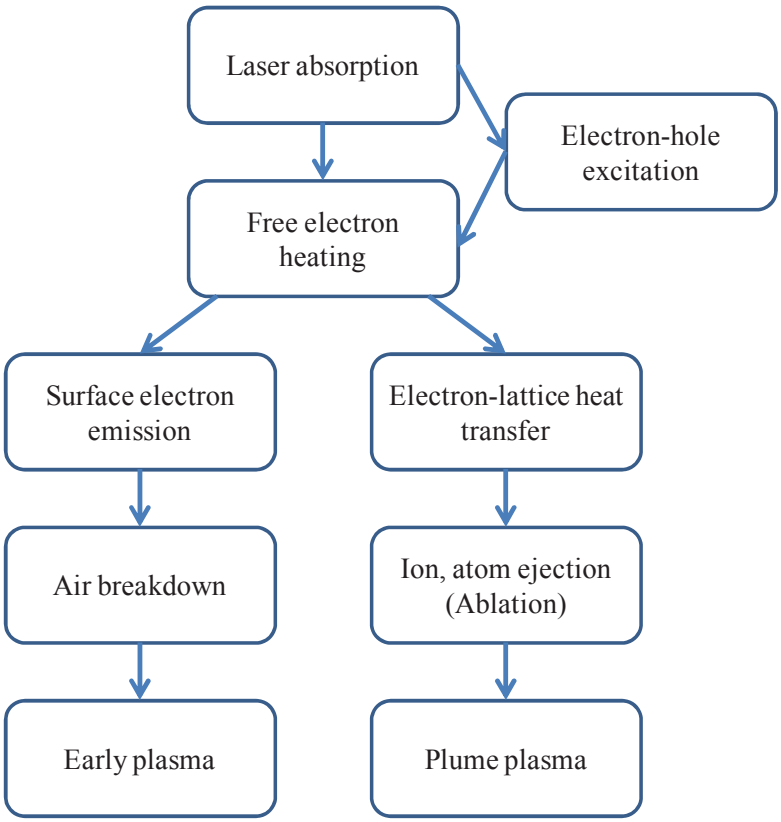

Figure 1.3 Schematic diagram of the USLP-matter interaction process.

1.2 Laser Absorption

Laser absorption is the first step of USLP ablation, and plays a key role in the whole process. The absorption efficiency significantly affects the ablation rate and the crater shape. Due to the much smaller mass of electrons relative to the atoms, it is a good approximation to state that light is mainly absorbed by electrons. The absorption process can be attributed to three major mechanisms: inverse bremsstrahlung absorption (IB), multiphoton absorption (MP), and collisionless absorption.

1.2.1 Inverse Bremsstrahlung Absorption

IB is a fundamental mechanism in the heating and breakdown of materials by a laser beam. A free electron can gain energy by colliding with the bound electrons and lattice when wiggling in the oscillating laser field (Zel'dovich et al., 2002). This process is known as IB, as presented in Figure 1.4 (Sundaram and Mazur, 2002), where CB denotes conduction band, and VB refers to valance band. An electron in CB is considered as a free electron. It can absorb the energy of a photon and be excited to a higher energy level, during which collision with other particles is required by the conservation of momentum. This process is intraband absorption, since there is no band transition during the absorption process. Because of the existence of the sufficient free electrons, it is well accepted that IB works as the dominant absorption mechanism in USLP ablation of metals (Nolte et al., 1997; Furusawa et al., 1999; Afanasiev et al., 2002b; Nedialkov et al., 2005a; Yang et al, 2007; Kim and Na, 2007; Zavestovskaya et al., 2007). In semiconductors and insulators, IB is also involved after sufficient generation of free electrons by multiphoton excitation (Mao et al., 2004; Bulgakova et al., 2005b; Wu and Shin, 2009).

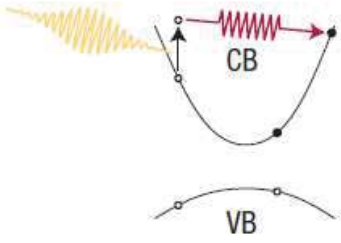

Figure 1.4. Schematic illustration of free carrier absorption (Sundaram and Mazur, 2002).

The physics and theory of IB have been extensively studied both experimentally (Price et al., 1995; Fisher et al., 2001; Agranat et al., 2007; Komarov et al., 2009) and theoretically (Seely and Harris, 1973; Eidmann et al., 2000; Fisher et al., 2001; Komarov et al., 2009). Its absorption rate can be calculated by the Drude model (Ginzburg, 1962;

Pedrotti et al., 1993; Vidal et al., 2001), which is proportional to the effective collision frequency υ_{eff} of electrons and ions. Eidmann et al. (2000) have shown via simulation that the effective collision frequency in aluminum first increases with the electron temperature to a peak value, and then starts to drop when the electron temperature further increases, as presented in Figure 1.5. The target is in cold solid state at low temperature (lower than Fermi temperature, denoted by v_{cold}), and gradually switches to a plasma state as the temperature increases (denoted by $v_{el\text{-}phonon}$). With a further rise of the temperature, the surface area of the target will become a hot plasma state (shown by $v_{spitzer}$), and the effective collision frequency starts decreasing with the temperature. In different temperature ranges, the collision processes between electrons and ions behaves quite differently, leading to a different collision frequency. Correspondingly, the absorptivity of aluminum is observed to change similarly with the collision frequency (Price et al., 1995), as shown in Figure 1.6. The absorptivity first rises with the incident laser intensity, and after the peak value, it gradually drops.

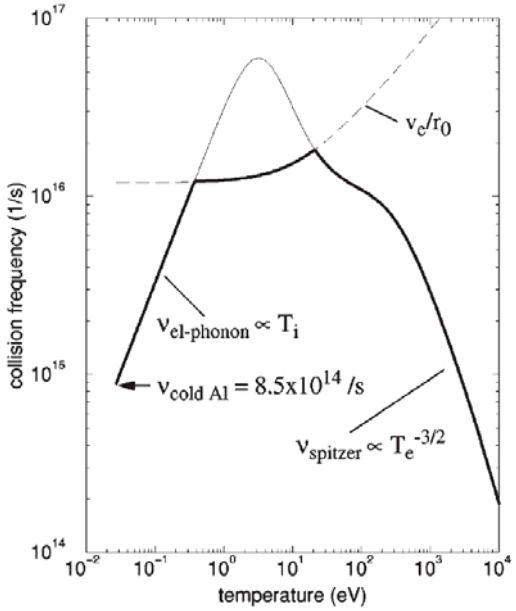

Figure 1.5. Collision frequency of solid Al as a function of the temperature T_e=T_i (thick solid line). The dashed line: the upper limit of the collision frequency (Eidmann et al., 2000).

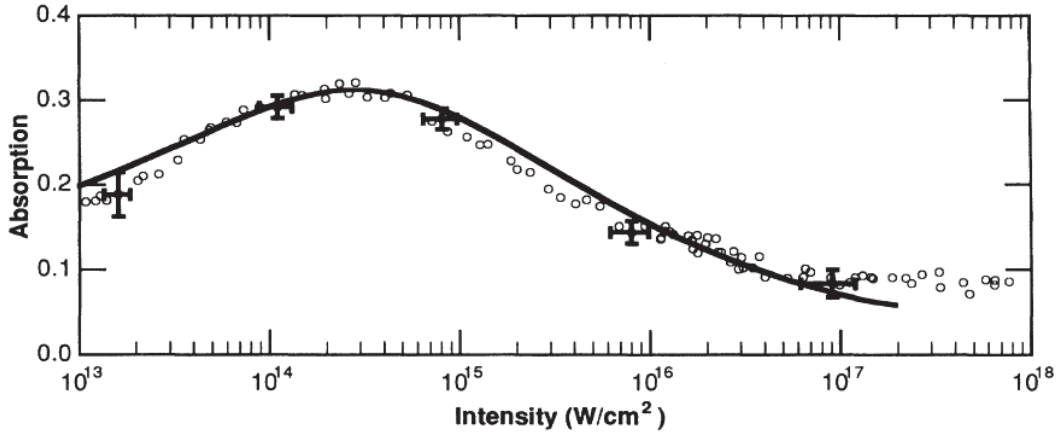

Figure 1.6. Absorption fraction vs peak laser intensity of aluminum. Wavelength: 400nm, pulse duration: 120fs (Price et al., 1995).

1.2.2 Multiphoton Absorption

Multiphoton absorption (MP) is an important absorption mechanism for bound electrons, the process of which is illustrated by Figure 1.7 (Sundaram and Mazur, 2002). When the photon energy is larger than the band gap, the bound electrons in valence band (VB) can directly absorb the light energy and be lifted to the free energy level (CB) (Figure 1.7 left). This process will be inhibited if the ionization potential or band gap is greater than the photon energy. Thus, some dielectric materials can not absorb light energy and appear to be transparent. However, at sufficiently high laser intensity as in the case of USLP–matter interaction, bound electrons of the transparent materials can be directly ionized by simultaneously absorbing several photons in the laser pulse (Figure 1.7 right). This process is called interband absorption because it involves the excitation from valance band to conduction band. Semiconductors and insulators lack free electrons for IB absorption at the early stage, and therefore, MP becomes crucially important, determining the breakdown threshold behavior (Apostolova and Hahn, 2000; Sudrie et al., 2002; Wan et al., 2011). The rate of n-photon absorption is proportional to I^n, where I is the laser intensity. The number of photons required is determined by the smallest n that satisfies the relation $n\hbar\omega \geq E_g$, where E_g is the bandgap energy of the material and

$\hbar\omega$ is the photon energy. Therefore, MP absorption rate will increase fast with the laser intensity, and is more important in the high intensity range.

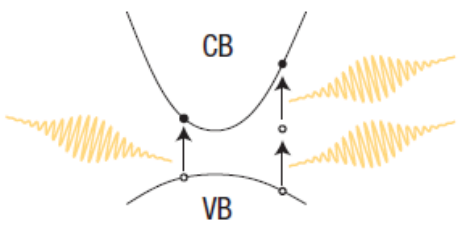

Figure 1.7. Schematic illustration of multiphoton absorption (Sundaram and Mazur, 2002).

MP is usually neglected in the ablation of metals, because of the existence of sufficient free electrons in normal state. However, it has been revealed by Guo et al. (2000) and Petek et al. (2000) that some normal or parallel band structures exist in metals. Fisher et al. (2001, 2005) reported that at low temperature (near room temperature), the interband absorption might also be important for metals. Figure 1.8 summarizes the contribution of interband and intraband absorption to the total AC conductivity of aluminum at different electron momentum relaxation rates (Fisher et al., 2001). The solid line represents the real part of the total conductivity ($\mathrm{Re}\{\sigma\}$), while the dashed line stands for the imaginary part of the conductivity ($\mathrm{Im}\{\sigma\}$). The dotted line denotes the intraband contribution to the conductivity ($\mathrm{Re}\{\sigma_{dr}\}$). The total AC conductivity is calculated as the sum of the interband and intraband absorption. By comparing the real parts of the conductivity, it can be seen that the contribution from interband is dominating at the low electron momentum relaxation rate, while it becomes negligible at the high relaxation rate. Since the electron relaxation rate generally increases with electron temperature, the conclusion could be drawn such that at low temperature, interband absorption dominates over the intraband absorption. As the temperature increases, the contribution from intraband absorption rises and becomes

more and more important. The interband absorption is inhibited at high temperatures because of the broadening of the absorption peak.

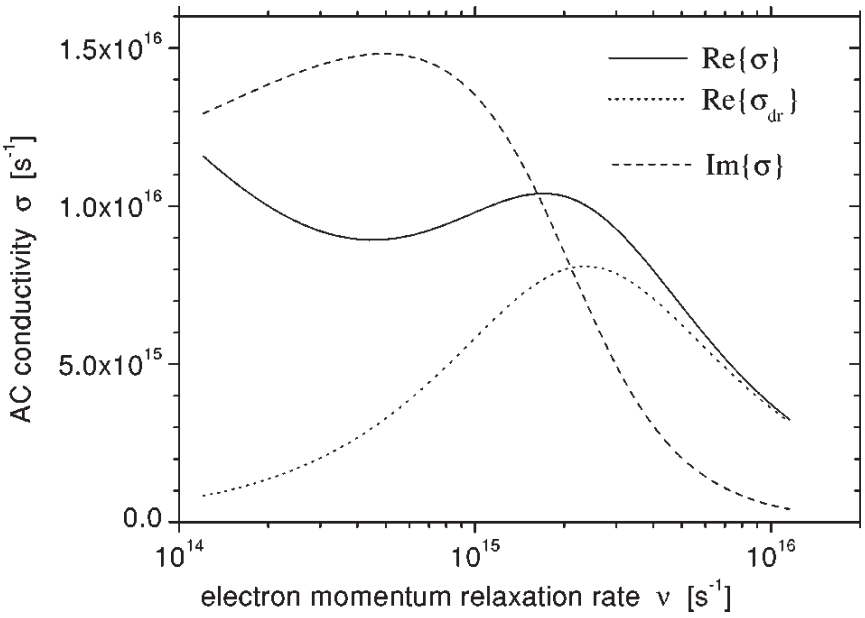

Figure 1.8. Total and intraband AC conductivity of aluminum at different electron relaxation rate (Fisher et al, 2001).

1.2.3 Collisionless Absorption

Collisionless absorption is the process where electrons directly absorb the laser beam energy without any collision process. When a laser beam is incident to an inhomogeneous plasma, the electric field's component along the plasma gradient will tend to drive the electrons to oscillate in this direction. The laser induced electric field creates resonant oscillations of the electrons, and excites the electrons to a high kinetic energy. It is an irreversible conversion of laser energy to electron kinetic energy, and this non-collisional absorption process is called resonance absorption (Gibbon and Bell, 1992). When electric field strength and the plasma gradient further increase, the electrons will be driven out of the target directly, while certain portion of them will be drawn back immediately, further transferring the kinetic energy to the target by colliding with other electrons, causing vacuum heating effect (Grimes et al., 1999). The initiation of two mechanisms depends

on the electron number gradient scale L^{-1}, which is estimated as: $L = \left| n_{e0} / \nabla n_e(z) \right|$, where n_e is the electron number density, and n_{e0} is the electron number density at room temperature (Fraenkel et al., 2000). The resonance absorption happens when the gradient is small (L is large), and the electrons are oscillating inside the target material. It was theoretically derived by Gibbon and Bell (1992) that when $L/\lambda>1$, the resonance absorption will be important, and when $L/\lambda<0.2$, the vacuum heating will be the dominant one, where λ is the laser wavelength. The occurrence of collisionless absorption requires very high laser intensity, and thus it is important in the high intensity range. It has been reported that for high intensity laser ablation, the total absorption predicted only by collisional absorption is underestimated compared to the experimental measurements, and it is deduced that the collisionless absorption is important in this range (Huttner, 1994, Gibbon and Bell, 1999; Komarov et al., 2009).

1.3 Laser Ablation Mechanism

Laser ablation refers to the material removal process due to the irradiation by laser pulses. An important feature of USLP-matter interaction is that the ablated area is of only a few hundred atomic layers per pulse, which relaxes within picoseconds after the excitation (Gamaly, 2011). Thus, the heat-affected-zone (HAZ) is limited into a small region, ensuring the high accuracy of the USLP ablation. Due to its great advantages, USLP ablation in high precision micromachining is one of the most promising applications of USLP-matter interaction. The ablation process is affected by the laser parameters, such as laser intensity, pulse duration, wavelength, and polarization. The experiments by Sokolowski-Tinten et al. (1998) have shown that different materials behave similarly under the irradiation by femtosecond pulses at fluences below the threshold for plasma formation. It is implied that some very general mechanisms are responsible for the material removal process. Two general ablation mechanisms are involved in USLP-matter interaction: thermal ablation and non-thermal ablation. At different ablation conditions, different ablation mechanisms will be dominant and thus the material ejection behavior is quite different.

1.3.1 Thermal Ablation

After absorbing incident laser beam energy, electrons will dissipate their energy by coupling with the local lattice atoms and ions. When the atoms gain enough energy, they can overcome the bonding energy and be ejected, leaving vacancies in the lattice. This material removal process due to the thermally induced high energy is called thermal ablation. Depending on laser pulse duration and laser fluence, different thermal ablation mechanisms can occur, and the ablation process undergo different thermodynamic trajectories. Figure 1.9 presents the typical thermodynamic trajectories of ns, ps, and fs laser ablation, summarized by Lorazo et al. (2003). The binodal curve (thin solid line) defines the area where liquid and vapor state could coexist, and the spinodal curve (dashed line) marks the zone where the homogeneous matter is metastable. The matter is in the state of supercooled vapor and superheated liquid in the left and right areas between binodal and spinodal curves, respectively. For ns laser ablation, the matter is heated slowly along the binodal curve until entering the metastable zone, triggering the ablation process (B→W). This process is called phase explosion (Miotello and Kelly, 1995; Sokolowski-Tinten et al, 1998). For ps laser ablation, the heating process is faster, while the expansion process is not fast enough. At low fluence, the target will cool down along binodal curve without entering the metastable zone (B→B'→W), and no material removal process takes place. The ablation will occur only when the target is heated above the critical point (CP, marked by cross) (B→V). For fs laser ablation, the system could undergo several thermodynamic trajectories, involving different ablation mechanisms. At low fluence, the target is rapidly heated into metastable zone (K→M), and phase explosion takes place. The maximum temperature is below CP. When the laser fluence increases, the target is first heated to a temperature above CP, and then adiabatically cooled into the metastable region (A→A'→W→Y). The heating process is isochoric and the target remains in solid density. The typical ablation in this region is critical point phase separation (Vidal et al., 2001; Cheng and Xu, 2005). At even higher fluence, the system is isochorically heated to an extremely high temperature, and the fast expansion leads to a breakup of the supercritical fluid (A→A"→U). Fragmentation (Perez and Lewis, 2002; Perez and Lewis, 2003; Perez and Lewis, 2004) is an important mechanisms

dominating in this regime. Figure 1.9 only provides a schematic description of the typical ablation process, and does not cover all the ablation mechanisms. Various ablation mechanisms have been proposed for fs laser ablation, such as spallation (Itzkan et al., 1995; Zhigilei and Garrison, 2000; Vidal et al., 2001; Perez and Lewis, 2002; Perez and Lewis, 2003), phase explosion (homogeneous nucleation) (Miotello and Kelly, 1995; Kelly and Miotello, 1996; Sokolowski-Tinten et al, 1998; Miotello and Kelly, 1999; Zhigilei and Garrison, 2000), critical point phase separation (Vidal et al., 2001; Cheng and Xu, 2005), fragmentation (Toxvaerd, 1998; Perez and Lewis, 2002; Perez and Lewis, 2003; Perez and Lewis, 2004), and vaporization (Perez and Lewis, 2003). Their occurrences strongly depend on the fluence of the incident laser pulse.

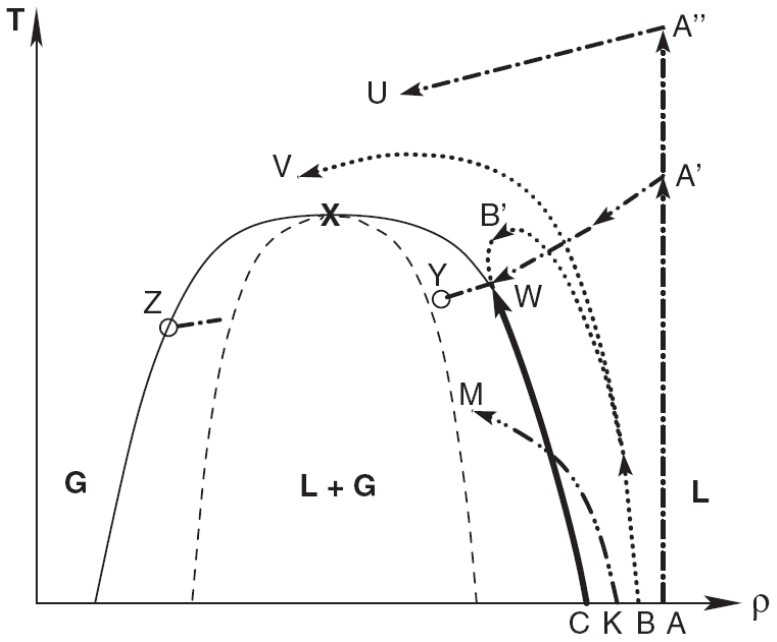

Figure 1.9. Thermodynamic trajectories of a hypothetical semiconductor or metal under fs (dashed-dotted line), ps (dotted line), and ns (thick solid line) laser irradiation. Thin solid line: binodal; dashed line: spinodal; cross: critical point. L: liquid; G: gas. Other capital letters refer to locations in the phase diagram. (Lorazo et al., 2003).

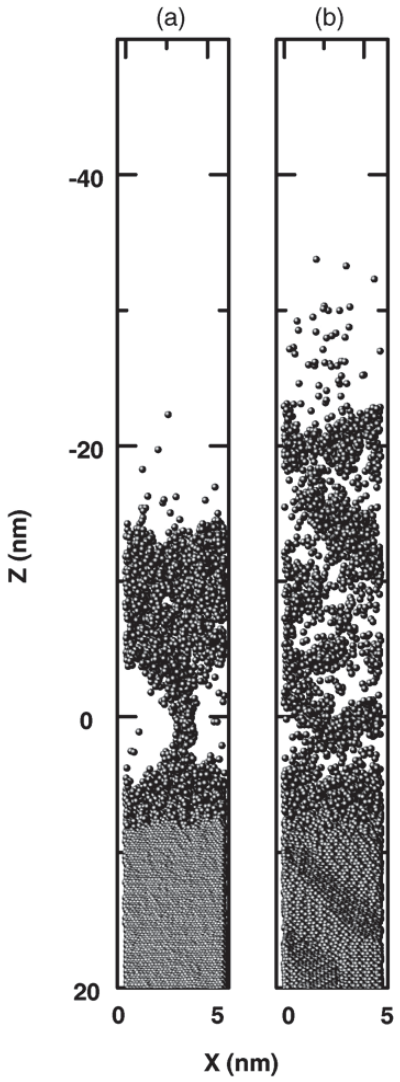

Figure 1.10. Snapshots of the atomic configuration in Al at 25 ps after the laser pulse onset: (a) laser fluence F = 0.2 J/cm^2 and (b) F = 0.5 J/cm^2. Laser wavelength is 800 nm, and pulse duration is 100 fs (Nedialkov et al., 2005b).

1.3.1.1 Spallation

Spallation is proposed to be the dominant ablation mechanism in the low laser fluence range (near ablation threshold) (Perez and Lewis, 2003; Nedialkov et al., 2005b). In this regime, the target temperature is usually below CP, but its heating generates a thermo-elastic stress. During the propagation into the bulk material, the thermo-elastic stress can cause the formation of voids and defects when its amplitude exceeds the matter bonding,

and trigger the consequent ablation of the material. Nedialkov et al. (2005b) studied the femtosecond ablation of aluminum at various laser fluences by molecular dynamics model (MD). The snapshots of the material removal process of aluminum at 25 ps at different laser fluences are presented in Figure 1.10. Figure 1.10 (a) shows the atoms evolution under the laser fluence near the ablation threshold (0.2 J/cm^2), where spallation is revealed to be dominating. The removed material is mainly composed of big clusters, which is the typical characteristic of the spallation. The breakdown occurs about 7 nm below the surface of the material, where the front of the stress is formed.

1.3.1.2 Phase Explosion

The absorption of laser beam energy leads to a heating of the target material. It could first change to liquid phase, and then be further heated into a state of superheated liquid, denoted by the area between binodal curve and spinodal curve in Figure 1.9. The expansion process will finally drive the system into the liquid-vapor metastable zone, where the homogeneous liquid state is no longer stable. It tends to overcome the activation barrier and nucleate in the gas state. The gas bubbles gradually form and the material is turned into a mixture of liquid droplets and vapor. This process is called phase explosion, also known as homogeneous nucleation. Figure 1.10 (b) reveals the atomic evolution during the phase explosion of aluminum. Instead of breaking directly at a certain depth, the material is removed homogeneously, consisting of small clusters and liquid droplets, which are much smaller than the cluster formed in spallation. It has been accepted that phase explosion also takes place in the low laser fluence range. However, different conclusions about its dominating range are given by different studies. The MD simulations by Perez and Lewis (2003) and Nedialkov et al. (2005b) found that the phase explosion dominates in the fluence range higher than that of spallation. On the contrary, the studies by Lorazo et al. (2003) and Hu et al. (2010) revealed that it would be dominant in a lower fluence range. This inconsistency could possibly be explained as follows. Phase explosion will occur once the matter enters into the liquid-vapor metastable region. As shown in Figure 1.9, it can be reached through several different thermodynamic trajectories, such as K→M (low fluence) and A→A'→W→Y (higher

fluence). Therefore, phase explosion can happen simultaneously with other ablation mechanisms at different laser fluences, dominating in different location and time scale.

1.3.1.3 Critical Point Phase Separation

When the laser fluence further increases, another mechanism becomes important, which is called critical point phase separation (CPPS). Its existence in ULSP ablation is first introduced by Vidal ea al. (2001) as follows. The target material is rapidly heated to a temperature above CP in a density of solid state, and then is pushed into the metastable region by crossing CP during fast expansion. During the cooling process, there appears to be a phase separation, splitting into an ablated vapor phase and an unablated solid/liquid phase, leading to the material removal process. Besides the involvement of phase separation, another difference between CPPS and phase explosion is that in CPPS, matter enters unstable zone during the cooling process, while it occurs during rapid heating process in phase explosion. CPPS mainly occurs at moderate laser fluence, and has been studied by Vidal et al. (2001) by using an HD model and by Hu et al. (2010) via an MD-MC model. Figure 1.11 shows the typical thermodynamic trajectories of cells at various depths in aluminum during ablation via CPPS, which are calculated by MD simulation by Vidal et al. (2001). The cells 50 and 54 are close to each other, and both pass through the CP during their cooling expansion. Cell 54 turns into the low density vapor phase after passing through the CP, while cell 50 turns into high density liquid phase, although it is deeper in the target. The phase separation of the adjacent materials leads to the multiple vapor and liquid irregular generation and the consequent material removal process. The ablated material contains vapor gas as well as some liquid droplets. It is observed by Vidal et al. (2001) that 15% of the ablated material is in liquid state. Figure 1.12 displays the material evolution and the corresponding density distribution with respect to time delay during ablation of Ni under the laser fluence of 1.0 J/cm^2 (Hu et al. 2010). Figure 1.12 (a) shows the material evolution at 21, 42, and 72 ps of time delay, and the material density distribution at the corresponding time is summarized in Figure 1.12 (b). At the time delay of 21 ps, the material layers above -20 nm are in vapor state with uniform densities, while the layers between −20 to 60 nm are liquid-vapor mixtures with gradually

changing number densities. Thereafter, more liquid layers are turned into vapor state, and the layers in different phases finally separate with each other at 72 ps, as shown in location 3 in Figure 1.12 (a). At this moment, violent oscillations of density are observed in the region between 0 to 10 nm, due to the generation and coexistence of bubbles and liquid droplets.

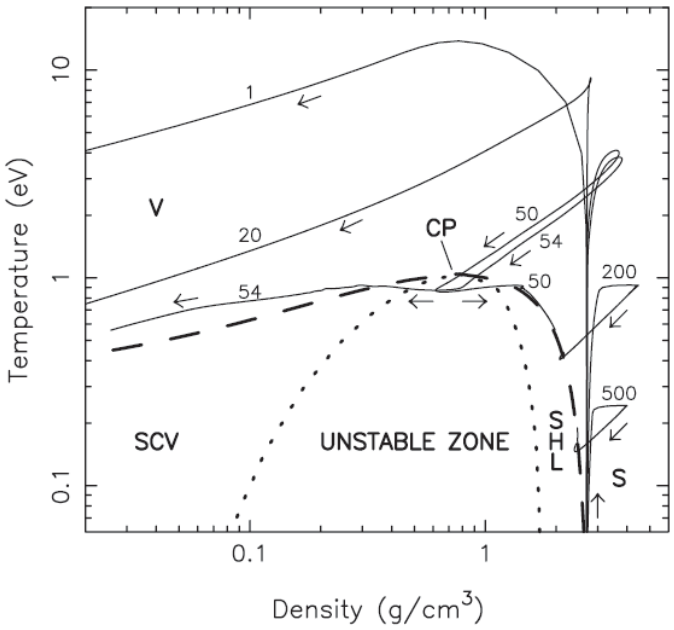

Figure 1.11. Trajectories of a few Lagrangian cells in the density-temperature plane. The total simulation time is 400 ps. The cells are numbered inward starting from the interface between the matter and the vacuum. Laser pulse has 500 fs, 1 μm, normal incidence, and 10 J/cm^2. Dashed curve: binodal; dotted curve: spinodal; SHL: superheated liquid; SCV: supercooled vapor; S: solid phase; V: vapor phase; CP: critical point. (Vidal et al., 2001).

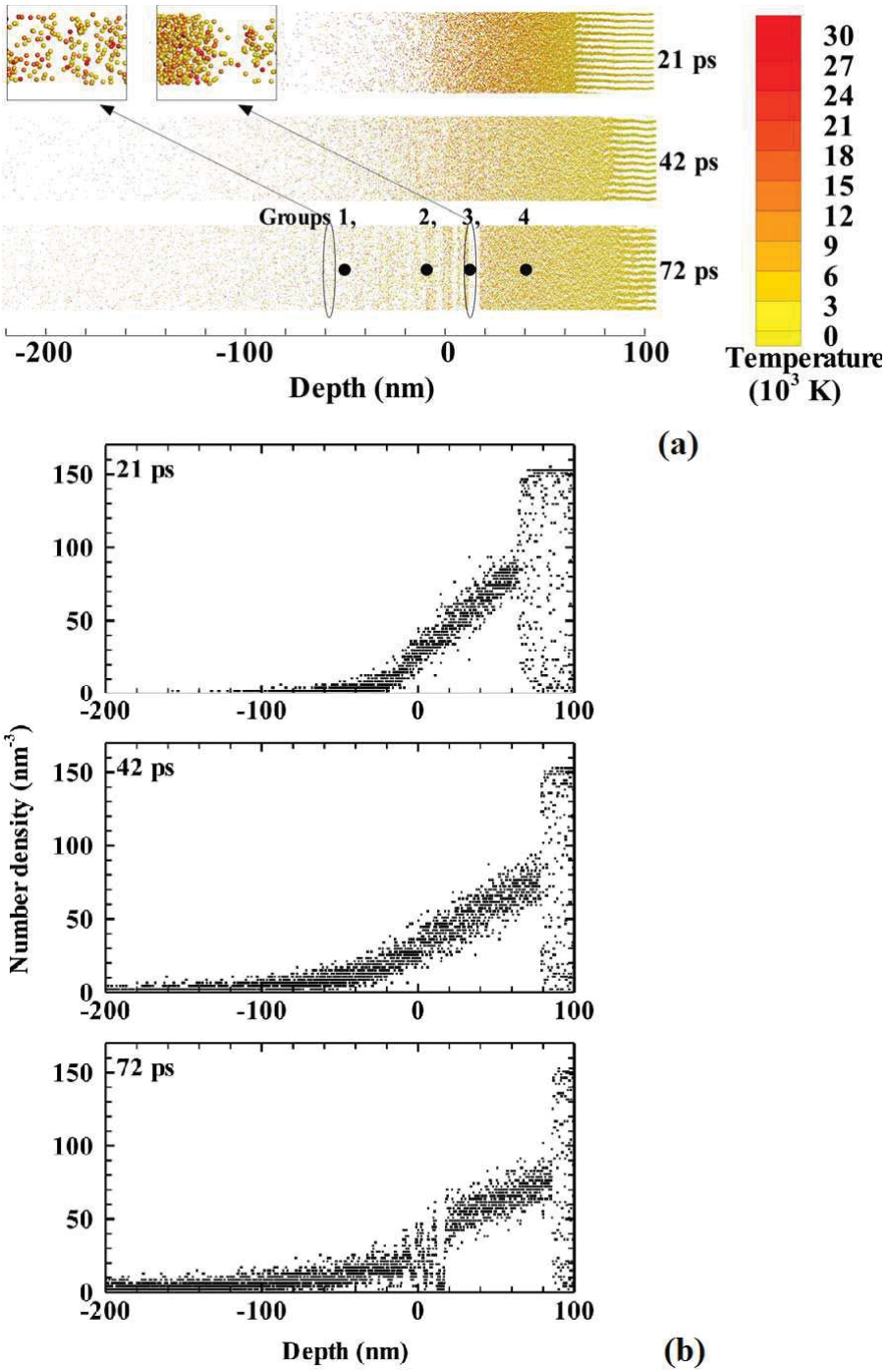

Figure 1.12. Left column: material structures evolution, right column: material density distribution. Laser pulse duration: 100 fs; wavelength: 248 nm; absorbed laser fluence: 1.0 J /cm^2. Material: Ni. (Hu et al., 2010).

1.3.1.4 Fragmentation

At higher fluence, fragmentation replaces CPPS as the dominant ablation mechanism. Due to the rapid heating in a constant density, there is a large thermo-elastic stress generated inside the target, leading to a nonuniform strain rates. Internal surfaces are created under this strain rates, and a lot of small fragments are formed and removed from the target bulk, consequently. This ablation process induced by highly nonuniform strain rates is called fragmentation. The occurrence of fragmentation is first proved by Perez and Lewis (2002). It is further analyzed by MD simulation in Perez and Lewis (2003), as presented in Figure 1.13. The pulse duration τ is 100 fs, and the laser fluence is much higher than the ablation threshold (F_{th}). The region dominated by fragmentation is denoted as III at t=600 τ. The removed material in this region is in a state of supercritical fluid, and is composed of a large number of fragmented pieces.

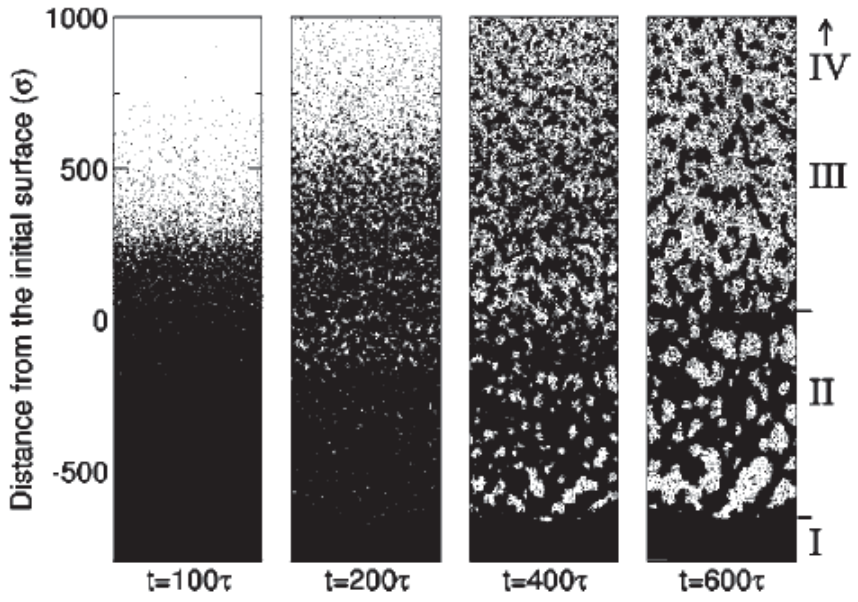

Figure 1.13. Snapshots of material evolution with F=2.8F_{th}, pulse duration τ is 100 fs. Region IV is the gaseous region (out of the range of the last snapshot). (Perez and Lewis, 2003).

1.3.1.5 Vaporization

Vaporization, also known as atomization, will occur at even higher laser fluence. It refers to the complete dissociation of the atoms in a top layer, which should be distinguished from the normal phase transition to gas state, like evaporation and sublimation. In the high fluence range, the atoms in surface layer will gain sufficient energy to escape from the target directly, and the whole skin layer will be atomized and vaporized. Strong ionization will also be induced by the sufficiently high laser fluence and the collision process. Therefore, the ablated material mainly contains single particles like electron, ions, and neutral atoms. Very rare clusters and droplets exist in this ablation regime.

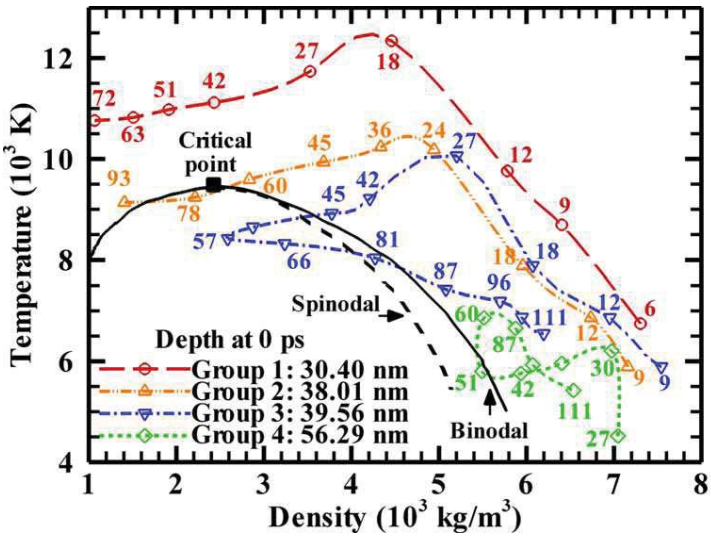

Figure 1.14. Thermodynamic trajectories of four atom groups. Laser and material parameters are the same as in Figure 1.11 (Hu et al., 2010).

It should be pointed out that although the ablation mechanisms discussed above occur and dominate at different fluence ranges, in many cases, two or even more of them will take place simultaneously. In Figure 1.13, at delay time of 600 τ, regions denoted by II, III and IV are dominated by phase explosion, fragmentation and vaporization, respectively (Perez and Lewis, 2003). In the ablation shown in Figure 1.12, more than

one mechanism is involved too, as illustrated by the thermodynamic trajectories in Figure 1.14 (Hu et al., 2010). It can be seen that the atoms in group 1 undergo fragmentation without cooling down into the metastable zone. On the other hand, the atoms in group 2 and group 3 are first heated to above CP, and then enter the metastable zone during the expansion process, which is the characteristic of CPPS.

1.3.2 Non-Thermal Ablation

Unlike thermal ablation, non-thermal ablation is mainly driven by the electric force. The most important non-thermal ablation is the Coulomb explosion (CE) (Stoian et al., 2000; Stoian et al., 2002; Reif et al. 2004), the main feature of which is as follows. During the ablation process, intensive ejection of hot electrons can lead to accumulation of positive charge in a superficial target layer and generate a strong electric field. In this electric filed, ions can be pulled out of the target surface and accelerated. Thus, CE can occur, when the ions are ejected out of the target by the repulsive Coulomb force. It is an ultrafast ejection process and typically takes place on a time scale of several hundred femtoseconds (Bulgakova et al., 2005b). One of the characteristical features of CE is that the ejected ions show momentum scaling (Roeterdink et al., 2003), where the momentum of ion species with the same mass but different charge is proportional to the ion charge number. Therefore, ions with different charge will be separated during ejection process, and several subgroups will be consequently formed.

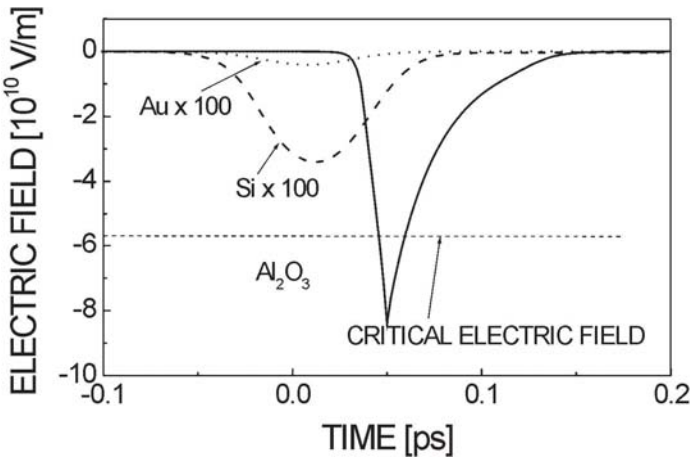

Figure 1.15. Temporal profiles of the laser-induced electric field in the surface region of the targets. Laser fluences are chosen to be above the ion emission threshold for each material (4 J/cm^2, 0.8 J/cm^2, and 1.2 J/cm^2 for Al_2O_3, Si, and Au, respectively). The laser pulse of 100 fs duration is centered at t = 0 (Bulgakova et al, 2004).

It has been shown that CE is the major process for the fast ion ejection from the insulator target irradiated by a femtosecond laser (Stoian et al., 2000, Stoian et al., 2002, Reif et al. 2004, Bulgakova et al, 2004, Bulgakova et al., 2005b). However, its occurrence in semiconductors is still under a debate (Roeterdink et al., 2003, Stoian et al., 2004, Roeterdink et al., 2004, Dachraoui et al., 2006b, Dachraoui et al., 2006c, Lenner et al., 2007, Hebeisen et al., 2008, Balling and Schou, 2013). The non-thermal peaks in the time-of-flight spectra and the momentum scaling of the velocities of ejected ions were observed by Roeterdink et al. (2003) and Dachraoui et al. (2006c), which were implicated as the conclusive evidence of the existence of CE. Dachraoui et al. (2006a, 2006c) also proposed the occurrence of CE in the ablation of metals. On the other hand, some other studies (Stoian et al., 2002, Bulgakova et al, 2004, Bulgakova et al., 2005b, Stoian et al., 2004, Balling and Schou, 2013) questioned such conclusions. First, some other possible originations of the observed phenomena were proposed, such as double layer effect and desorption (Stoian et al., 2004, Balling and Schou, 2013). Besides, the hydrodynamic simulation results by Bulgakova et al (2004, 2005a, 2005b) revealed that the electric field strength in the semiconductors is below the critical electric field of CE, as shown in Figure 1.15. The temporal evolution of the electric field in the surface region of Al_2O_3,

Si, and Au during ablation process was calculated. It is revealed that the electric field in Al_2O_3 is above the critical strength for CE, while the electric fields in Si and Au are much lower than the critical value. This is because semiconductors and metals have high electron diffusion and mobility, and the positive charge near the surface are quickly compensated by the electrons from the bulk material. Therefore, it requires a further investigation to provide a clear evidence on the occurrence of CE in semiconductors. Most existing studies have focused on the relatively low laser fluence range (<10 J/cm^2), where the positive net charges are believed to be able to survive for a long time before becoming compensated by the electrons inside the bulk material. However, the underlying physics in the higher fluence regime need to be studied, where the electron emission rate will be much higher and the generated electric field is expected to be stronger, which is one of the critical criteria for the existence of CE.

1.4 Plasma Dynamics

In USLP-matter interaction, two kinds of plasma are observed: early stage plasma and plume plasma. Different from longer pulse ablation, the plume plasma (generated after hundreds of ps, Zeng et al., 2005) does not has any interaction with the incident pulse due to the ultrashort pulse duration. On the contrary, the early stage plasma starts early enough (in a few femtoseconds, Geindre et al., 1994) to couple with the laser pulse. In USLP-matter interaction, early plasma generation and evolution can significantly affect the laser beam energy deposition into the target and the consequent material removal process. By controlling the plasma interaction with laser pulses and target surface, potential improvement of ablation efficiency and quality is expected. Therefore, it is necessary to understand the fundamental physics of plasma generation and evolution.

1.4.1 Early Stage Plasma Dynamics

In the early stage of USLP-matter interaction, the laser beam energy is first absorbed by the electrons close to the surface. After gaining enough kinetic energy, these energetic electrons can be ejected from the surface through both photoelectric and thermal emission

processes (Herring et al., 1949; Bechtel et al., 1977; Chen and Mao., 2008). When the hot electrons are emitted into the ambient gas, they would collide with neutral gas atoms or molecules and, thus, ionize the gas. During the laser pulse, the emitted electrons from the target surface and additional electrons formed via electron impact ionization of the ambient gas can absorb laser energy directly through IB absorption. The absorbed photon energy from the femtosecond laser pulse can increase the electron temperature and enhance the ionization process. As a consequence, a microscale plasma above the target surface is initiated during the laser pulse. A certain laser intensity is required for the generation of early plasma, which is considered as the threshold for early plasma formation. It is shown in Figure 1.16 that the threshold for early plasma formation decreases with increasing pulse width for a laser pulse width under 200fs (Chen and Mao, 2008).

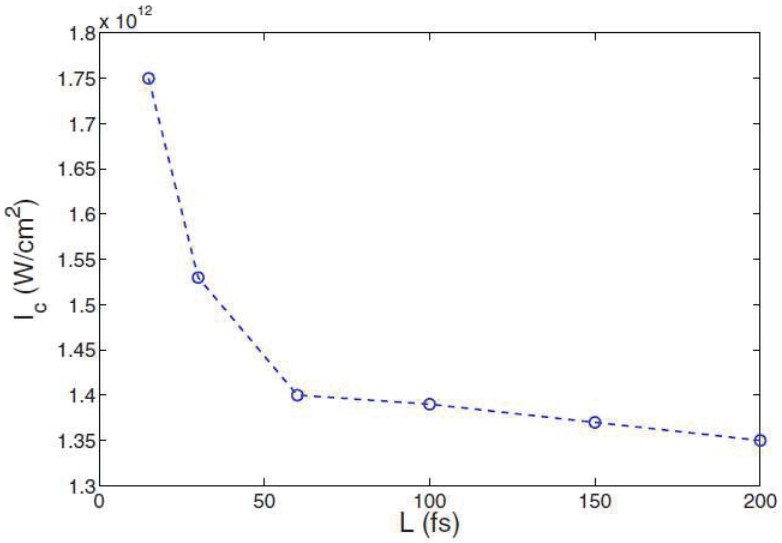

Figure 1.16. Calculated laser intensity threshold for laser-induced plasma formation as a function of laser pulse's FWHM (Chen and Mao, 2008).

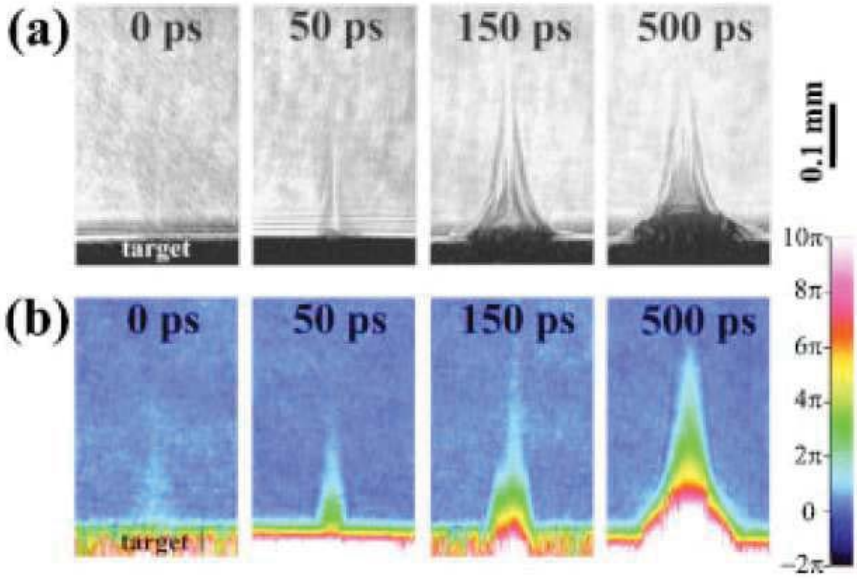

Figure 1.17. Shadowgrams (a) and phase shift maps (b) of the plasma at four different delay times (Mao et al., 2000b).

Because of the thermal movement and density gradient of the electrons and ions in the space, the early plasma will expand quickly after its formation in the perpendicular direction to the target surface. As shown in Figure 1.17, the early plasma primarily expands in longitudinal direction and forms a line like profile (Mao et al., 2000b). The initial expansion velocity in the perpendicular direction is as high as 10^7 m/s. The expansion process of high density plasma is affected by the collision and Coulomb effects among the elections and ions. At a low density comparable to gas, the expansion process can be treated as a collision free expansion and there is no collision between particles (Ellegaard et al., 2002; Loir, 2003). The early plasma will cool down quickly during the expansion process. The energetic electrons tend to expand fast but are attracted and oscillate back and forth between the ions. In this way the energy of electrons is transferred to ions, and the temperature and expansion speed will decrease. The coupling of the two subsystems is efficient and fast. Within a few tens of periods of the ion plasma frequency, the electrons transfer almost all their energy to the ions.

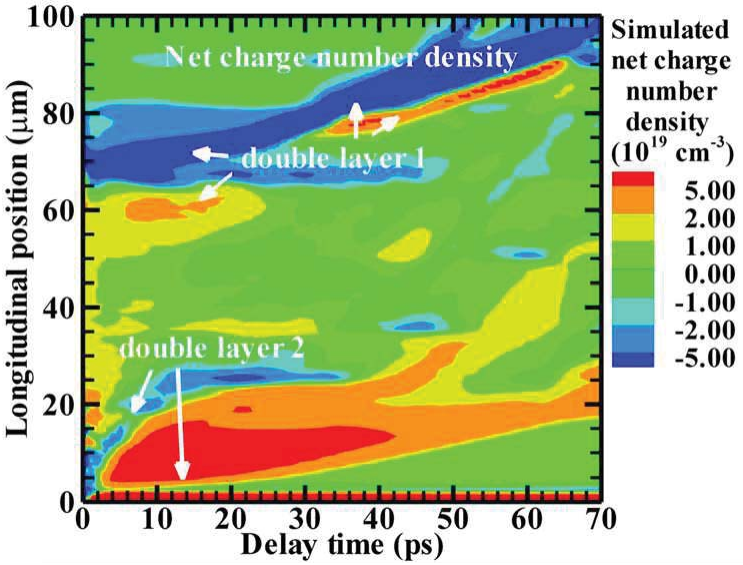

Figure 1.18. Simulated spatial-temporal evolution of charged particle (net charge) number density within the delay time of 70 ps. Laser wavelength: 800 nm; pulse duration: 100 fs; power density: 4.2×10^{14} W/cm^2; and target: Cu (Hu et al., 2011a).

Electrostatic mechanism is one of the key mechanisms for early plasma expansion. In the early plasma, the ejected energetic electrons expand faster than the ions. An electrical double layer is formed as a consequence of the high electron speed that carries electrons far out into the ambient in front of the ion cloud, known as double layer effect (Plyutto, 1961; Bulgakova et al, 2000; Nedelea and Urbassek, 2004; Nedialkov et al., 2004b). Hu et al. (2011a) studied the charged particle evolution with respect to time during the femtosecond ablation of copper by MD-MC simulation. Figure 1.18 shows the simulation results of evolution of net charge number density, with respect to delay time and space. The formation of double layers is clearly observed to begin in the very early stage (starting before 1 ps) in the regions of 0-30 μm and 60-80 nm. The negative charges are separated from the positive charges, and expand faster in front. Consequently, there will be an electrostatic field pointing out of the surface located mainly at the ion front. Ions with different charge will be accelerated in proportion to their charge. This effect causes a spatial segregation of the different charge states and a stronger acceleration of highly charged ions and light species, since the space-charge field is concentrated on the ion expansion front and hence on the light species (Zhigilei, 2003, Noël and Hermann, 2007).

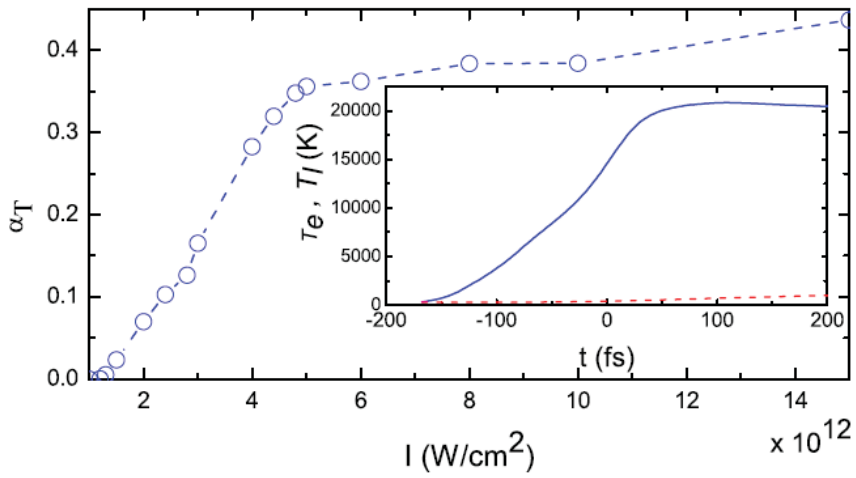

Figure 1.19. Calculated total laser absorption by the early plasma as a function of laser intensity with FWHM of 100 fs. Inset plot shows the electron surface temperature (solid line) and lattice surface temperature (dashed line) as a function of time, where the laser peak intensity is 10^{13} W/cm^2 and FWHM is 100 fs (Chen and Mao, 2008).

Since the early plasma is formed before the end of laser pulse, it will interact with the incident laser pulse via absorbing and scattering processes. The major absorption processes include inverse Bremsstrahlung absorption (IB) and multiphoton absorption (MP). IB depends on electron density, laser wavelength, laser intensity, and ion density, while MP relies on atom density, laser wavelength, and laser intensity. It is revealed by Chen and Mao (2008) that the total absorption of incident laser energy by early plasma increases fast with the incident laser intensity up to about 5×10^{12} W/cm^2, after which the increase is much slower and tends to saturate (Figure 1.19). According to their results, the absorption by early plasma is negligible at the intensity below 1.39×10^{12} W/cm^2. The early plasma absorption can block the incident laser beam, and the beam energy deposited into the target material is reduced. Zhang et al. (2011) have reported that there is a saturation phenomenon for femtosecond laser ablation of silicon-on-insulator at high laser intensity, which is due to the absorption by early plasma. The absorbed photon energy from the laser pulse can further enhance the ionization of the ambient gas, as well as increase the electron temperature of the plasma. Being heated to an extremely high temperature, the thermal energy of the early plasma can be diffused both into the ambient

gas and back to the target surface. The studies of Vorobyev and Guo (2005) and Bulgakova et al. (2008) revealed that the plasma could transfer thermal energy back to the target surface, leading to a significant enhancement in thermal energy retained in the materials. Therefore, by fully understanding the underlying physics of plasma evolution, it is possible to control the plasma behavior to improve the ablation process.

1.4.2 Plume Plasma

Under the irradiation of USLP, the target will be ablated. During the ablation process, the irradiated material will be partially ionized by avalanche ionization, and consists of electrons, ions and neutral atoms, consequently forming a plume plasma. The generation of plume plasma usually starts from hundreds of picoseconds after the irradiation of laser pulse, which is required for sufficient lattice heating. Compared with the early stage plasma, the plume plasma expands much slower, the speed of which is about 10^3 m/s as reported by Zeng et al. (2005). Besides, the expansion speeds in the longitudinal direction and radial direction are close, and hence, the plume plasma expands in a spherical shape, as illustrated in Figure 1.20.

The components of the plume plasma are studied by time-gated fast imaging and optical emission spectroscopy measurements. Amoruso et al. (2007a) and Noël and Hermann (2007) revealed that for ablation of metals at low laser fluences (< 0.5 J/cm^2), the plume plasma consists of two plume components. A “slow” component of high intensity is found near the target whereas a “fast” component with lower emission intensity is located at larger distance. The slow component consists mainly of nanoparticles, while the fast component is composed of electrons, ions, and neutral atoms. The fast component separates from the target surface, whereas the slow component remains in contact with the target surface, even for times larger than tens of μs. At higher fluences a new third component preceding the main atomic plume component was observed by Noël and Hermann (2007). It is considered to be the recombination of faster ions with electrons in the early stage of the plume evolution. However, Axente et al. (2009) reported that for ablation of fused silica, only one “fast” component exists in the plume plasma, which expands three times faster than the fast

component in ablation of copper. No nanoparticles are observed in this component and it should be composed of electrons, ions and neutral atoms.

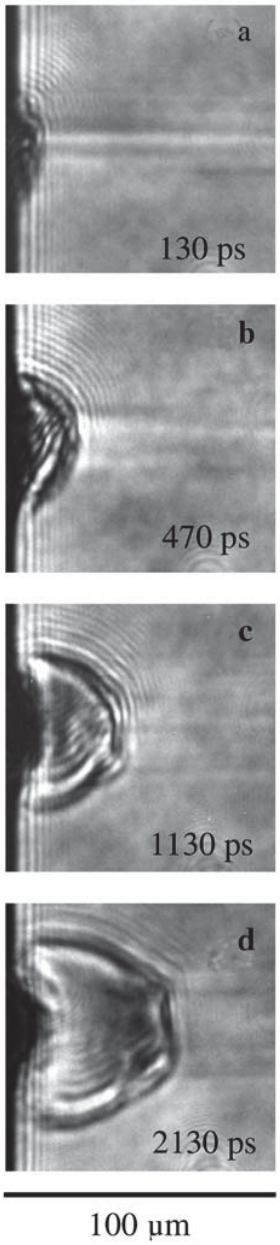

Figure 1.20. Temporal evolution of shock wave images obtained by laser shadowgraphy. fs laser parameters: pulse duration 100 fs, wavelength 800 nm, peak power density 112 TW/cm^2 (Zeng et al., 2005)

1.5 Double-Pulse Ablation

To understand the fundamental physics of USLP-matter interaction, a straightforward methodology would be to study the interaction between target materials and single laser pulse. However, single pulse (SP) ablation cannot provide the best results for many applications, such as laser-induced breakdown spectroscopy (LIBS), material removal, surface treatment, etc. Multi-pulse (typically double-pulse) techniques have been developed to enhance these applications. The double-pulse (DP) method is a technique to process materials or laser-induced plasma by two temporally separated pulses with a defined delay time, varying from fs to μs. There are three typical configurations for the DP method: collinear, pre-ablative orthogonal, and reheat orthogonal, as shown in Figure 1.21 (a), (b), and (c), respectively. For the collinear method, two pulses are sent to the target through the same beam path normal to the target surface. In pre-ablative orthogonal setup, the first pulse travels parallelly to the target surface, creating a spark on the surrounding media, and the second one ablates the sample by normal irradiation. The reheat orthogonal uses the similar idea to the pre-ablative, but with a switched order of the two pulses. Among these configurations, the collinear method is most commonly used, since both pulses are used to interact with target materials. The adoption of temporally separated pulses could induce different laser-material interaction mechanisms, and hence provides new possibilities of further enhancement of material processing, such as the change of morphological features of ablation craters and laser-induced plasma.

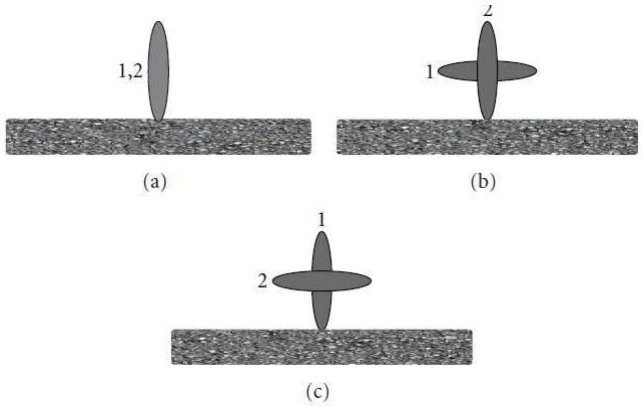

Figure 1.21. DP ablation configurations (a) shows collinear configuration; the first pulse ablates the sample and the second one reheats the plasma, (b) is an orthogonal pre-ablative configuration; the first pulse creates a spark on the surrounding media and the second one ablates the sample, (c) shows the same idea as (a), but the plasma is reheated in an orthogonal way (Anabitarte et al., 2012).

1.5.1 Material Removal

DP ablation has been discovered to be able to enhance the ion ejection during the ablation process. Using emission spectroscopy, Hu et al. (2007) and Singha et al. (2008) observed that a second delayed pulse causes an increase in the ion emission from Si, as shown in Figure 1.22. The fluorescence from Si ion increases with the increase of the pulse delay. The similar phenomena were also observed for metals (Semerok and Dutouquet, 2004; Scuderi et al., 2005; Cogan et al., 2005; Le Harzic et al., 2005a; Chowdhury et al., 2005; Hu et al., 2007; Donnelly et al., 2009; Povarnitsyn et al., 2009; De Falco et al., 2008; Perez et al., 2008). Figure 1.23 shows the ion time-of-flight (TOF) signals and the total yield as a function of time delay for a titanium target (Donnelly et al., 2009). It is shown that the ion emission rate remains constant before 10 ps, and starts to rise from 10 ps to 100 ps, and tends to drop quickly after that. The total emission rate is over 10 times higher than the SP ablation. Two mechanisms have been proposed by previous studies to explain the steep rise of the ion emission. For semiconductors like silicon, Koudoumas et al. (2004) proposed that the first pulse melts the surface and the second pulse interacts more strongly with the liquid. For metals, a second possible mechanism is that the enhanced fluorescence is produced by multiphoton excitation of

atoms and particles in the plume produced by the first half pulse, as proposed by Semerok et al. (2004) for Cu ablation.

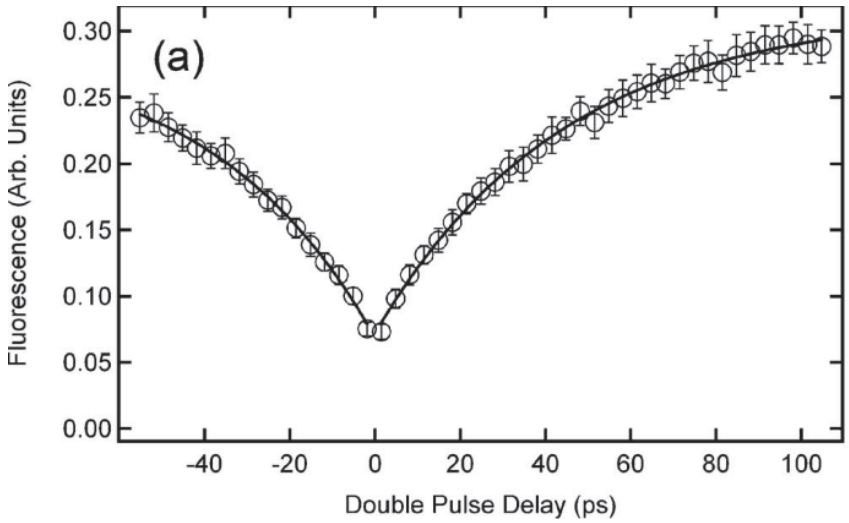

Figure 1.22. Atomic fluorescence produced by the double pulse ablation of Si<111>. Fluorescence vs delay time at a combined fluence of 48.7 J /cm2 (45 fs, 800 nm). Each point is the average of 40 pulses, with each pulse ablating a fresh surface area. The error bars are a single standard deviation. The smooth curve is a least squares fit of an exponential function (Hu et al., 2007).

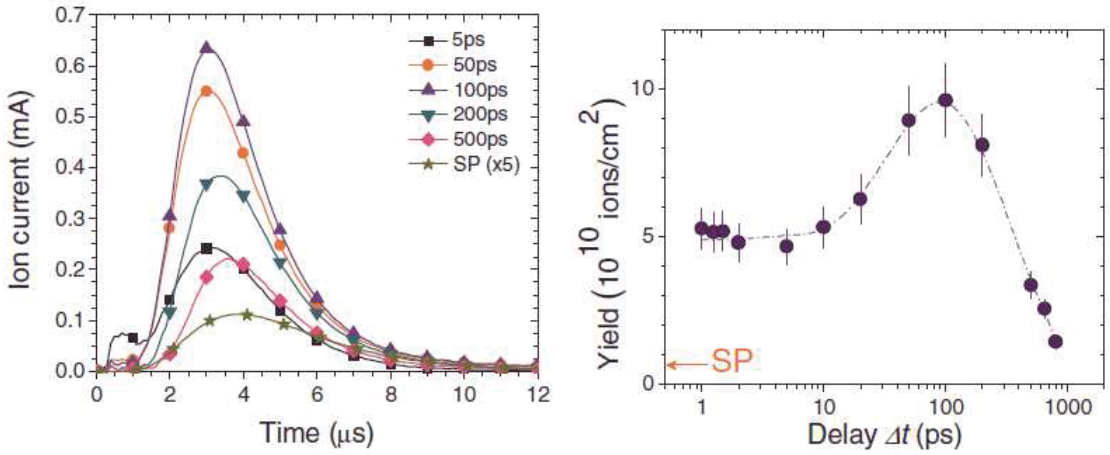

(a) (b)

Figure 1.23. (a) Ion TOF signals for different delays between the two laser pulses. SP indicates the signal for SP irradiation, and (b) Ion yield as a function of the delay between pulses. The dashed curve is a guide to the eye. The arrow indicates the yield for the first pulse only (SP). Laser: 250 fs, 1054 nm, 85 μJ per pulse. Target: Ni (Donnelly et al., 2009).

Despite the strong enhancement of the ion ejection, the ablation rate (ablation depth per pulse) was observed to be suppressed by DP ablation for metals (Semerok and Dutouquet, 2004; Scuderi et al., 2005; Cogan et al., 2005; Le Harzic et al., 2005b; Chowdhury et al., 2005; Hu et al., 2007; Donnelly et al., 2009; Povarnitsyn et al., 2009; Singha et al., 2008; Wojakowski et al., 2009; Spyridaki et al., 2003; Koudoumas et al., 2004; Amoruso et al., 2007b). Figure 1.24 shows the ablation rate variation of copper as a function of delay time, which have been observed both in air and in vacuum at fluence levels in the range from a few to ten times the ablation threshold (Povarnitsyn et al., 2009). When the time delay is much shorter than the electron-lattice relaxation time (10 ps for metals), the ablation efficiency is almost independent of the delay. When the time delay is close to electron-lattice relaxation time, the ablation efficiency decreases monotonically, and finally, reaches a plateau regime for 100 ps of delay, where it can reach values even smaller than that obtained by a single pulse. Several explanations of the unusual dependency of the crater depth on the delay were proposed. In particular, Povarnitsyn et al. (2009) analyzed this suppression of the ablation efficiency by detailed

hydrodynamic modeling for the case of DP ablation of a copper target irradiated by 100 fs pulses at 800 nm, and related it to the formation of a second shock wave induced by the interaction of the second laser pulse with the expanding target material that suppresses the rarefaction wave created by the first pulse, thus lowering the ablation yield. The second possible mechanism is the drop of electronic heat conductivity at high temperature (Singha et al., 2008; Penczak et al., 2014; Amoruso et al., 2010; Noël and Hermann, 2009). Kanavin et al. (1998) and Kim et al. (2008) showed that the electron heat conductivity decreases with the increase of the lattice temperature. During DP ablation, the electronic heat conductivity is decreased by the heating of the first pulse, and the heating depth by the second pulse is subsequently reduced, leading to the decrease of the ablation depth. A plasma shielding effect was proposed by Semerok and Dutouquet (2004) as another possible reason for ablation suppression. With sufficient laser fluence, the first pulse will create strong plasma above the target surface. When the pulse delay is set to be long enough so that the second pulse arrives on the target surface after the plasma generation, the plasma will interact with the second pulse and significantly absorb the incident laser energy, leading to the reduction of the ablation rate.

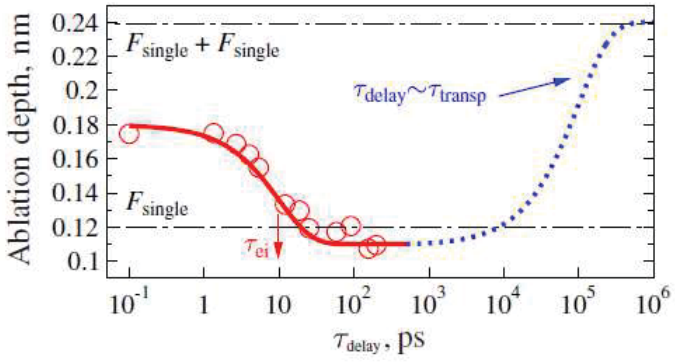

Figure 1.24. Empty (red) circles, DP experiment with Cu ablation by pulses with F_{single}=2 J/cm^2 (800 nm, 100 fs); solid (red) curve, interpolation of the experiment. Dashed (blue) curve, theoretical assumption for $\tau_{delay} \sim \infty$ (Povarnitsyn et al., 2009).

Amoruso et al. (2010) showed the detailed analysis of the ejected materials during DP ablation. Figure 1.25 shows the yield of ions, nanoparticles (NP), and neutral atoms during DP ablation of Cu (Amoruso et al., 2010). The ion yield first increases with the pulse delay, reaching the peak value at several hundreds of ps, and then starts to drop. The ion yield by DP ablation is much higher than SP ablation. The atom yield is also much higher than SP ablation, and increases steeply with the pulse delay. The NP first decreases with the pulse delay, and becomes smaller than SP ablation after tens of ps. It remains constant at the pulse delay longer than 100 ps. The NP yield decreases with the pulse delay in a very similar manner to the ablation rate shown in Figure 1.24, indicating that ablated material of an USLP process mainly decomposes into a NP form. It has been observed that there are two distinct ablation plumes in the far field: a faster-moving atomic plume and a slower-moving nanoparticle plume, as observed by Amoruso et al. (2007a). Typically, the atomic/ion plume accounts for only 10%–20% of the total ablated mass, and the NP takes more than 80% (Amoruso et al., 2007a; Amoruso et al., 2008; Povarnitsyn et al., 2009). Therefore, by adopting DP ablation of metals, the NP yield can be suppressed as well as the ablation rate, while the yield of ions and neutral atoms can be significantly enhanced, leading to the enhancement of the laser-induced plasma, which will be discussed in the next section.

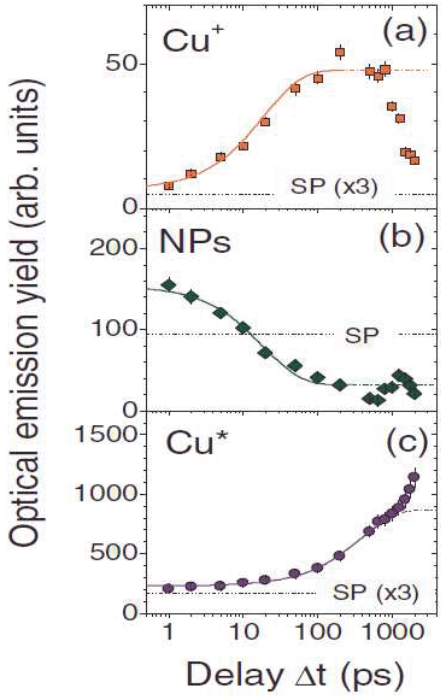

Figure 1.25. Optical emission yield of the various plume components as a function of the time delay between the pulses: (a) Cu^+; (b) nanoparticles (NP); and (c) Cu atom. The dashed lines show the values corresponding to SP irradiation. The solid lines are fits to an exponential dependence of the emission intensity on time delay (Amoruso et al., 2010).

Different from metals, ablation enhancement by DP ablation of silicon was reported by Singha et al. (2008), Wojakowski et al. (2009), Hu et al. (2007), and Choi et al. (2002). Wojakowski et al. (2009) studied the ablation depth per pulse for DP ablation of silicon by a picosecond laser (1064 nm, 8.5 ps). Figure 1.26 shows the normalized ablation depth per pulse of DP ablation, which was calculated as quotient of the measured depth of the DP ablation and the corresponding SP ablation with the same total pulse energy. It can be seen that the DP ablation could significantly increase the ablation rate. The enhancement is around 10%-20% at the fluence of 2.6 J/cm^2, and is drastically increased to over two times when the laser fluence is increased to 7.8 J/cm^2. The enhancement effect does not seem to be sensitive to the pulse delay in the study range (6000-15000 ps). Choi et al. (2002) studied the DP ablation of silicon by a femtosecond laser (83 fs, 800 nm), and also showed the enhancement of ablation rate by DP ablation. In this case, the maximum enhancement occurs at the pulse delay of around 11 ps. It was

proposed in Hu et al. (2007) that the responsible reason is the silicon melting and the resultant stronger coupling between the second pulse and the silicon target.

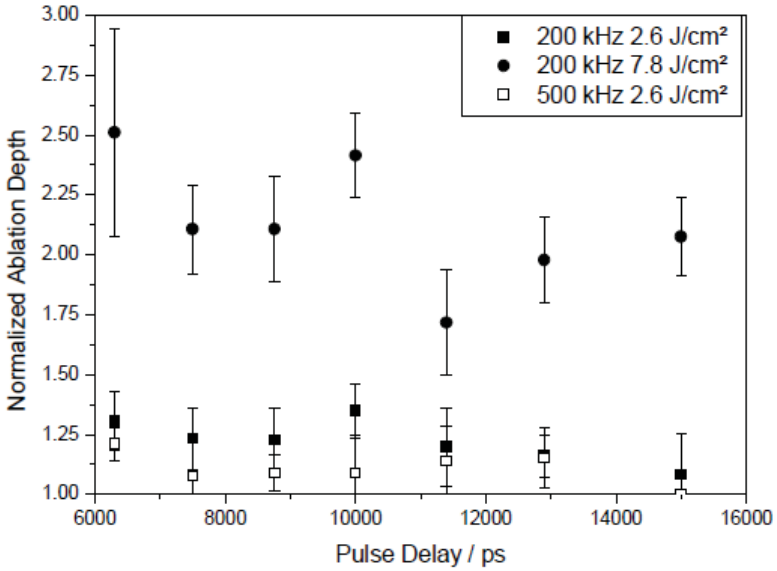

Figure 1.26. Normalized ablation depth per pulse for DP ablation (1064 nm, 8.5 ps). The normalized values are calculated as quotient of the measured depth of the DP ablation and the corresponding SP ablation with the same total pulse energy. (Wojakowski et al., 2009).

1.5.2 Plasma Enhancement

Laser-induced breakdown spectroscopy (LIBS) is a promising detecting technique which provides an easy, fast, and in situ chemical analysis with a reasonable precision, detection limits, and cost (Scaffidi et al., 2003; Eland et al., 2001; Scaffidi et al., 2006; Margetic et al., 2000). It is a promising option for remote diagnostics and non-destructive testing technique, which keeps the measured object undamaged. The major challenge for LIBS technique is that its sensitivity is limited due to the continuum radiation from electrons. To overcome that, it is demanded to significantly increase the intensity of the plasma emission, which could be possibly achieved by DP ablation. The plasma enhancement by DP ablation could be attributed to two possible mechanisms. First, the first pulse will create a plasma during the ablation process. Upon the arrival of the second

pulse, the plasma can possibly absorb a large portion of its energy, and be reheated to a higher temperature and density. Second, in some cases, DP ablation could enhance the ablation rate and remove more material from the target. The removed material will contribute to the enhancement of the plasma.

Harilal et al. (2013) studied the plasma emission of collinear DP ablation with a pulse duration of 100 fs and a wavelength of 800 nm, and revealed that the emission signal first increases with the time delay and reaches the peak value at about 20 ps, as shown in Figure 1.27. After 20 ps, the emission drops as the time delay further increases. Similarly, the electron temperature of the plasma also reaches the maximum value at the time delay of 20 ps, as shown in Figure 1.28. The authors claimed that the reheating by the delayed pulse of the ablation plume generated by the first pulse is the main mechanism for the improved signal intensity in DP LIBS.

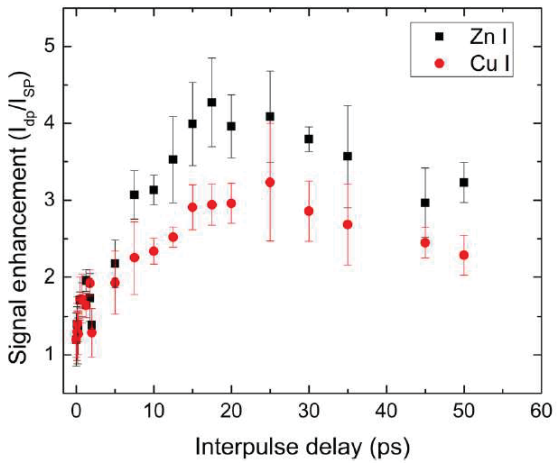

Figure 1.27. The signal enhancement recorded for Zn I 481.05nm and Cu I 510.55 nm lines for DP fs LIBS with respect to single pulse LIBS. For direct comparison a single pulse energy of 1 mJ was used which was equivalent to the sum of the energy for pre and delayed pulses in DP scheme (collinear, 100 fs, 800 nm) (Harilal et al., 2013).

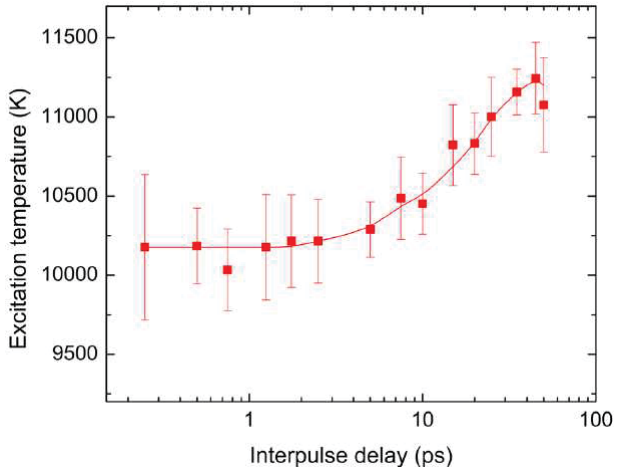

Figure 1.28. The excitation temperature of the fs DP plasma plume estimated using the Boltzmann method for various inter-pulse delay. The estimated excitation temperature for single fs pulse LIBS (or ULIBS) was 9800±300 K (Harilal et al., 2013).

Mildner et al. (2013) studied the LIBS enhancement by the collinear double pulse with a pulse duration of 30 fs and a wavelength of 785 nm. As shown in Figure 1.29, the emission signal evolution was divided into four stages. In stage I (0-1 ps), there is no enhancement of the signal and it is still in the electron thermalization time (around 1 ps for Al (Mueller and Rethfeld, 2013)). It is concluded that during electron thermalization, the second pulse has no major influence on the ablation mechanisms and the overall behavior resembles the case of single pulse ablation at the same total pulse energy (regime I). The second, delayed energy deposition into the system may only lead to a corresponding delayed electron–phonon coupling. In stage II (1-10 ps), the signal starts to increase with the pulse delay. In this stage, the electron starts to transfer energy into the lattice and the lattice begins to melt. The electron conductivity in liquid state is much smaller than in solid. The deposited laser energy is therefore confined in a much shallower zone. Therefore the liquid can reach much higher temperatures and higher ionization degree of the plasma plume. It should be noticed that the electron and lattice have not reached the thermal equilibrium state at this stage, and the lattice temperature increases with the pulse delay. In stage III (10-100 ps), the enhancement continues to grow but saturates at several tens of ps. It is because at some point, the lattice and

electrons have achieved the equilibrium, and the lattice temperature has reached the peak value. After that, the heat accumulation effect will not be further enhanced. In stage IV (100-1000 ps), the enhancement signal starts to grow again. Mildner et al. (2013) believed that this could be due to the interaction of the second pulse with the plume plasma. In their study, the maximum enhancement was observed at 800 ps. The similar phenomenon was also reported by Piñon et al. (2008), Piñon et al. (2009) and Balachninaitė et al. (2010).

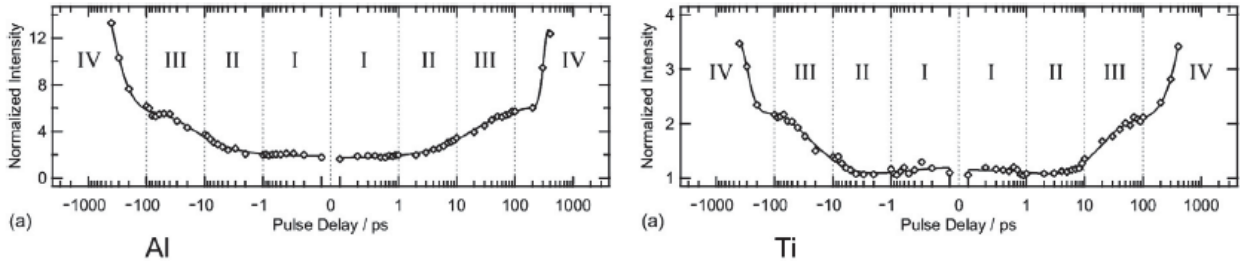

Figure 1.29. Transient DP-LIBS signal of aluminum and Ti on a logarithmic time scale with a total pulse energy of 350 nJ and equal intensity ratio between the twopulses. A maximumLIBS-signal enhancement is reached around (800 ± 30) ps; optimal reflection of the 2nd pulse is seen at approximately (150 ± 30) ps. Roman numerals label four differentenhancement regimes: (I) no enhancement; (II) increase; (III) saturation behavior; (IV) further increase with maximum LIBS enhancement (collinear, 30 fs, 785 nm) (Mildner et al., 2013).

Liu et al. (2013) studied the enhancement of the LIBS from the air atoms and ions by DP ablation, as shown in Figure 1.30. The orthogonal configuration was adopted, with a pulse duration of 33 fs and a wavelength of 810 nm. The first pulse causes the air breakdown and generates a filament, and the second pulse reheats the filament in air. It is revealed that the enhancement ratio can be fitted by a Gaussian function with respect to the time delay between the two pulses. The maximum enhancement was observed at the zero pulse delay, and can be as high as 35. Accordingly, the electron temperature calculated by the Boltzmann fitting method also displays a Gaussian style evolution, and reaches the peak value at the zero time delay, as shown in Figure 1.31.

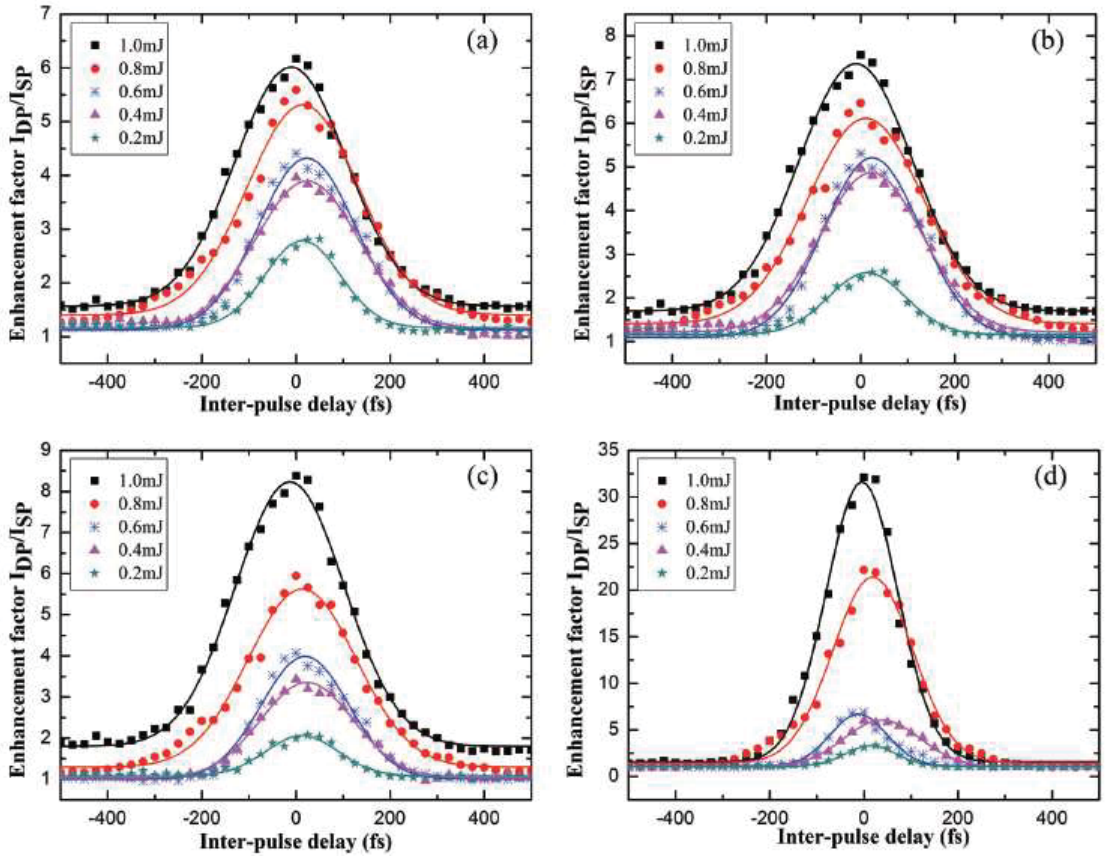

Figure 1.30. Influence of the inter-pulse delay, on the signal enhancement factor for several emission lines in the DP-LIBS measurements with all cases of probe pulse energy. (a), (b), (c) and (d) indicate the results of the spectra of 777.2, 746.8, 656.2 and 500.5 nm, respectively (orthogonal, 33 fs, 810 nm). (Liu et al., 2013).

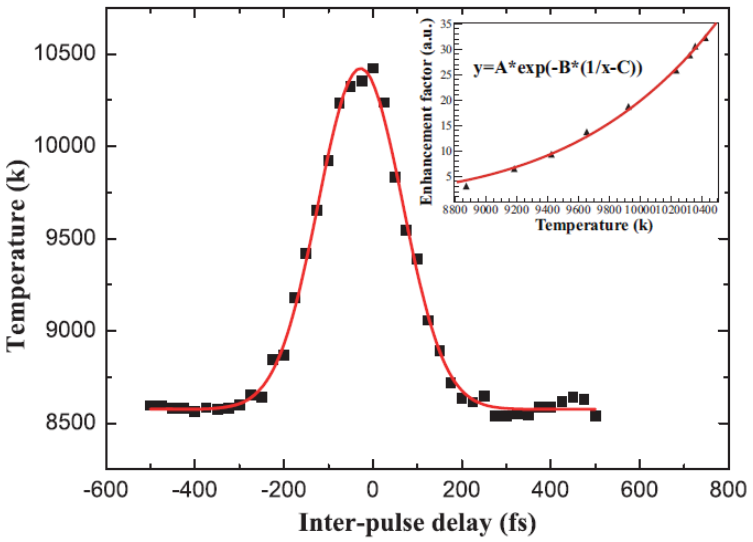

Figure 1.31. The time-averaged electron temperature as a function of the inter-pulse delay between the two laser pulses in the DP-LIBS measurements with the probe pulse energy E_2 = 1.0 mJ. The insert shows the relation between the signal enhancement factor of N II 500.5 nm line and the electron temperature within the inter-pulse delay range of -200 fs to 0 fs (orthogonal, 33 fs, 810 nm). (Liu et al., 2013).

1.6 Modeling Approaches

As discussed in the previous sections, the USLP-matter interaction is a very complicated process and involves multi-physical phenomena. Therefore, a lot of theoretical studies have been devoted to investigating the physics of USLP-material interaction, focusing on different mechanisms under different conditions.

The two-temperature model (TTM) has been widely used to describe the energy transfer inside the target. It treats the electrons and lattice separately and captures the heat diffusion process well for the early stage of ultrashort laser ablation. Anisimov et al. (1974) proposed the parabolic TTM, which does not consider the non-thermalizatoin of electrons, and is only valid for pulses between 100 fs and 10 ps. Qiu and Tien (1993) and Tzou (1995) developed a hyperbolic TTM, that can be applied to pulse duration shorter than 100 fs. To further improve TTM, a semi-classical TTM was established by Chen et

al. (2006) to include the effects of non-equilibrium electron transport and electron drifting. TTM has its advantages in its simplicity, computational efficiency, and acceptable accuracy. It has been used to predict the ablation rate for femtosecond laser ablation (Wu and Shin, 2007a; Wu and Shin, 2009), and decent accuracy is achieved. However, its application is limited because it can not include the non-thermal process, material removal process, plasma generation and evolution, and laser-plasma interaction.

Hydrodynamic models (HD) (Spitzer and Haem, 1953, Eidmann et al., 2000, Laville et al., 2002; Colombier et al., 2005; Wu et al., 2007b; Wu et al., 2007c; Veysman et al., 2008; Chen and Mao., 2008) have been developed to describe the material removal and plume expansion behavior during laser ablation. It has been wide applied to longer pulse ablation processes and is proved to be valid for different laser and material properties (Wu and Shin, 2006, Wu and Shin, 2007b, Wu et al., 2007c). Nevertheless, most HD models only account for the plume behavior, and only a few of them consider hot electron emission and resultant early stage plasma generation, which are very important for femtosecond laser ablation. In the model developed by Bulgakova et al. (2007), the effect of hot electron emission process was accounted for and the electron transport inside the target was calculated. Chen and Mao (2008) applied a one-dimensional HD model to simulate the early stage plasma behavior during femtosecond laser ablation. Colombier et al. (2005) incorporated TTM into their hydrodynamic model to account for the electron-ion coupling effect and thus more accurate simulation results on laser ablation were obtained. The application of HD model is limited by its disadvantages in the following aspects. First, equations of state (EOS) have to be combined with the HD model to provide thermal and optical properties of materials in a wide range of temperature and density. Therefore, the accuracy of a HD model strongly relies on the accuracy of EOS, which is not satisfactory in many cases. Second, as a continuum model, a HD model is not capable of capturing the non-equilibrium transformation and other ultrafast dynamics during the initial stage of ablation.

Molecular dynamics (MD) simulation provides an explicit atomistic representation of target heating, material removal and expansion, and solves problems that cannot be accounted for by continuum models, such as highly non-equilibrium states and fast phase

transformations induced by USLP irradiation (Zhigilei and Ivanov, 2005). It has been widely used to investigate the USLP ablation of different materials in different fluence ranges (Zhigilei and Garrison, 2000; Vidal et al., 2001; Perez and Lewis, 2002; Perez and Lewis, 2003; Lorazo et al., 2003; Perez and Lewis, 2004; Cheng and Xu, 2005), providing insight into the material removal mechanisms and fast transitions in the very early stage. MD models have their own disadvantages in its computational cost. As a consequence, it can only simulate the ablation process in a very small simulation domain (typically hundreds of atoms) and time scale (tens of ps). This small domain can not fully capture the ablation process of the bulk material, which involves a collective motion of a large number of atoms. Besides, the MD model itself does not consider the electron relaxation dynamics. To improve the MD model, Schäfer et al. (2002) and Cheng and Xu (2005) established TTM-MD models by combining MD and TTM models together. The thermal evolution of the electron system and its coupling with the lattice are involved in these models. However, it does not consider the ionization of the material and fast phase and density change of the electron system.

In the studies by Lorazo et al. (2006) and Hu et al. (2010), an alternative improvement to MD models was proposed by coupling it with a Monte Carlo (MC) method, which was adopted to describe the electron dynamics during ablation. The ionization process and fast phase and density change of the electrons during ablation are described by the MC method, and the simulation results are improved, although the models do not account for the Coulomb interaction between charged particles and the early plasma generation and its interaction with the incident laser beam. Inogamov et al. (2008) used an integrated HD model and MD model, where the HD model was applied to solve the early stage heating and expansion of electrons and lattice, and the MD model was adopted to describe the lattice atoms motion and removal process later. This model however does not describe the surface electron emission process and the resultant early plasma generation. Hu et al. (2011a) improved the MC-MD model by adding the particle in cell (PIC) method to calculate the Coulomb interaction between charged particles and the beam propagation method (BPM) to handle the interaction of early plasma with the incident laser beam. As a result, the early plasma dynamics could be simulated with good

accuracy in comparison with experimental measurement. This MD/MC-PIC-BPM model was further combined with an HD model by Hu et al. (2012), where the output of the MD/MC-PIC-BPM model served as the initial stage of the HD model, and thus the plume plasma evolution in a longer time scale up to tens of ns could be covered. This model provides a reliable and complete description of the ablation process, including the early stage plasma evolution. However, the MD model used is a one dimensional model and does not consider the heat transfer, particle expansion in radial direction. Especially, the spacial distribution of the incident laser beam that will have a significant impact on the thermal diffusion and plasma evolution process could not be effectively accounted for. Besides, although it could be coupled with HD model in the later stage, the MD/MC-PIC-BPM model is still very computational expensive.

In conclusion, many different kinds of models have been developed in order to simulate the USLP ablation process. However, most of early studies only focused on one or several phenomena during the ablation process, and did not account for all the important physics mechanisms. Particularly, the early plasma dynamics were rarely studied, except for the models developed by Chen and Mao (2008) and Hu et al. (2011a, 2012). Therefore, it is necessary to develop a model covering all the important mechanisms during the ablation process and improve the understanding of the USLP-matter interaction. Particularly, electron dynamics inside the target, surface electron emission, early plasma generation and evolution, and its interaction with incident laser pulse and target surface are of special interest. Besides, the model should be able to cover the 3 dimensional evolution of the ablation process and be computationally efficient.

1.7 Research Objectives

The main objective of this research is to investigate the important physical mechanisms during USLP-matter interaction under different ablation conditions, and provide a better fundamental understanding. Particularly, the dynamics of early stage plasma during ablation processes will be investigated via modeling and experiment. Its generation, evolution, and interaction with the incident laser pulse and target surface will

be studied in order to improve the ablation process accordingly. The specific goals include:

1. Investigation of early plasma generation and evolution dynamics during USLP ablation of different materials (metal, semiconductor, and insulator): a comprehensive hydrodynamic model and MC-MD model will be developed, and experimental measurement will be carried out.
2. Investigation of ablation process of various materials in different laser intensity ranges: ablation rates at different ablation conditions will be studied to determine the optimum ablation condition; particularly, ablation in the high laser intensity range will be studied, considering the collisionless absorption and early plasma absorption.
3. Investigation of early plasma interaction with a subsequent laser pulse: both HD model and MD model will be developed to study the interaction between the early plasma and a subsequent laser pulse, and the experimental measurement will be carried out by a beam chirping method; the subsequent laser pulse will be used to excite the early plasma to higher temperature and density, in order to have a strong interaction with the target surface.

1.8 Thesis Outline

In this chapter, the background knowledge, literature review, and the major aims of the research are presented.

Chapter 2 will describe in detail the experimental systems and the measurement methods using in this research. A shadowgraph technique is adopted for measurement of early stage plasma, and the plume plasma is measured by a fluorescence measurement. The spectral emission of the plasma is measured to calculate the electron number density and temperature.

In Chapter 3, comprehensive HD models are established for USLP ablation of metals and semiconductors. They are 2 dimensional, multi-fluid models, consisting of two stages in temporal manner. In the first stage, TTM is used to simulate the energy transfer process inside the target. The electron emission process and ambient gas ionization are

calculated, while the resultant early stage plasma is simulated by a HD model. For the later stage, a HD model is applied to calculate the material removal and plume plasma evolution. The quotidian equation of state (QEOS) model is supplied to calculate the thermal and electrical properties of materials at different conditions.

An integrated atomistic model for DP ablation of semiconductors by USLP is described in Chapter 4. The model includes the molecular dynamics (MD) method for atom motion, the Monte Carlo (MC) method to describe carrier dynamics, the particle-in-cell (PIC) method for particle interaction in plasma, and the beam propagation (BP) method to simulate the laser propagation in air. The interaction between the second pulse and the plasma created by the first pulse is taken account, including laser absorption, reflection, and scattering. The material properties are also provided by the QEOS model and Drude model.

Chapter 5 presents the study of USLP ablation of metals and semiconductors. For ablation of metals, copper and aluminum are used as the study materials. The expansion of the early plasma and the plume plasma are measured and analyzed. The ablation rate at high laser intensity in the ambient environment of vacuum and air are studied. The ablation of silicon is mainly studied for the case of semiconductor. The early plasma dynamics are studied numerically and experimentally, revealing its role in the ablation process in the high intensity range. The Coulomb explosion in the early stage are discovered and analyzed.

The effects and mechanisms of DP ablation of silicon are investigated in Chapter 6. The ablation rate by DP ablation are measured and compared with the case of SP ablation. The mechanisms for ablation enhancement under different conditions are analyzed. Plasma emission spectrums are measured to calculate the plasma temperature and electron number density changes with time for different delay times, which are used to validate the model prediction. The reason for plasma enhancement phenomenon is revealed and the optimum conditions for the enhancement of material removal and plasma are determined.

Conclusions of this study and recommendations of future study are presented in Chapter 7.

2. EXPERIMENTAL METHODS

This chapter presents the diagnostic systems and measurement techniques used in this research. First, the details of the major components in the experimental setup are described. Then, the experimental setups and measurement methods are introduced for different measurement purposes, including shadowgraphic measurement of early stage plasma, fluorescence measurement of plume plasma, spectral measurement of electron temperature and number density in plasma.

2.1 Experimental Apparatus

The major components of the experimental systems used in this research are introduced in this section, including a femtosecond laser, an ICCD camera, and a spectrometer.

2.1.1 Femtosecond Laser

The laser system used in this research is a regeneratively amplified Ti:sapphire laser (Spitfire, Spectra Physics). It has the pulse duration of 100 fs, the wavelength of 800 nm, and the repetition rate of 1 kHz. The output laser pulse energy is 1 mJ per pulse. To adjust the laser pulse energy, a half waveplate and a polarizer are set in front of the laser, and the laser pulse energy can be varied from 5μJ to 1 mJ. The output laser beam has a Gaussian profile for spatial distribution, and the $1/e^2$ diameter (the largest distance between two points where the intensity falls to $1/e^2 = 0.135$ times of the peak value) is 4.8 cm, which is measured by an optical beam profiler (Spiricon, USB L130). Figure 2.1 shows the beam profile of the output laser beam at the laser pulse energy of 70 μJ.

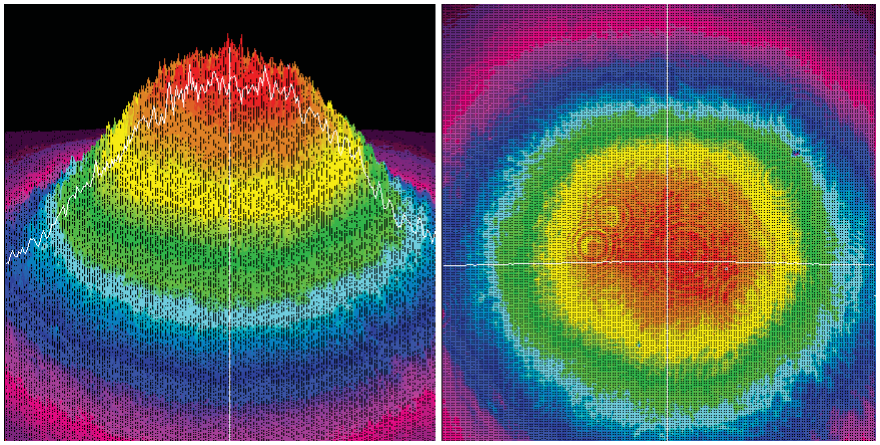

(a) (b)

Figure 2.1. 3D (a) and 2D (b) beam profiles of the output laser beam from the laser system used in this research. Pulse duration: 100 fs, wavelength: 800 nm, and laser pulse energy: 70 μJ.

2.1.2 ICCD Camera

The ICCD camera (PI-MAX2, Princeton Instruments) is one of the key components in the experimental measurements listed in this research project. It was used to take the images in the measurements of the early and plume plasma evolutions, and also as the detector of the spectral lines of the plasma emission for the measurements of electron temperatures and number densities. A CCD chip is contained in the ICCD camera. The array size is 1024 pixels × 1024 pixels, and the resolution is 13 μm per pixel. The detectable wavelength range of the camera is from 200 nm to 900 nm.

The camera can be operated in two modes: the shutter mode and the gate mode. A ST-133 controller (DG535 installed) is cabled to the camera to provide the triggering signals, and control the scan and exposure timing. In the shutter mode, the intensifier gating is under the control of signals from the ST-133, and the camera could be run freely. This mode is proper for taking images in a large time scale (μs or longer). In the gate mode, the camera can be triggered by external signals and turned on for a controllable period of time, which is called gate width. The shortest gate with of the camera is below 2 ns. This mode is good for taking images in a short time scale (ns or shorter). In this

research project, the experimental measurements mainly used the gate mode, since the early stage phenomena of the ablation process is the main research object.

2.1.3 Spectrometer

A spectrometer (iHR 550, Horiba Jobin Yvon) is used in the research to measure the emission spectrums of the generated plasma. It has a focal length of 550 mm, and the entrance aperture ratio of f/6.4. Three gratings are contained in the spectrometer, including two gratings with 1200 gr/mm, and one with 1800 gr/mm. The 1200 gr/mm grating was mainly adopted in this research, the spectral range of which is 150 nm to 1500 nm. The spectral resolution is 0.025 nm, and the spectral dispersion is 1.37 nm/mm.

2.2 Experimental Systems and Measurement Techniques

In this section, the experimental setups and methods are introduced. A shadowgraphic measurement system is established to measure the evolution of early stage plasma. The plume plasma dynamics is measured by fluorescence measurement. Besides, the electron number density and temperature inside the plasma are detected by the measurement of the emission spectrums of the plasma.

2.2.1 Early Plasma Measurement

The schematic of the experimental setup for the early plasma measurement is shown in Figure 2.2, which was established in the previous study of Hu et al. (2011a). For the shadowgraph measurement, a beam splitter split the laser beam into two parts, one applied as the pump pulse and the other as the probe pulse. The pump laser beam was used to ablate the target and was focused onto the target by a 10×microscope objective with a numerical aperture of NA = 0.30 and a focal length of f = 8.3 mm. The objective was mounted on a translational stage in order to accurately (1 μm) control the focal point position. The probe laser beam was used to measure the formed plasma by shadowgraphy, the wavelength of which was halved to 400 nm by a second-harmonic generator (SHG).

After being adjusted and optimized by a beam reducer, two focal lenses and an optical iris, the probe pulse irradiated the generated plasma above the target surface, forming the shadowgraph images into the ICCD camera through two objective lenses. A band-pass filter for 400 nm was used to block the pump beam and the background light, only allowing transmission of the probe beam.

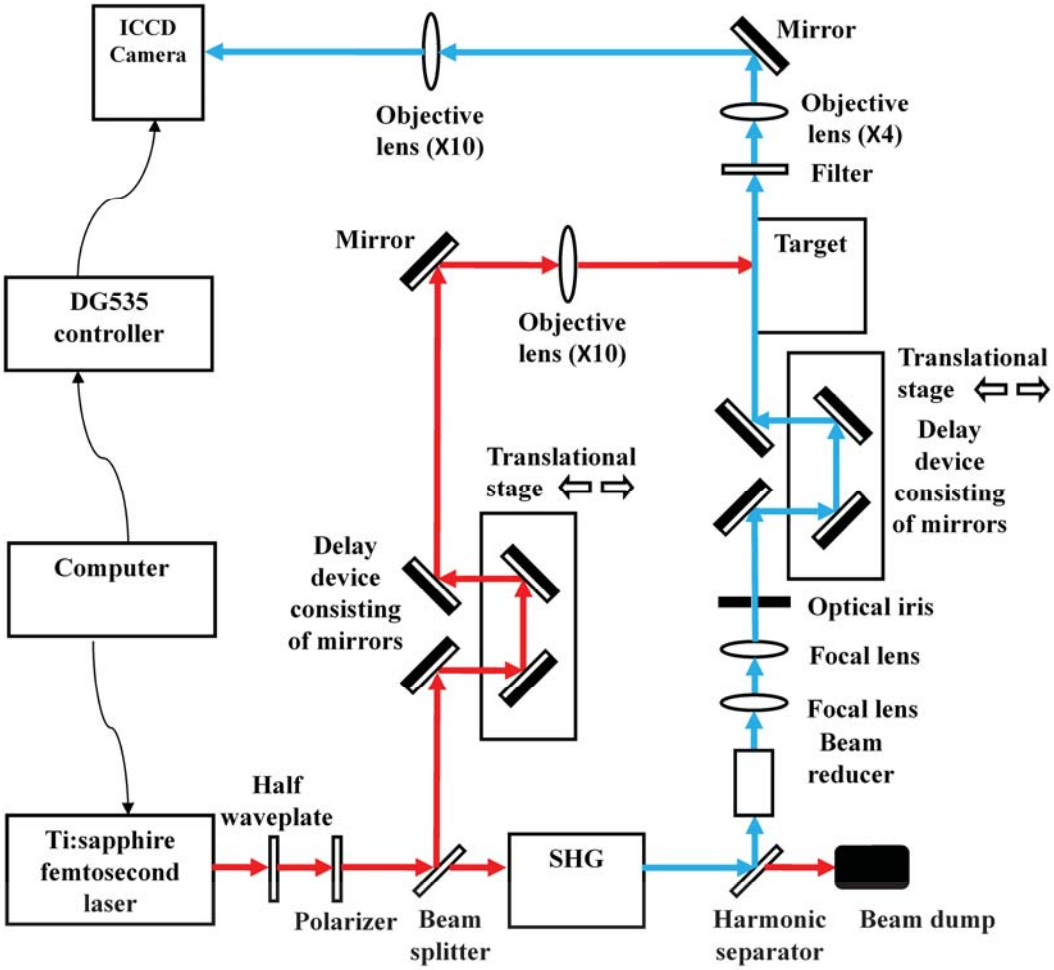

Figure 2.2 Experimental setup for plasma measurement by shadowgraphy.

Two delay devices consisted of mirrors and translational stages were inserted into the paths of both probe and pump beams to control the delay time between them. The translational stages have the accuracy of 1 μm, and hence provide a time resolution of 1 fs for the delay time. With the delay devices, it is possible to measure the plasma

evolution in the very early stage (within 1 ps). The synchronization between the pump and probe pulses were adjusted by two steps. First, the pulse profiles of them detected by two photodiodes were measured by an oscilloscope (DS1302CA, Rigol). The delay devices were moved until two profiles overlapped with each other. Considering the temporal resolution of the oscilloscope and the photodiodes, the accuracy of this step was about 20 ps. To improve the accuracy, the synchronization was further adjusted by observing the formation of filament (air breakdown) via the ICCD camera. The moment when the air breakdown occurred and observed by the ICCD camera was determined to be the instant when the two beams overlap and the zero time point. Since the time for air breakdown to occur is only several femtoseconds, an accuracy of several femtoseconds was achieved in this step.

2.2.2 Plume Plasma Measurement

For the direct fluorescence measurement, a 10× microscope objective was used to focus the laser beam onto the target to ablate the target. The focal point position could be accurately adjusted (1 μm) by the translational stage. The fluorescence emission of the generated plasma passed through a doublet and a 4× microscope objective lens, forming images into the ICCD camera. A filter for $\lambda > 650$ nm was applied to block the scattered laser beam and the background light. The position of plasma front was defined as the location where the fluorescence intensity was 20% of the strongest intensity in the centre of the plasma.

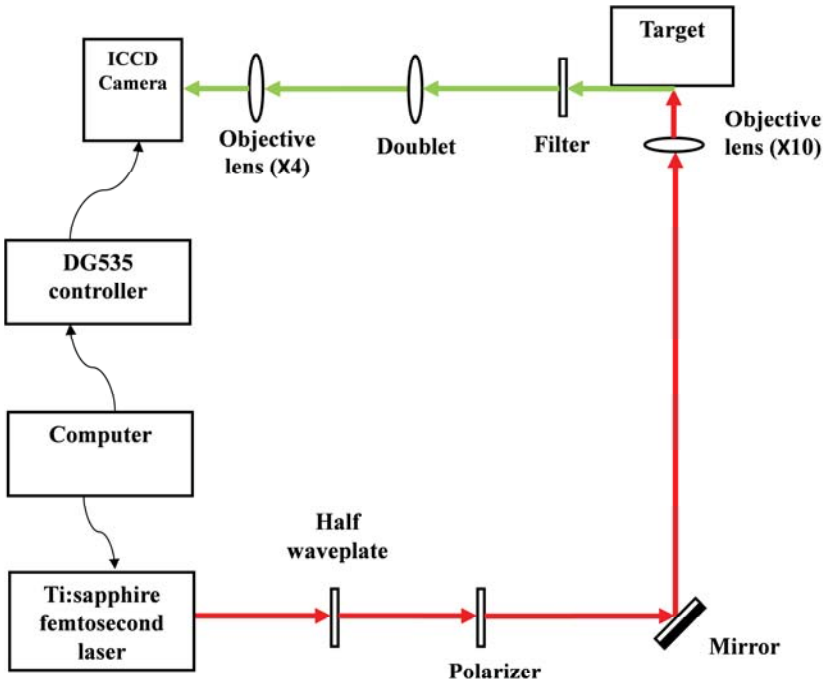

Figure 2.3 Experimental setup for plasma measurement by fluorescence.

2.2.3 Double-Pulse Ablation and Spectrum Measurement

The DP ablation setup (Figure 2.4) is similar to the system for the shadowgraphic measurement of early plasma in Figure 2.2. Instead of using one single pulse, a Mach-Zehnder interferometer was developed to generate two pulse replicas with the same pulse characteristics. The temporal overlap between two pulses was achieved by measuring the two-photon absorption signal in a photodiode. The pulse delay was accurately controlled from several fs to 100 ps by delay devices with the precision of several femtoseconds. A polarizer and a half-waveplate were adopted to control the pulse energy of each pulse. The pump pulses were focused onto the target (silicon wafer) surface by a 10X microscope objective with a numerical aperture of NA = 0.30 and a focal length of f = 8.3 mm. The plasma emission signal was delivered into a spectrometer and formed the spectrum images on an ICCD camera. A focal lens set in front of the spectrometer collects the emitted light from the plasma and focuses it into the slit of the spectrometer.

Therefore, the numerical aperture (N.A.) of the spectrometer and the focal lens should be similar. In this experiment, the spectrometer has a N.A. of 6.4, while the focal lens has a value of 5.9, which are close enough to each other. A beam splitter (BS2) created a probe beam, which aimed to help align the setup.

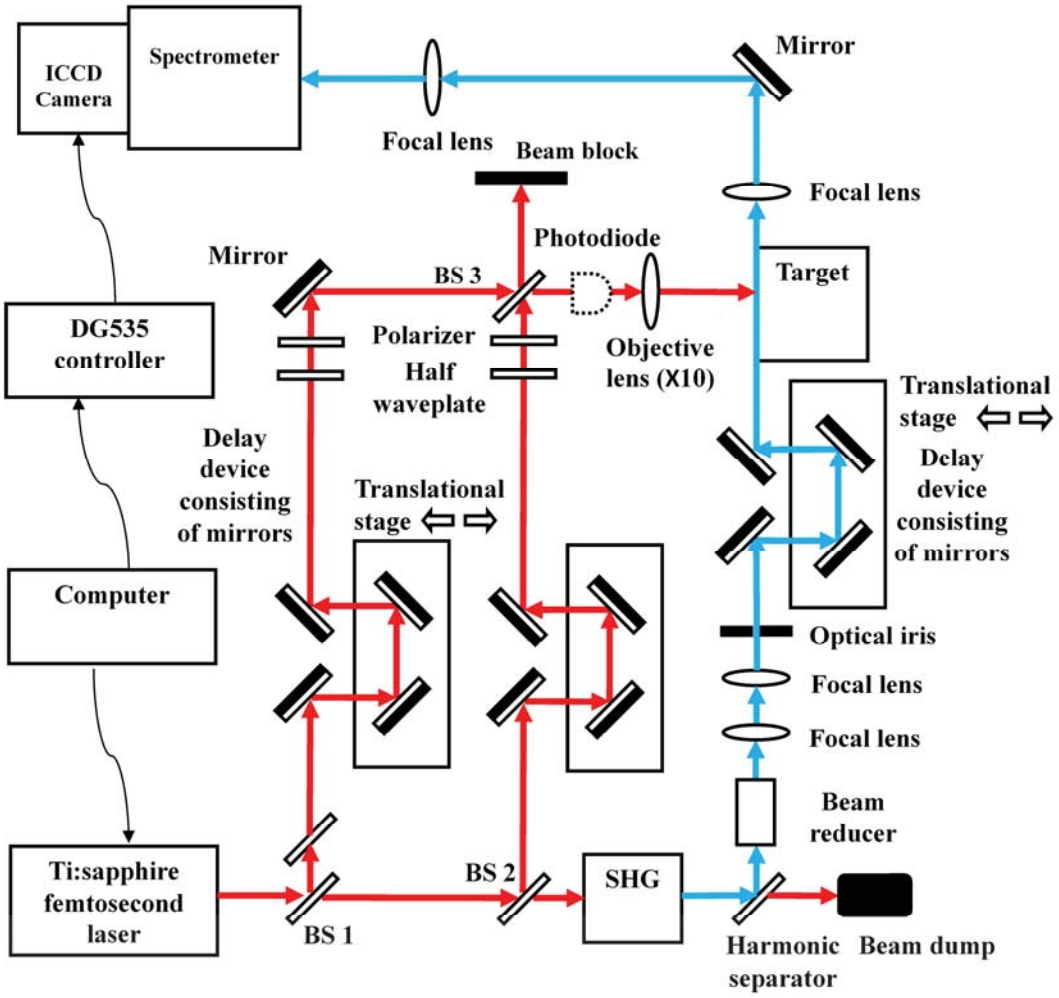

Figure 2.4 Experimental setup for spectral measurement.

3. HYDRODYNAMIC MODEL FOR USLP ABLATION

Hydrodynamic (HD) models for USLP ablation of both metals and semiconductors will be presented in this chapter. The models account for all the important physical mechanisms during the USLP-matter interaction, including laser energy absorption, energy transfer inside the target, early stage plasma generation and expansion, and plume expansion. They are 2 dimensional (2D) axisymmetric models, which are sufficient to describing the three dimensional behavior for laser beams with axisymmetric profiles. The whole ablation process is divided into two stages in temporal manner in the models. In the first stage, a two temperature model (TTM) is used to simulate the energy transfer process inside the target. The electron emission process and ambient gas ionization are calculated, while the resultant early stage plasma is simulated by a two-dimensional multi-fluid HD model. For the later stage, a comprehensive HD model is applied to calculate the plume plasma evolution, including electrons, ions and atoms from both the target and ambient gas, which is modified from the HD model developed by Wu et al. (2007b) for nanosecond laser ablation. The quotidian equation of state (QEOS) model (More et al., 1988; Wu et al., 2007c) is supplied to calculate the thermal and electrical properties of materials at different conditions.

3.1 Hydrodynamic Model for Metals

The schematic diagram for the model setup is shown in Figure 3.1. The metal target is located in $z<0$ region, and the ambient environment is in the region where $z>0$. The metal-ambient interface is located at $z=0$, and the symmetric axis is at $r=0$. The laser beam travels along $-z$ direction, irradiating perpendicularly on the target. The model is divided into two stages. The first stage covers the first several hundreds of femtoseconds, when the lattice is relatively cool and remains in solid state. In this stage, the ionization

of the ambient gas assisted by hot electron emission through the target surface forms the early stage plasma. The second stage starts when the lattice is heated to a high temperature, during which the chemical bonds among material atoms are broken and material removal starts with the formation of plume plasma.

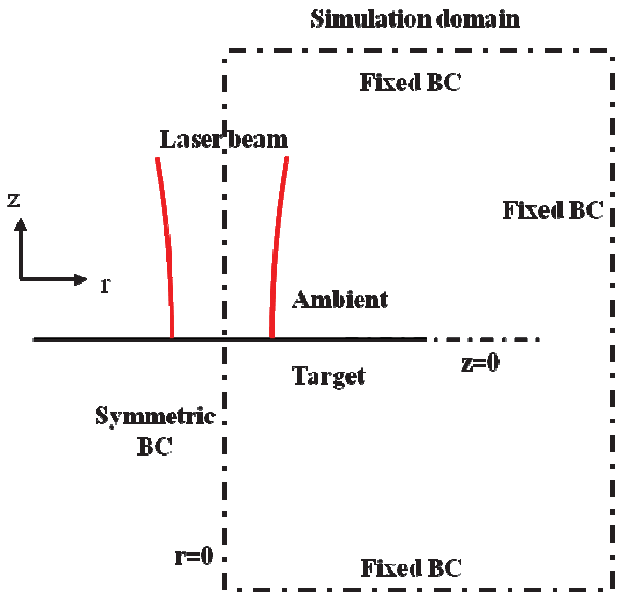

Figure 3.1. Schematic diagram of the model setup.

3.1.1 The First Stage

In this stage, the nearly-free electrons in metal target absorb the laser energy, coupling with the surrounding electrons and phonons. There will be hot electron emission from the target surface and ionize the ambient gas (not for the ablation in vacuum). Early plasma will be generated in this stage.

3.1.1.1 Laser Profile and Air Breakdown

The laser beam has a Gaussian profile and is focused by an external focal lens. The power density distribution is calculated as:

$$I(r,z) = 2I_0(\frac{w_0}{w(z)})^2 \exp(\frac{-2r^2}{w^2(z)}), \tag{3.1}$$

where I_0 is the average power density over the focal spot (beam waist), w_0 is the beam waist size, and $w(z)$ is the radius of the beam spot at distance z given by:

$$w(z) = w_0\sqrt{1+(\frac{z}{z_R})^2}, \tag{3.2}$$

where $z_R = \frac{\pi w_0^2}{\lambda}$ is the Rayleigh range, λ is the laser wavelength.

For the case of ablation in air, the air molecules can be directly ionized by the incident laser beam at high enough laser intensity. At relatively low laser intensity, multi-photon ionization (MPI) is dominating, and tunneling ionization (TI) is important in the high intensity range. The switch point of the two mechanisms is determined by the Keldysh parameter γ_K (Keldysh, 1964):

$$\gamma_K = 2.31\times10^6(\frac{\varepsilon_{ion}}{I\lambda^2})^{1/2}, \tag{3.3}$$

where ε_{ion} is the ionization potential.

At low laser intensity ($\gamma_K \gg 1$) MPI dominates, and its ionization rate is calculated as (Stuart et al., 1996; Lin et al., 2009):

$$R_{MP} = \sigma_k[I/\hbar\omega]^k n_{ga}, \tag{3.4}$$

where σ_k is the cross section for *k*-photon collision, $\hbar$ is the reduced Planck constant, ω is the photon frequency, and n_{ga} is the atom number density in air.

In the laser intensity range even higher ($\gamma_K \ll 1$),TI becomes more important. In an intense electric field, the potential barrier of an atom (molecule) is drastically distorted. Hence, electrons can easily escape from the atom and ionize the neutral atoms. The rate of TI can be calculated by the Perelomov-Popov-Terent'ev (PPT) developed by Perelomov et al. (1966).

The ionized charged particles will assist and enhance further air breakdown by impact ionization (II), the rate of which is given by (Raizor, 1965, Couairona and Mysyrowicz, 2007, Lin et al., 2009)

$$R_{IMP} = \sigma_{IMP} I n_e \tag{3.5}$$
$$\sigma_{IMP} = \frac{e^2}{\varepsilon_0 m_e c n_0} \frac{\tau_e}{(1+\omega^2 {\tau_e}^2)},$$

where σ_{IMP} is the cross section for II, n_e is the electron number density, e is the elementary charge, ε_0 is the vacuum permittivity, m_e is the electron mass, c is the speed of light, n_0 is the refractive index in vacuum, and τ_e is the electron relaxation time.

3.1.1.2 Laser Absorption

Both the collisional and collisionless absorptions are considered in the model. The collisional absorption is the most common term considered for femtosecond laser ablation, and can be calculated by:

$$S(r,z,t) = (1-R)\alpha I_{surf}(r,z,t) exp(-\alpha z), \tag{3.6}$$

where R is the surface reflectivity and α denotes the absorption coefficient, which are calculated based on Drude theory (Ginzburg, 1962; Pedrotti et al., 1993; Vidal et al., 2001). I_{surf} is the laser intensity reaching the target surface, which is assumed to have a Gaussian profile for both spatial and temporal distributions.

The absorption coefficient α is determined by the effective collisional frequency between electrons and other particles. At low electron temperature ($T_e < T_F$, T_F is the Fermi temperature), the target material is still in cold solid state, and the total collision process contains the electron-electron (υ_{e-e}) and electron-phonon (υ_{e-ph}) collision (Agranat et al., 2007):

$$\upsilon_{eff} = v_{e-e} + v_{e-ph} \tag{3.7}$$
$$\upsilon_{e-e} = \frac{A_T T_e^{\,2}}{\hbar T_F}$$
$$\upsilon_{e-ph} = \frac{k_\varepsilon e^2 T_i^2}{\hbar^2 v_F},$$

where T_e and T_i are temperature of lattice and electrons, v_F is the Fermi velocity, k_ε and A_T are constants. Besides, there is a limitation for υ_{eff}:

$$\upsilon_{eff} \le \upsilon_C \frac{\sqrt{{v_F}^2 + T_e / m_e}}{r_0}, \tag{3.8}$$

where r_0 is the ion radius. This criterion comes from the condition that the electron mean free path cannot be smaller than ion radius. In this range, the collision frequency will increase with the lattice and electron temperature, which will rise with the laser intensity.

For $T_e > T_F$, the material will be considered as the hot plasma state, the collision frequency will be given as (Hora, 1975, Lima et al., 1979):

$$\upsilon_{eff} = \frac{4(Ze^2)^2 N_a}{\pi^{1/2} a^2 m_e^2 v_e^2} \int d^3k \frac{(\vec{k}\cdot\vec{a})^2}{k^5 \left|\varepsilon_{eff}(\vec{k})\right|^2} \left(\frac{k_d^2}{k^2} - 1\right) e^{-k_d^2/k^2}, \tag{3.9}$$

where Z is the number of electrons of a atom, N_a is the density of atoms, v_e is the electron velocity, $\vec{a} = e\vec{E} / m_e\omega$ is the electron oscillation amplitude, $\vec{k}$ is the wave vector, $\vec{E}_0$ is the electric field strength induced by laser pulse, $\varepsilon_{eff}(\vec{k})$ is the dielectric function of the material, $k_d = \omega_p / v_e$, $\omega_p = \sqrt{4\pi e^2 n_e / m_e}$ is the plasma frequency.

Eqn. (3.9) can be simplified at different limitations. For moderate laser intensity ($\frac{e^2E^2}{2m_e\omega^2} \ll \hbar\omega$), only single photon scattering and absorption is involved. Eqn. (3.9) can be simplified to (Seely and Harris, 1973):

$$\upsilon_{eff} = \frac{4}{3}\left[\frac{(2\pi)^{\frac{1}{2}} Z^2 e^4 N_a L}{m_e^2 v_e^3}\right], \tag{3.10}$$

L is the Coulomb logarithm defined by

$$L = \int_{\theta_{min}}^{\pi} \cot\frac{1}{2}\theta d\theta, \tag{3.11}$$

where $\theta_{\min}$ is the lower cutoff of the scattering angle.

However, when the intensity becomes higher, it is possible for an electron to collide with and absorb several photons simultaneously. When the intensity becomes higher ($\frac{e^2E^2}{2m_e\omega^2} \gg \hbar\omega$), the collision frequency is given as (Seely and Harris, 1973):

$$\upsilon_{eff} = \frac{8\pi^2 N_a Z^2 e m_e \omega^3}{E^3}, \tag{3.12}$$

Between these two regimes, the transition region will be described by the harmonic mean of Eqn. (3.10) and Eqn. (3.12) (Eidmann et al., 2000):

$$v_{eff}^{-1} = (\frac{4}{3}\left[\frac{(2\pi)^{\frac{1}{2}} Z^2 e^4 N_a L}{m_e^2 v_e^3}\right])^{-1} + (\frac{8\pi^2 N_a Z^2 e m_e \omega^3}{E^3})^{-1} . \quad (3.13)$$

At high laser intensity, because of the quick drop of the collisional absorption rate (Price et al., 1995; Eidmann et al., 2000), collisionless absorption becomes important and needs to be taken into account. The energy transfer process from the laser radiation to the matter should obey the Poynting's theorem ((Born and Wolf, 1970)):

$$\frac{\partial u}{\partial t} + \nabla \cdot \vec{S}_p = -\vec{J}_e \cdot \vec{E} \quad (3.14)$$

,

where $\vec{E}$ is the electric field intensity, $\vec{B}$ is the magnetic field density, $u = (\varepsilon_0 \vec{E}^2 + \vec{B}^2 / \mu_0)/2$ is the energy density of the laser electromagnetic field, and $\vec{S}_p = c^2 \varepsilon_0 \vec{E} \times \vec{B}$. The absorbed energy *S* is determined by the source term $-\vec{J}_e \cdot \vec{E}$. ($\vec{E}$, $\vec{B}$) are calculated from the Maxwell equations:

$$\begin{aligned} &\nabla \cdot \vec{E} = 0 \\ &\nabla \cdot \vec{B} = 0 \\ &\nabla \times \vec{E} = -\partial \vec{B} / \partial t \\ &\nabla \times \vec{B} = \mu_0 \vec{J}_e + \mu_0 \varepsilon_0 \partial \vec{E} / \partial t \end{aligned} \quad (3.15)$$

,

where ε_0 and μ_0 are permittivity and permeability, respectively, and $\vec{J}_e$ is the electric current density including both drift and diffusion terms:

$$\vec{J}_e = en_e\mu_e\vec{E} + eD_e\nabla n_e, \tag{3.16}$$

where μ_e and D_e are the carrier mobility and diffusivity, respectively.

3.1.1.3 Energy Transfer Inside Target

The energy transfer inside the material is described by the two dimensional TTM (Qiu and Tien, 1993; Tzou, 1995):

$$\begin{aligned} C_e\frac{\partial T_e}{\partial t} &= \frac{1}{r}\frac{\partial}{\partial r}\left(k_e r\frac{\partial T_e}{\partial r}\right) + \frac{\partial^2 T_e}{\partial z^2} - G\left(T_e - T_i\right) + S \\ C_i\frac{\partial T_i}{\partial t} &= G\left(T_e - T_i\right) \end{aligned}, \tag{3.17}$$

where C_e, C_i, T_e, T_i are the volumetric heat capacities and temperatures of electrons and lattice, respectively, k_e is the electron thermal conductivity, all the values of which are obtained from QEOS model (More et al., 1988), which was developed by Wu et al. (2007b). The electrons and lattice are treated as two separate systems, interacting with each other through electron-phonon coupling term G (Laville et al., 2002). It is assumed that during this stage, electrons are in local thermal equilibrium and the lattice stays in solid state.

3.1.1.4 Surface Electron Emission

By absorbing the laser energy, the electrons near the target surface will be heated to a very high temperature, such that the electrons can gain enough kinetic energy to break the attraction of the lattice and escape from the target surface, initiating the surface electron emission. There are two important electron emission mechanisms: thermal emission and photoelectric emission. The thermal electron emission rate is determined by Richardson's equation (Herring and Nichols, 1949; Bechtel et al., 1977):

$$J_{th} = AT_{es}^2 \exp\left(-\frac{\Phi}{k_B T_{es}}\right), \tag{3.18}$$

where T_{es} is the surface electron temperature, A is a universal constant equal to 120 A/cm^2K^2, and Φ is the work function of the material.

The n-photon photoelectric emission rate can be written as (Bechtel et al., 1977, Chen and Mao., 2008):

$$J_n = \alpha_n \left(\frac{e}{h\upsilon}\right)^n A I^n \left(1-R\right)^n T_{es}^2 F\left[\frac{nh\upsilon - \Phi}{k_B T_{es}}\right], \tag{3.19}$$

where α_n is the n-photon photoelectric emission coefficient, which is for the current case, we use $\alpha_3 = 10^{-45} cm^2 s^{-2}$, and F represents the Fowler function which is discussed in Yen et al. (1980) and Girardeau-Montaut and Girardeau-Montaut (1995).

The total electron flux in z direction at the target surface is given by:

$$J_z = J_n + J_{th}. \tag{3.20}$$

Usually, at room temperature, the thermal emission rate is neglectable. However, as shown in eqn. (3.18), the emission rate will increase rapidly as the temperature becomes higher. Therefore, the initiation of thermal emission requires some time for the increase of temperature. Based on eqn. (3.19), the emission rate of n-photon photoelectric emission is proportional to I^n, while it is also affected by the surface temperature.

3.1.1.5 Electron (ion) Dynamics Inside Target

Because of the electron emission at the target surface, there will be electron transport from the bulk to the target surface. The electron and ion dynamics inside the target is described as (Mao et al., 1998; Bulgakova et al., 2005b):

$$\frac{\partial n_e}{\partial t} - \frac{1}{e}\nabla \cdot \vec{J}_e = 0 \qquad (3.21)$$
$$\frac{\partial n_i}{\partial t} + \frac{1}{e}\nabla \cdot \vec{J}_i = 0,$$

where n_e (n_i) is the electron (ion) number density, and $\vec{J}_e$ ($\vec{J}_i$) is the electric current density for electron (ion) including both drift and diffusion terms.

At the metal-air interface, the electric current density in z direction is determined by the surface electron emission rate. The electron current density in r direction is continuous through the interface. They are implemented as the boundary conditions for the calculation of early stage plasma, together with the surface electron temperature and electron's thermal velocity. The material ions flux is determined by Eqn. (3.21), and performs as the boundary condition at the metal-air interface for the simulation of material ions inside the plasma.

3.1.1.6 Plasma Dynamics

The ejected electrons from target surface will ionize the ambient gas and form an early stage plasma. The early plasma and ambient gas dynamics are simulated by a 2D HD model in the region z>0 using the models given below.

For electrons inside the plasma:

$$\frac{\partial n_e}{\partial t}+\nabla\cdot(n_e\vec{v}_e)=S_e$$
$$\frac{\partial \vec{p}_e}{\partial t}+\nabla\cdot(\vec{p}_e\vec{v}_e)=-\nabla(P_e)+n_e\vec{f}_e \quad . \tag{3.22}$$
$$\frac{\partial \varepsilon_e}{\partial t}+\nabla\cdot(\varepsilon_e\vec{v}_e)=-\nabla\cdot(P_e\vec{v}_e)-\nabla\cdot\vec{q}_T+Q_{IB}+Q_c+Q_{imp}+Q_{rec}$$

For material ions inside the plasma:

$$\frac{\partial n_{ti}}{\partial t}+\nabla\cdot(n_{ti}\vec{v}_{ti})=0$$
$$\frac{\partial \vec{p}_{ti}}{\partial t}+\nabla\cdot(\vec{p}_{ti}\vec{v}_{ti})=-\nabla(P_{ti})+n_{ti}\vec{f}_{ti} \quad . \tag{3.23}$$
$$\frac{\partial \varepsilon_{ti}}{\partial t}+\nabla\cdot(\varepsilon_{ti}\vec{v}_{ti})=-\nabla\cdot(P_{ti}\vec{v}_{ti})-\nabla\cdot\vec{q}_T+Q_c+Q_{imp}+Q_{rec}$$

For ambient gas (ions and neutral atoms):

$$\frac{\partial n_{gi}}{\partial t}+\nabla\cdot(n_{gi}\vec{v}_{gi})=S_{gi}$$
$$\frac{\partial n_{ga}}{\partial t}+\nabla\cdot(n_{ga}\vec{v}_{ga})=S_{ga}$$
$$\frac{\partial \vec{p}_g}{\partial t}+\nabla\cdot(\vec{p}_g\vec{v}_g)=-\nabla(P_g)+n_{gi}\vec{f}_{gi}+n_{ga}\vec{f}_{ga} \quad . \tag{3.24}$$
$$\frac{\partial \varepsilon_g}{\partial t}+\nabla\cdot(\varepsilon_g\vec{v}_g)=-\nabla\cdot(P_g\vec{v}_g)-\nabla\cdot\vec{q}_T+Q_c+Q_{imp}+Q_{rec}$$

where $\vec{p}_{e(ti,g)}=m_{e(ti,g)}n_{e(ti,g)}\vec{v}_{e(ti,g)}$ is the electron (target ion, gas) momentum, $P_{e(ti,g)}=n_{e(ti,g)}k_BT_{e(ti,g)}$ is the electron (target ion, gas) pressure, and $\varepsilon_{e(ti,g)}=1.5n_{e(ti,g)}k_BT_{e(ti,g)}+0.5m_{e(ti,g)}n_{e(ti,g)}v_{e(ti,g)}{}^2$ is the total energy of electron (target ion, gas) with $m_{e(ti,g)}$ as the electron (target ion, gas) mass, k_B as the Boltzmann constant, and $\vec{v}_{e(ti,g)}$ as the electron (target ion, gas) velocity. $T_{e(ti,g)}$ is the electron (target ion, gas)

temperature. Here ejected electrons and ambient gas are treated as ideal gases in thermal equilibrium.

$S_{e(gi,ga)}$ is the source term for electron (gas ion, gas atom) generation in the bulk of the plasma. It is due to the II, MPI and recombination, and therefore, can be written as:

$$S_e = S_{gi} = -S_{ga} = R_{imp}(\varepsilon,x,t) + R_{pi}(\varepsilon,x,t) + R_{rec}(\varepsilon,x,t). \tag{3.25}$$

where $R_{imp}(\varepsilon,x,t) = -\nu_i(\varepsilon)n_e(\varepsilon) + 4\nu_i(2\varepsilon+U_I)n_e(2\varepsilon+U_I)$ is the II rate (Apostolova and Hahn, 2000), where $\nu_i(\varepsilon) = 1.5(\frac{\varepsilon}{U_I}-1)^2$, U_I is the ionization energy of the atoms. $R_{pi}(\varepsilon,x,t) = \sigma_k[I/h\nu]^k n_{ga}$ is the MPI rate (Stuart et al., 1996; Lin et al., 2009), where σ_k is the cross section for k-photon collision.

$R_{rec}(\varepsilon,x,t) = 2^{3/2} r(\varepsilon) n_e{}^2 \left(\frac{\varepsilon - U_I}{2}?\, t\right) - 2^{7/2} r(2\varepsilon+U_I) n_e{}^2(\varepsilon?\, t)$ is the three body recombination rate, where $r(\varepsilon) = 1.5C(\frac{1}{U_I m_e})^{1/2}(\frac{\varepsilon}{U_I}-1)(\frac{\varepsilon}{U_I})^{1/2}$, $C = \frac{\hbar^3\pi^2}{2m_e}\frac{g_0}{g_1}\frac{n_i}{n_a}$, g_0 and g_1 are the degeneracy factors of the ionic levels.

$\vec{f}_{e(i,a)}$ is the force term, which consists of electric forces, collision forces and ponderomotive force (Bulgakova et al., 2007). For electrons,

$$\vec{f}_e = e\vec{E} + \vec{f}_{e-i} + \vec{f}_{e-a} + \vec{f}_p. \tag{3.26}$$

$e\vec{E}$ is the electric force, where *e* is the unit electric charge and $\vec{E}$ is the electric field due to the presence of the electrons and ions in the plasma, and can be obtained by solving the Poisson equation at every time step. $\vec{f}_{e-i}$ and $\vec{f}_{e-a}$ result from elastic collisions between electrons and ions and atoms, respectively, which can be written as $\vec{f}_{e-i(a)} = \upsilon_{ei(a)} m_e(\vec{v}_e - \vec{v}_{i(a)})$, where $\upsilon_{ei(a)}$ is the electron-ion (atom) collision frequency.

$\vec{f}_p$ is the ponderomotive force term induced by the laser induced electric field variation. It is given as (Khishchenko et al., 2008)

$$\vec{f}_p = -K_1\left(\epsilon^{\omega}\right)\frac{Zm_e}{4m_i}\frac{e^2}{m_e^2\omega^2}\frac{\partial|E|^2}{\partial\vec{r}}, \tag{3.27}$$

where $\epsilon^{\omega} = 3\sqrt{\pi}v_{eff}(4\omega)^{-1}$, $K_1(r,z)$ is the integral function:

$$K_1(r,z) = \frac{8}{3\sqrt{\pi}}\int_0^{\infty}\frac{t^{10}\exp(-t^2)}{t^6+x^2}dt .$$

For ions,

$$\vec{f}_i = q\vec{E} + \vec{f}_{i-e} + \vec{f}_{i-a} . \tag{3.28}$$

For atoms, there is no electric force, so

$$\vec{f}_a = \vec{f}_{a-i} + \vec{f}_{a-e} . \tag{3.29}$$

$\vec{q}_T$ is the thermal flux of electron (ion, atom) by conduction, which is given by $\vec{q}_T = K'T_{e(i,a)}\nabla T_{e(i,a)}$, where K' is defined by Spitzer and Haem (1953). $Q_{IB} = \alpha I$ is the absorption rate of inverse Bremsstrahlung by early plasma and α is the inverse Bremsstrahlung absorption coefficient (Vidal et al., 2001; Konstantin et al., 2008).

Q_c, Q_{imp} and Q_{rec} are the energy terms generated by collision, II, and recombination, respectively, which for electrons are given by Chen and Mao (2008):

$$Q_c = \frac{3m_e}{m_a} n_e k_B \left[\left(T_e - T_a \right) \upsilon_{ea} + \left(T_e - T_i \right) \upsilon_{ei} \right] \tag{3.30}$$
$$Q_{imp} = -v_z n_a E_p$$
$$Q_{rec} = -0.5 v_r n_i \left(3k_B T_e + m_e v_e^2 \right) + v_r n_i E_p,$$

where v_z is the II frequency, E_p is the ionization potential, and v_r is the three body recombination frequency. For ions and atoms, the expressions are similar.

3.1.2 The Second Stage

In the second stage, the target temperature is high enough to generate the plume plasma. A two dimensional hydrodynamic model is implemented to simulate the plume plasma expansion in the whole simulation domain, which was modified from the HD model developed by Wu et al. (2007b) for nanosecond laser ablation. The material ions and ambient gas are assumed to be in local thermal equilibrium inside the plasma and the heat exchange terms are neglected, while the spatial heat diffusion terms are still included. The governing equations are given based on the conservation of mass, momentum and energy:

$$
\begin{aligned}
&\frac{\partial n_e}{\partial t}+\nabla\cdot(n_e\vec{v}_e)=S_e \\
&\frac{\partial \vec{p}_e}{\partial t}+\nabla\cdot(\vec{p}_e\vec{v}_e)=-\nabla(P_e)+n_e\vec{f}_e \\
&\frac{\partial \varepsilon_e}{\partial t}+\nabla\cdot(\varepsilon_e\vec{v}_e)=-\nabla\cdot(P_e\vec{v}_e)-\nabla\cdot\vec{q}_T+Q_{IB}+Q_c+Q_{imp}+Q_{rec} \\
&\frac{\partial n_{ti}}{\partial t}+\nabla\cdot(n_{ti}\vec{v}_{ti})=0 \\
&\frac{\partial n_{gi}}{\partial t}+\nabla\cdot(n_{gi}\vec{v}_{gi})=S_{gi} \\
&\frac{\partial n_{ga}}{\partial t}+\nabla\cdot(n_{ga}\vec{v}_{ga})=S_{ga} \\
&\rho=m_t n_{ti}+m_g(n_{gi}+n_{ga}) \\
&\frac{\partial \vec{p}}{\partial t}+\nabla\cdot\left(\vec{p}\vec{v}\right)=-\nabla\left(P\right)+n_i\vec{f}_i+n_a\vec{f}_a \\
&\frac{\partial \varepsilon}{\partial t}+\nabla\cdot(\varepsilon\vec{v})=-\nabla\cdot(P\vec{v})-\nabla\cdot\vec{q}_T+Q_c+Q_{imp}+Q_{rec}
\end{aligned}
\qquad (3.31)
$$

where ρ is the total density. P, $\vec{p}$ and ε are the total pressure, momentum and energy of metal and ambient gas. In this stage, the laser absorption term is not considered because there is no laser pulse any more. Besides, the hot electron emission can be neglected and the early stage plasma has disappeared.

3.1.3 Initial and Boundary Conditions

The simulation starts at t=0, when the temperature of both the target material and the ambient gas stays in room temperature ($T_e=T_i=300K$), the velocities of electrons, ions and atoms are all zero ($\vec{v}_{e(i,a)}=0$), the total pressure P=1atm. For the first stage, the TTM and the electron dynamics inside the target are first solved in the region where z<0 by the finite volume method. The Poisson equation is solved by a multigrid method in the whole simulation domain. At the metal – air interface, the hot electron emission rates are calculated based on the obtained target surface temperature, and the target material ion flux is calculated by the ion dynamics equation inside the material. These are

implemented as the boundary conditions for eqns. (3.22)-(3.24) for the early plasma. The hydrodynamic equations are solved by convex essentially non-oscillatory (ENO) high order schemes (Liu and Osher, 1998) in the region where z>0 to simulate the early plasma behavior. At the beginning of the second stage, the simulation results of the first stage are applied as initial conditions and eqns. (3.31) are solved in the whole simulation domain to simulate the plume plasma expansion as well as lattice and air properties. In the second stage, the target temperature is greater than the critical temperature, and the interface between the condensed and gaseous phases disappears and is smeared into a macroscopic transition layer (Anisimov et al., 1979). Under such conditions, the contribution of ions from the condensed phase to the plasma region should mainly come from the hydrodynamic expansion, and the laser ablation process should be described by solving the hydrodynamic equations for the whole physical domain, supplemented with wide range equations of state. The simulation domain is chosen to be large enough such that the boundaries of the domain are not disturbed at all. Therefore, fixed boundary conditions are applied at the upper, lower and right boundaries of the simulation domain. At the left boundary (r=0), the values at points left to the r=0 axis is equal to those right to the axis, because of the symmetric properties of the simulation.

3.2 Hydrodynamic Model for Semiconductors

The comprehensive HD model for femtosecond laser ablation of metals has been developed in Section 3.1. The metals contain sufficient free electrons, which will directly absorb the incident laser beam energy via inverse bremsstrahlung absorption. Compared with metals, semiconductors lack free electrons, and the electrons from the valence band must be first excited into the conduction band via interband absorption, leaving positive charged “holes” in the valence band. Therefore, laser energy absorption and the carrier dynamics in semiconductors are different from those in metals. An updated HD model for femtosecond laser ablation of silicon is presented in this section. The model is applicable to sub-picosecond lasers in a wide range of wavelength (200 nm-1064 nm) and laser fluence (up to 100 J/cm^2)

3.2.1 Laser Absorption

Because of the lack of free electrons in semiconductors, the laser beam energy is first absorbed by bonded electrons through interband absorption. The electrons excited into the valence band can further absorb the laser beam energy by inverse bremsstrahlung absorption and increase their temperatures. The total absorption term S can be calculated as (Bulgakova et al., 2005b)

$$S = \alpha I + \beta I^2 + \Theta n_e I - E_g \frac{\partial n_e}{\partial t}. \tag{3.32}$$

where α and β are single- and two-photon absorption coefficient, Θ is the free carrier absorption coefficient, E_g is the band gap of the semiconductor, n_e is the electron number density.

3.2.2 Energy Transfer Inside the Target and Surface Electron Emission

The energy transfer inside the target can be described by the well-known two-temperature model, as described in Section 3.1. Surface electron emission will occur at the target surface, and the total emission rate is the summation of thermal emission rate J_{th} and the n-photon photoelectric emission rate J_n, the same as discussed in Section 3.1. The photoelectric emission takes place when the total photon energy absorbed by surface electrons is higher than the work function to overcome the surface energy barrier. For a wavelength of 800 nm in this study, the photon energy $h\upsilon$ is 1.55 eV, and the work function Φ for silicon is 4.6 eV (Van Driel, 1987). Therefore, three photons are necessary to overcome the work function and three-photon photoelectric emission is expected to be the dominant mechanism. The three-photon emission coefficient is $\alpha_3 = 10^{-30} (cm^2 s / C)^3$ (Mao et al. 1998).

3.2.3 Electron-Hole Dynamics Inside Target

The electron dynamics in silicon are described by (Bechtel et al., 1977; Mao et al., 2000a; Bulgakova et al., 2004) (hole dynamics are similar)

$$\frac{\partial n_e}{\partial t} - \frac{1}{e}\nabla \cdot \vec{J} = G_e - R_e . \tag{3.33}$$

where $\vec{J}$ is the electric current density including both drift and diffusion terms as described in Chapter 3.

In eq. (3.33), G_e and R_e represent the electron generation and loss term, respectively. The term G_e is given by (Bechtel et al., 1977; Mao et al., 2000a; Bulgakova et al., 2004; Bulgakova et al., 2005b)

$$G_e = \frac{(1-R)\alpha I}{h\nu} + \frac{(1-R)^2 \beta I^2}{2h\nu} + \delta n_e \frac{n_a}{n_a + n_i} . \tag{3.34}$$

where α and β are single- and two-photon absorption coefficients, δ is the II coefficient, and n_a, n_i are atom and ion number density, respectively.

The term R_e denotes the three photon Auger recombination process given by (Sebenne et al, 1975)

$$R_e = \gamma n_e^3 . \tag{3.35}$$

with γ being the Auger recombination coefficient.

3.2.4 Plasma Dynamics

The electron and ion dynamics inside the plasma during the laser ablation of semiconductors should have the same governing equations as those of metals described in

Section 3.1.1.6. A 2D multi-fluid hydrodynamic model is used to describe the plasma dynamics during ablation of semiconductors.

4. ATOMISTIC MODEL FOR USLP ABLATION OF SEMICONDUCTORS

A self-closed integrated atomistic model for USLP ablation of semiconductors will be presented in this chapter. It consists of the molecular dynamics (MD) method, the Monte Carlo (MC) method, the particle-in-cell (PIC) method, and the beam propagation (BP) method. The laser propagation in air and the air breakdown were calculated by the 1D BP method, considering MPI, II, and II. The neutral atom motion was simulated by the MD method. The MC method was adopted to analyze the carrier behaviors in the same region. MC/PIC method was added to simulate the particle dynamics in the plasma region, accounting for the long range Coulomb interaction between charged particles. The metallic transition of the liquid silicon was considered by changing the material density and electron number density at the melting point. All the thermal and optical properties of the materials were calculated by the QEOS model and the Drude model developed by Wu et al. (2007c) to account for their variation over a wide range of temperature and density. The integrated model which was originally developed to study the laser-material and laser-plasma interaction for copper by Hu et al. (2011b) has been expanded to deal with semiconductors. The major differences include the interband electronic transition, laser absorption mechanisms, electron-hole pair dynamics, and metallic characteristic of liquid silicon.

4.1 Beam Propagation and Air Breakdown

In this model, the laser propagation in air was simulated by the 1D BP method developed by Hu et al. (2011b), which is given as:

$$\frac{\partial A}{\partial z} = ikn_2 |A|^2 A - \frac{\sigma}{2}(1+i\omega\tau)n_e A - \frac{\varepsilon_{ion}}{2}\frac{\partial n_e}{\partial t}\frac{A}{|A|^2}, \quad (4.1)$$

where A is the electric field envelope function, z denotes the laser propagation direction, i represents the imaginary unit, k is the wave number, n_2 is the optical Kerr coefficient, σ represents the cross section for electron-neutral inverse bremsstrahlung, τ denotes the electron collision relaxation time, ε_{ion} is the ionization potential, and n_e denotes the free electron number density. The effects of the optical Kerr effect, the IB collision, and the energy losses due to ionization (MPI, TI, II) processes are considered in the three terms on the right-hand side, respectively. This 1D BP method calculates the laser electric field variation in the laser propagation direction, but does not consider the laser profile change in the radial direction. It is valid because the laser profile in the radial direction does not change significantly under the conditions in this study.

During laser propagation in air, laser self-focusing and defocusing are two important competing processes. With the laser power higher than the critical power given by Couairon and Mysyrowicz (2007), laser self-focusing occurs because of the change of the refractive index of the air, which act as a focusing lens to enhance the laser focusing. On the other hand, a high enough laser power will trigger air breakdown and a large amount of atoms in air are ionized by MPI or TI processes, forming the air plasma. The subsequent IB and II processes will further assist the air breakdown process and enhance the plasma. The generated strong plasma will scatter the incident laser beam and thus trigger defocusing. The competition between the self-focusing and defocusing will finally reach a balance (Sprangle et al., 2002), creating the filamentation phenomenon (Talebpour et al., 1999; Zheng et al., 2007).

It has been revealed (Ageev et al., 1983; Turcu et al., 1997; Gamal et al., 1999; Phuoc, 2000) that with the presence of a target, the critical power of air breakdown near the target surface could be significantly reduced, due to the enhancement of the II process by the ejected electrons from the target surface. For example, Mao et al. (2000) and Hile (1996) revealed that the critical power is lowered from 10^{14} W/cm^2 to 10^{12} W/cm^2 for a ps laser. In this study, the laser power is sufficient to cause the air breakdown near the focal region, where a target surface is present. The consequent defocusing effect will balance

the self-focusing process, making it not necessary to calculate the self-focusing effect by a 2D model. Therefore, the 1D BP method adopted in this model is sufficient to capture the laser propagation in air under the study conditions.

For air breakdown process, TI, MPI, IB, and II are considered, as described in Section 3.1.1.1. The interaction between atoms and ions is calculated by the MD method, while the Coulomb interaction is simulated using the PIC/MC method, which will be described in the following sections.

4.2 Atomic Dynamics

The atomic dynamics was described by the standard MD method, similar to the method in Hu et al. (2011b). However, instead of the Morse potential for metals as in Hu et al. (2011b), the atomic interaction of silicon was described by the tree-body Stillinger-Weber potential (Stillinger and Weber, 1985), which exhibits good accuracy in predicting elastic (Noya et al., 1996; Cowley, 1988), vibrational (Noya et al., 1996; Broughton and Li, 1987), triple-point (Broughton and Li, 1987; Abraham and Broughton, 1986), and liquid (Stillinger, 1985; Balamane, 1992) properties. For laser ablation, Stillinger-Weber potential has been verified for its validity through comparisons of ablation depth with experimental values (Lorazo et al., 2006; Vasileska and Goodnick, 2006). The initialization of atom positions was created by a lattice dynamics code GULP (Gale and Rohl, 2003). The dissipative particle dynamics (DPD) method (Besold et al., 2000) was then applied to equilibrate the atom system at 300 K. To check the equilibrium stability, the program was run for 1 ns without external force.

The DPD equations of motion are described as (Hu et al., 2011b):

$$\dot{r}_i = \frac{p_i}{M}$$
$$\dot{p}_i = F_i + F_i^D + F_i^R \tag{4.2}$$
$$F_i = -\nabla_{r_i} V$$
$$F_i^D = \sum_{j \neq i} (-\gamma w^D(r)(\hat{r}_{ij} \cdot v_{ij})\hat{r}_{ij})$$
$$F_i^R = \sum_{j \neq i} \sigma_N w^R(r) \zeta \hat{r}_{ij},$$

where $\boldsymbol{r}_i$, $\boldsymbol{p}_i$, and M are the position vector, momentum vector, and mass of the atom i, respectively. $\boldsymbol{v}_{ij}$ (= $\boldsymbol{v}_i - \boldsymbol{v}_j$) is the relative velocity between particles i and j, while $\hat{\mathbf{r}}_{ij}$ denotes the unit vector of the interatomic axis $\boldsymbol{r}_{ij} = \boldsymbol{r}_i - \boldsymbol{r}_j$. The force term $\boldsymbol{F}_i$ is obtained from the intermolecular potential V. γ and σ_N are the friction constant and the noise strength, respectively. w^D and w^R are r-dependent weight functions vanishing for $r > r_c$. ζ is a Gaussian white noise variable with zero mean and unit variance.

$\boldsymbol{F}_i^D$ represents the additional dissipative force on particle i, and $\boldsymbol{F}_i^R$ denotes the corresponding random force. The following relations are required by the fluctuation dissipation theorem:

$$\sigma_N{}^2 = 2k_B T\gamma \tag{4.3}$$
$$[w^R(r)]^2 = w^D(r)$$

After reaching initial temperature equilibrium, non-equilibrium molecular dynamics ensembles are adopted to simulate the atom dynamics and the energy exchange with electrons. The equation of motion for atom i is calculated by (Schäfer et al., 2002):

$$M\frac{d^2\mathbf{r}_i}{dt^2} = -\nabla_{\mathbf{r}_i} V - \frac{g}{C_l}\frac{T_l - T_e}{T_l} M\mathbf{v}_i^*, \tag{4.4}$$

where $-\nabla_{\mathbf{r}_i} V$ is the force origin from the intermolecular potential, g is the electron-phonon coupling term, C_l is the lattice specific heat, T_e and T_l are the electron temperature and lattice temperature, respectively. The simulation domain is divided into layers of thickness equal to the cut-off radius, in which the macroscopic properties, such as T_e and T_l, are calculated. Electron-phonon coupling is calculated within these layers, which is proportional to the temperature difference T_e - T_l. In the coupling term, the thermal velocity $\mathbf{v}_i^* \equiv \mathbf{v}_i - \mathbf{v}_c$ is calculated as difference between the actual velocity and the center of mass velocity. This equation of motion satisfies the momentum conservation, as proved by Hu et al. (2010). The Verlet velocity scheme (Frenkel and Smit, 2002) is used to solve the equation of motion, and the time step Δt of even 5 fs has been shown to be adequate through a time step sensitivity analysis (Hu et al., 2010).

For the boundary conditions of simulation domain, a free boundary is set at the top, lateral directions are set to be periodic, and the nonreflecting boundary condition is applied at the bottom (Hu et al., 2010a).

4.3 Carrier Dynamics in Target

In the target area, the carrier dynamics, including photon absorption by carriers and scattering processes, are calculated by the MC method. During USLP ablation, very high carrier temperature can be achieved (several electron volt (eV)), and thus the Maxwell-Boltzmann distribution can be adopted as an approximation of the energy distribution of carriers. The validation of the MC method with Maxwell-Boltzmann distribution has been proved by previous studies in the calculation of carrier transportation in semiconductors (Lorazo et al., 2006; Vasileska and Goodnick, 2006) and plasma particle dynamics (Hu et al., 2011b; Nanbu 2000). In this study, similar to the model developed by Hu et al. (2011b), the electrons in the valence band are treated as the Drude classical electron gas with the Maxwell-Boltzmann energy distribution at equilibrium. Each electron in the system is randomly assigned a position, velocity, and kinetic energy, and then the equilibrium distribution of the system is achieved by the Metropolis method (Frenkel and Smit, 2002).

Different from the model for copper developed by Hu et al. (2011b), more absorption mechanisms and electron-hole dynamics need to be considered. To calculate the laser absorption by electrons, the simulation domain was divided into layers with a thickness less than 1 nm. Each electron in the same layer has the same probability to absorb the photon energy. The dominating absorption mechanisms considered in this model include free carrier intraband absorption (inverse Bremsstrahlung) and single-/two-photon interband absorption, as described in Section 3.2.1. The former is important in liquid state and after strong electronic excitation in solid state, and the latter dominates in the cold solid state before electronic excitation. The occurrence possibilities of different absorption mechanisms were calculated by the relative ratio of their absorption coefficient. For metals, only free carrier absorption was considered in Hu et al. (2011b). In this model, upon interband absorption, an electron-hole pair was generated with the total kinetic energy of $\hbar\omega - E_g$ and the effective mass of $0.75\, m_e$ (Lorazo et al., 2006), where $\hbar\omega$ is the photon energy, E_g is the band gap, and m_e is the free electron mass. For metals, the interband excitation was ignored due to the large amount of free electrons.

The scattering processes are simulated by the similar scheme described by Hu et al. (2011b), and the total scattering rate can be written as (Lorazo et al., 2006; Vasileska and Goodnick, 2006):

$$\Gamma_0 = 1/\tau_0 \geq \Gamma_{real}(\varepsilon_{ei}) + \Gamma_{self}(\varepsilon_{ei}) = \Sigma\Gamma_j(\varepsilon_{ei}) = \Sigma 1/\tau_j(\varepsilon_{ei}) \quad (4.5)$$

The total scattering rate Γ_0 is the summation of all the possible scattering mechanisms $\Gamma_j(\varepsilon_{ei})$, including electron-electron scattering, electron-phonon scattering and II. $\Gamma_{real}(\varepsilon_{ei})$ is the real instantaneous collisional rate, and $\Gamma_{self}(\varepsilon_{ei})$ is the self-scattering rate, which is induced to make the total scattering rate constant without changing the momentum and trajectory after the scattering (Vasileska and Goodnick, 2006). The total relaxation time τ_0 determines the simulation time step of the MC method. For each electron, the collision mechanism is determined by the collision probability τ_0/τ_j.

The energy exchange during the collision process needs to be simulated for electron-electron scattering, electron-phonon scattering and II, respectively. For electron-electron scattering, the energy changes for the two involved electrons are calculated by a simplified scheme as: (Weng and Kushner, 1990; Tas et al., 1997):

$$\begin{aligned} &\Delta\varepsilon_1 = -\varepsilon_1\zeta,\ \Delta\varepsilon_2 = +\varepsilon_1\zeta, \text{ if } \varepsilon_1 \geq \varepsilon_2; \\ &\Delta\varepsilon_1 = +\varepsilon_2\zeta,\ \Delta\varepsilon_2 = -\varepsilon_2\zeta, \text{ if } \varepsilon_1 < \varepsilon_2, \end{aligned} \tag{4.6}$$

where ζ is a random number between 0 and 1, and $\varepsilon_1/\varepsilon_2$ are the original kinetic energies of the two electrons, respectively. The total energy is conserved for each collision event, and the electron momentum conservation is also satisfied for the whole electron system, although it is not necessarily satisfied for each collision.

The energy exchange term for electron-phonon scattering is calculated by the electron-lattice coupling term in Eq. (4.4) by MD calculation. It was proposed as a virtual phonon exchange process (MacDonald, 1980; Ivanenko and Mitsen, 1997). In each simulation spot, the calculated energy exchange is transferred between the electron system and the lattice.

The energy exchange during II process is described as (Tas et al., 1997):

$$\Delta\varepsilon_{imp} = -\varepsilon^{ion} - (\varepsilon_{imp} - \varepsilon^{ion})\zeta,\ \Delta\varepsilon_{new} = +(\varepsilon_{imp} - \varepsilon^{ion})\zeta, \tag{4.7}$$

where $\Delta\varepsilon_{imp}$ is the energy change of the impact energy, ε_{imp} is its original energy, ε^{ion} is the ionization energy, and $\Delta\varepsilon_{new}$ is the total kinetic energy of the generated electron. The reverse process describes the recombination process.

4.4 Carrier Dynamics in Plasma

During USLP ablation, a strong hot plasma can be generated by strong surface electron/ion ejection. The Coulomb interaction is the dominating interaction mechanism among charged particles, and can significantly affect the plasma dynamics. Typically,

MC method can effectively calculate the Coulomb interaction in the short-range (Birdsall, 1991; Birdsall and Langdon, 2005). However, since the Coulomb interaction is a long-range interaction, the MC method is too computationally expensive to capture the long-range interaction. Therefore, the particle-in-cell (PIC) method is adopted to capture the long-range Coulomb interaction in the plasma. This PIC/MC method is then coupled with MD method in the plasma region to consider the interaction between charged particles and neutral atoms. The PIC code in this study was obtained from the model developed by Hu et al. (2011b), which was modified from the standard PIC/MC simulation technique (Serikov et al., 1999; Birdsall, 1991; Birdsall and Langdon, 2005) for the simulation of ultrashort laser pulse induced plasma. In the explicit PIC model, the spatial grid size should follow $\Delta x < \lambda_D$ (λ_D is the Debye length), because the long-range interaction is only effective outside the Debye cube. In this study, the grid size of 1 nm was adopted according to the sensitivity test. The time step Δt was chosen to be 1 fs, which satisfies the restriction that $\Delta t < \omega_p^{-1}$ (ω_p is the electron plasma frequency) due to the effect of electron plasma oscillation. A 1D PIC model was applied in this study, which is valid because in the early-stage, the plasma expands mainly along the laser propagation direction at normal incidence (Mao et al., 2000). However, in the direction perpendicular to laser propagation direction, the whole simulation domain is comprised by 2D layered planar sheets. This 1D PIC simulation only captures the velocity variations of the charged particles along the laser irradiation direction. The velocity changes in the perpendicular direction are calculated by the MD/MC method. The simulation domain dimension in the horizontal dimension is about 8 nm × 8 nm, and periodic boundary conditions are applied to MD and MC methods so that the overall dimensionality of MD/MC simulation is still one. At the two ends of the simulation domain, the electric field is considered to be 0.

4.5 Metallic Transition in Liquid State

It has been revealed that the group IV and III–V semiconductors have a metallic transition in the liquid state (Li and Fauchet, 1987). When the silicon temperature is

above melting temperature (1683 K), the electron number density is set to jump to about 2×10^{23} cm^{-3} (Lorazo et al., 2006). In this model, the electrons in valence band were locally promoted into the conduction band at the melting point. In solid state, the atomic interaction was described by the tree-body Stillinger-Weber potential (Stillinger et al., 1985), while the embedded atom method (EAM) potential (Zhakhovskii et al., 2009) was adopted to describe the inter-atomic interaction for metallic liquid silicon.

4.6 Simulation Domain Setup

Figure 4.2 shows the simulation domain size information. The total simulation domain is 2 mm in the laser propagation direction, including a MD simulation domain containing a $10\times10\times400$ nm^3 area for silicon, and a $10\times10\times600$ nm^3 area for the air above. The periodic boundary conditions are applied in the transverse direction. It is assumed that the free electrons and the neutral Si atoms will not go beyond the total simulation domain and the MD simulation domain, respectively, in the longitudinal direction within the first 100 ps. This assumption has been verified. It is also assumed that the motion of neutral air atoms in air II subdomain can be neglected within 100 ps, because its low density will not affect the plasma dynamics a lot. During this time, the interface between the target plume and the background air is still in the MD range. The motion of Si lattice in Si II subdomain can be neglected because of the non-reflecting boundary condition applied at the bottom of Si I subdomain. The laser pulse propagation in the region above the target surface is simulated using the 1D BPM method, while considering the effect of the laser power density change due to the external focusing lens. The generation and dynamics of charged particles (free electrons and ions), originated from the target and air, are simulated using the PIC-MC method. The evolution of neutral atoms and the scattering processes between neutral atoms and charged particles are simulated using the MD-MC method.

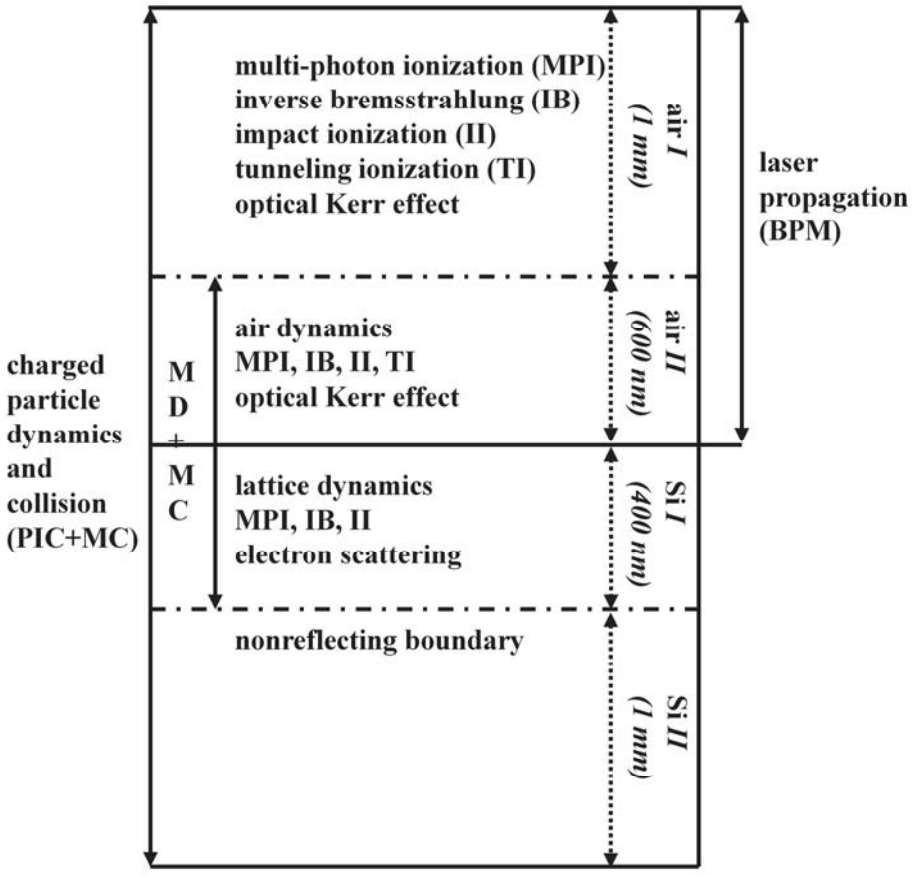

Figure 4.1. Schematics of the simulation method and domain, with Si as the target.

5. USLP ABLATION OF METALS AND SEMICONDUCTORS: NUMERICAL AND EXPERIMENTAL INVESTIGATION OF EARLY PLASMA DYNAMICS AND ITS ROLE IN ABLATION PROCESS

In this chapter, the ablation of metals and semiconductors by a femtosecond laser pulse at different intensity is investigated by using the HD models developed in Chapter 3. The experimental measurements for plasma expansion are carried out to validate the simulation results, using a shadowgraph technique for early plasma and direct fluorescence measurement for plume plasma. For ablation of metals, the evolutions of both the early plasma and plume plasma are investigated in a time scale from several femtoseconds to 50ns, focusing on their spatial profiles and expansion velocities. The effects of surface electron emission and early plasma generation are also studied with the proposed model. The electron emission rates of different mechanisms are obtained at different laser intensities. The maximum surface electron temperatures without considering electron emission are calculated and compared with the results involving all mechanisms to investigate the importance of the early plasma during the ultrashort laser–metal interaction. Considering the early plasma absorption and the switching of the dominant absorption mechanisms, ablation rates at high laser intensity are predicted by the model. For ablation of semiconductors, the ablation in the high laser intensity range and the effect by early plasma absorption are studied. The early plasma evolution dynamics are investigated by the model and the experimental measurement. In addition, the ion ejection mechanisms are investigated by the model at the early stage of ablation process and the occurrence of CE in semiconductor is proposed.

5.1 USLP Ablation of Metals

USLP ablation of metals has been investigated for many years, while a better understanding of its underlying physics is still required, due to its involved complicated multiphysical phenomena. The ablation process (ablation rate and quality) could be affected by many factors, and varies with different laser intensity, wavelength, pulse duration, material properties, etc. Experimental investigations (Nolte et al., 1997, Furusawa et al., 1999, Afanasiev et al., 2002a) have indicated that the electron thermal diffusion can play an important role in the dissipation of absorbed photonic energy. Because of different heat dissipation mechanisms, USLP ablation of metals has been categorized by two different regimes at low ($<5\times10^{12}$W/cm^2 for copper) and moderate ($5\times10^{12} - 1\times10^{14}$W/cm^2 for copper) laser intensity. As an example, the experimental measurement data for copper are shown in Figure 4.1 (Nolte et al., 1997). The dependence of the ablation rate could be expressed by two different logarithmic functions (Nolte et al., 1997; Afanasiev et al., 2002a):

$$L = \delta \ln\left(\frac{I}{I_{th}{}^{M}}\right) \qquad (4.1)$$

$$L = l \ln\left(\frac{I}{I_{th}{}^{H}}\right),$$

where δ is the optical penetration depth, l is the electronic heat penetration depth, and $I_{th}{}^{M}$, $I_{th}{}^{H}$ are the thresholds of ablation for the low and moderate laser intensity range, respectively. In the case of low-intensity ablation, the number density of hot electrons is so low that energy transfer occurs only within the area characterized by the skin depth. However, in the case of moderate laser intensity, the density of hot electrons is high enough, and the contribution of the electron thermal diffusion to the dissipation of the absorbed energy causes a sudden increase in the ablation depth per pulse.

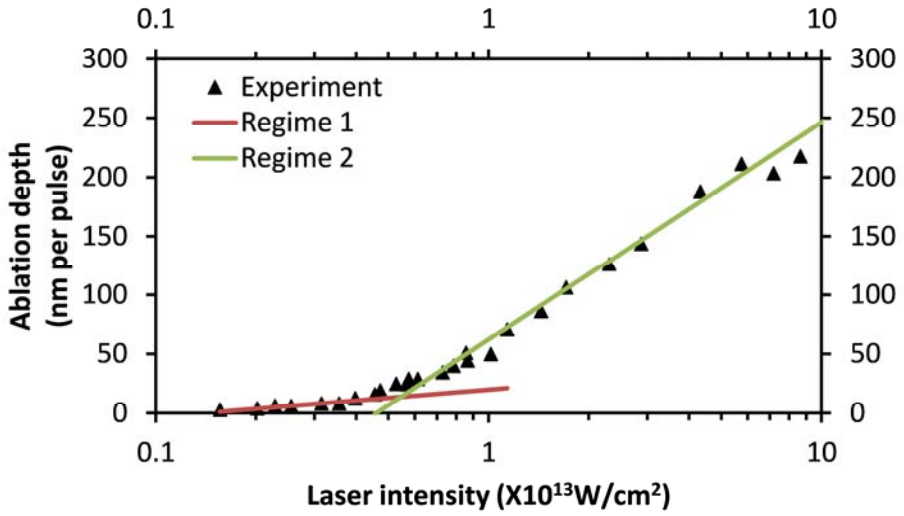

Figure 5.1. Ablation depth per pulse for copper versus the incident laser fluence. Pulse duration: 150 fs, wavelength: 780 nm, target material: copper (Nolte et al., 1997).

Some experimental measurements (Komashko et al., 1999; Vidal et al., 2001; Nedialkov et al., 2004a; Atanasov and Nedialkov, 2007) show that at high laser intensity ($>1\times10^{14}$W/cm^2) in vacuum, there is a steep increase of the ablation depth per pulse with respect to the laser intensity, while the ablation depth in air grows much slower. This phenomenon indicates that new mechanisms are involved, and a further investigation is necessary for a better understanding of the relevant physics in this regime. Besides, as discussed in Section 1.4.1, the early plasma absorption of incident laser pulse energy is not negligible at the intensity above 1.39×10^{12} W/cm^2. Its density, generation time, spatial profile, and expansion dynamics can all significantly affect the ablation process. Therefore, in this study, the early plasma dynamics during femtosecond laser ablation of metals are investigated. After that, the ablation process in the high laser intensity range is studied, considering all possible dominating absorption mechanisms and the early plasma absorption of incident laser pulse energy.

5.1.1 Validation of the HD Model

To investigate the evolution of the early stage plasma, its very early stage (before 300 fs) expansion is calculated and compared with the experimental data in Geindre et al. (1994) as shown in Figure 4.2. The target is Al, the laser pulse duration is 77fs, the wavelength is 620nm, and the laser intensity is 3×10^{15}W/cm^2. The plasma front is determined by the front of the electrons out of the target. Under the irradiation of the Gaussian beam, the electrons near the beam center will gain more laser energy and first become energetic enough to be ejected out of the target surface. Therefore, the early plasma initiates from the beam center and grows gradually in radial direction at the beginning. Besides, the spatial profile of the early plasma is similar to the Gaussian distribution of the laser pulse. After 166 fs, the expansion in radial direction becomes negligible compared with that in longitudinal direction, because the whole irradiated area has reached high enough temperature for surface electron emission, and the ejected electrons have higher velocities in longitudinal direction than in radial direction. The expansion of early plasma can thus be considered to be one-dimensional in this stage.

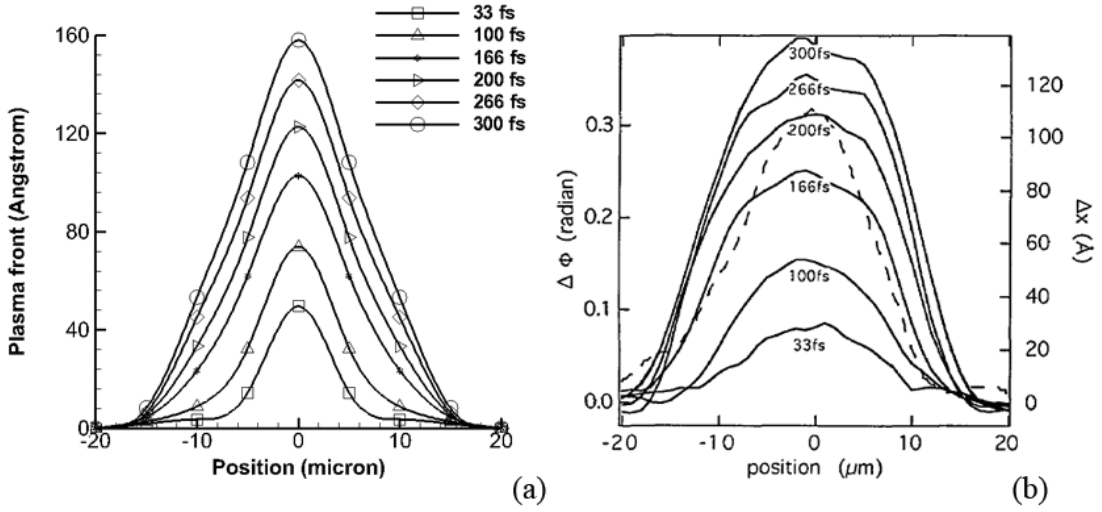

Figure 5.2. Early stage plasma front shape development. Target material: Al, the laser pulse duration: 77fs; the wavelength: 620nm; and the laser intensity: 3×10^{15}W/cm^2. (a) Simulation results. (b) Experimental results in Geindre et al. (1994).

5.1.2 Early Stage Plasma Dynamics

The evolution of the early plasma up to hundreds of picoseconds was measured by shadowgraph measurement using the set-up described in Chapter 2. The target material is copper. The laser pulse has the duration of 100fs, the wavelength of 800nm, and the laser fluence of 21 J/cm^2. The laser focal spot was set slightly above the target surface, the distance of which was equal to the Rayleigh length of the laser beam. The results in Figure 4.3 reveal that plasma forms in several portions during its expansion. The portion A is mainly generated by laser induced air breakdown near the focal point, the location of which does no move during the whole process. It is initiated almost simultaneously with the laser irradiation and lasts for about 150 ps. The portion B is formed almost concurrently with the portion A, grows fast and disappears at about 150 ps. From about 28 ps, the growth of the third portion is noticeable, of which the expansion speed is much slower than the portion B. The simulation results of plasma front expansion in both longitudinal and radial directions are shown in Figure 4.4, in comparison with the experimental results. The simulation only considers the plasma generated by copper electron emission and avalanche ionization of the air, and neglects the portion A because it does not have spatial evolution. Figure 4.5 shows the plasma front expansion velocities at different delay times. Before 150 ps, the plasma front is determined by the front of portion B and grows very fast (as high as 1.5×10^6m/s) at the beginning. After that, portion B disappears and the plasma front determined by the front of portion C that is far behind starts a second expansion. The expanding velocity drops to about 3.5×10^4m/s. Both portion B and portion C are believed to be caused by the electron emission from the target surface and the avalanche ionization of the air (Hu et al., 2011a). However, portion B consists of the electrons with high kinetic energies, which can be generated simultaneously with the laser irradiation by photoelectric emission and air breakdown. These electrons will expand fast due to their high kinetic energies, disperse into the ambient gas quickly and finally disappear in a very short amount of time. The thermal electron emission is delayed compared with photoelectron emission because of the thermal relaxation process. The emitted electrons with low energies will expand and disperse slowly, forming the portion C. The expansion speed is close to that in

longitudinal direction, which is the reason why the plasma can maintain its spherical shape during expansion in this time scale.

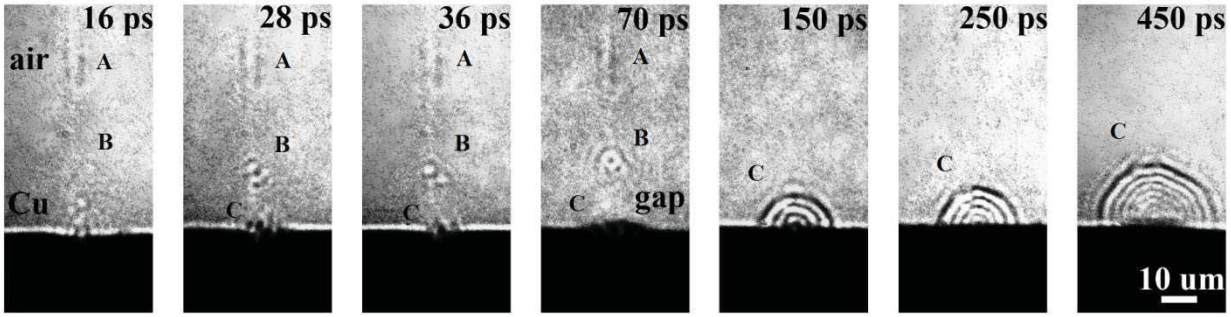

Figure 5.3. Images of early plasma by shadowgraph measurement. Target material: copper; the laser pulse duration: 100fs; the wavelength: 800nm; and the laser fluence: 21J/cm^2.

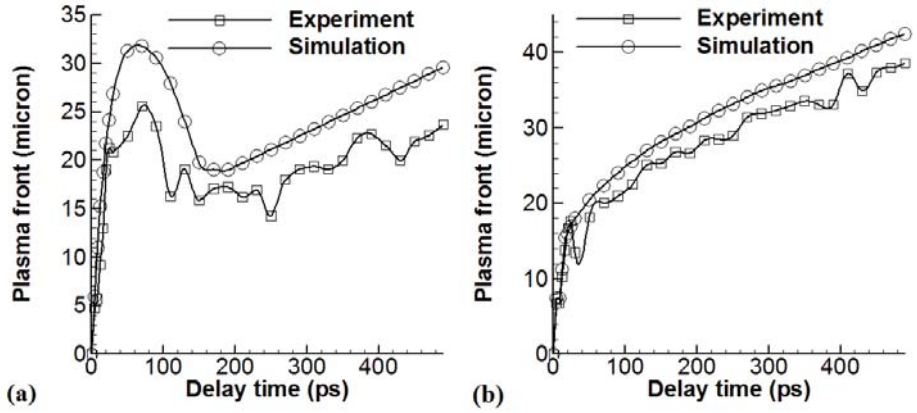

Figure 5.4. Plasma expansion for focal point above the target surface. Target material: copper; the laser pulse duration: 100fs; the wavelength: 800nm; and the laser fluence: 21J/cm^2. (a) Longitudinal direction, (b) radial direction.

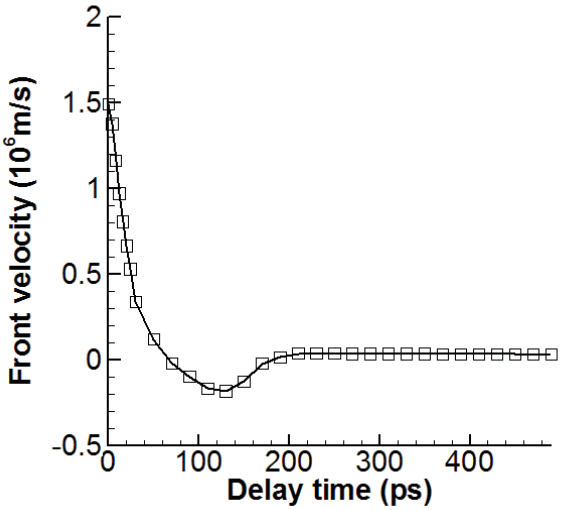

Figure 5.5. Plasma front expansion velocity in longitudinal direction. Target material: copper; the laser pulse duration: 100fs; the wavelength: 800nm; and the laser fluence: 21J/cm^2.

To analyze the components inside the early plasma, the electron, material ion density and ambient gas ion distribution are calculated, as shown in Figure 4.6, Figure 4.7 and Figure 4.8, respectively. Both the material ions ejection and ambient gas ionization have already started after several picoseconds. However, the ejected material ions number density is much lower than that of the ambient gas ions. Besides, Figure 4.9 shows that the front of copper ions is far behind the front of the electrons generated by surface electron emission and air ionization, and the expansion speed is much slower (~10^3m/s). Therefore, the early stage plasma is mainly caused by the electron emission and the air breakdown.

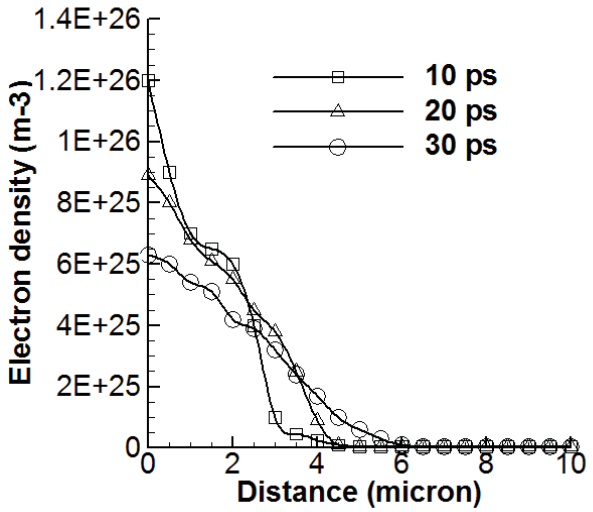

Figure 5.6. Electron density distribution in plasma. Target material: copper; the laser pulse duration: 100fs; the wavelength: 800nm; and the laser fluence: 21J/cm^2.

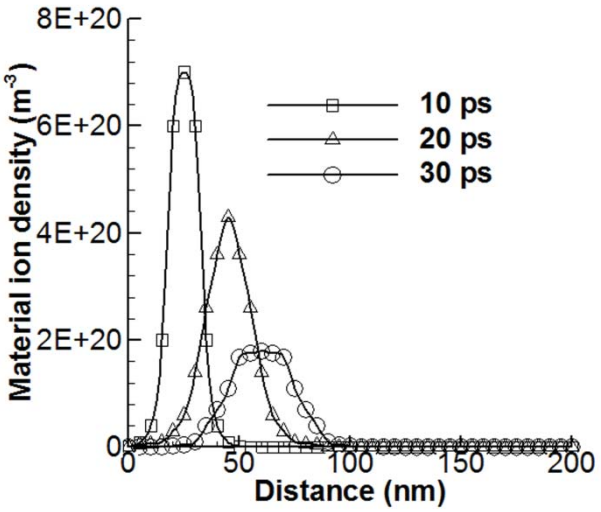

Figure 5.7. Density distribution of ions from the target material in plasma. Target material: copper; the laser pulse duration: 100fs; the wavelength: 800nm; and the laser fluence: 21J/cm^2.

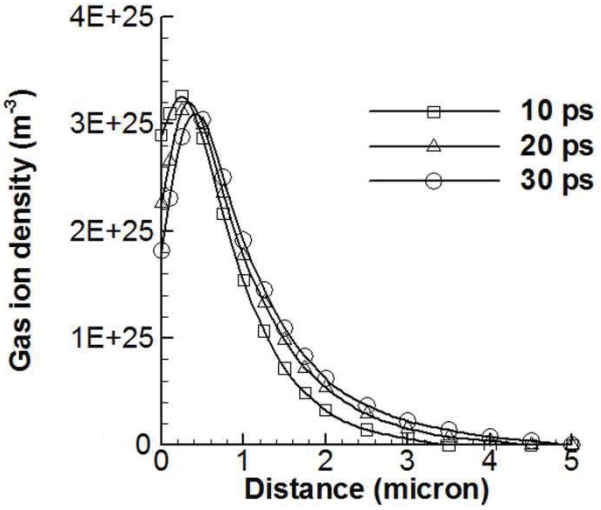

Figure 5.8. Density distribution of ions from the air in plasma. Target material: copper; the laser pulse duration: 100fs; the wavelength: 800nm; and the laser fluence: 21J/cm^2.

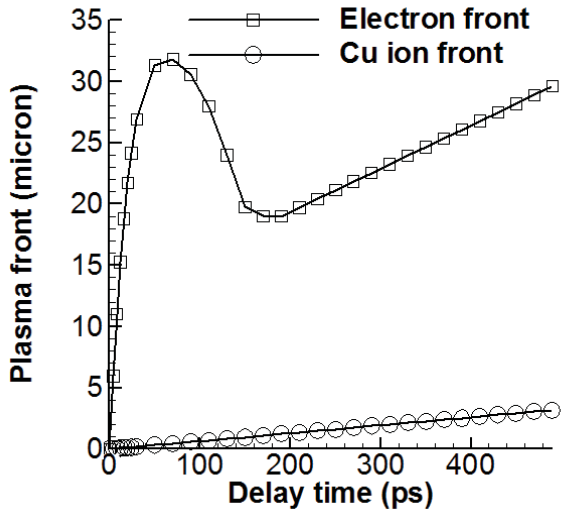

Figure 5.9. Plasma front position of early plasma and plume plasma. Target material: copper; the laser pulse duration: 100fs; the wavelength: 800nm; and the laser fluence: 21J/cm^2.

For further analysis, the early plasma generation and expansion under the same laser irradiation in vacuum are studied by the model. If the early plasma properties are similar

in vacuum and in air, the early plasma should mainly come from the target material; otherwise, it can be deduced that the early plasma is caused by the electron emission and the ambient gas ionization. The results in Figure 4.10 reveal that there is an early plasma generated in vacuum at the first 100 fs, while the plasma front location is much lower and expansion speed is much slower than those of plasma in air. The early plasma in vacuum comes from the electron emission from the target surface, but it will disappear soon because there is no ambient gas ionization to generate more electrons. However, the early plasma in air can be formed and enhanced by air breakdown and keep growing for more than 500 ps. Therefore, it can be proved that the early plasma is mainly caused by the electron emission and the air breakdown, rather than target material ejection.

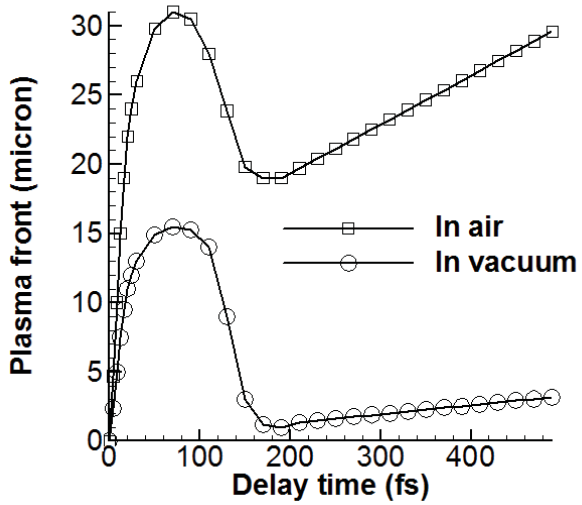

Figure 5.10. Early plasma expansion in air and in vacuum. Target material: copper; the laser pulse duration: 100fs; the wavelength: 800nm; and the laser fluence: 21J/cm^2.

5.1.3 Plume Plasma Dynamics

The copper plume plasma evolution from 1 ns to 50 ns are measured by fluorescence measurement, as shown in Figure 4.11. The laser fluence is 21J/cm^2. Different colors represent different fluorescence intensities, determined by local electron densities and temperatures. The corresponding simulation results are shown in Fig. 4.12, compared

with the measurements. In such a long time scale, there is no early stage plasma anymore and only plume plasma exists, the front of which is determined by the front of ejected ions and neutral atoms from the target, where the ion density is higher than the air density. Fig. 4.13 shows the expansion velocity of the plume plasma (~10^3m/s), which is much slower than that of the early stage plasma (10^4~10^6m/s) and decreases with time. After 50 ns, the plume plasma tends to stop expanding and will finally disappear by diffusing into the surrounding.

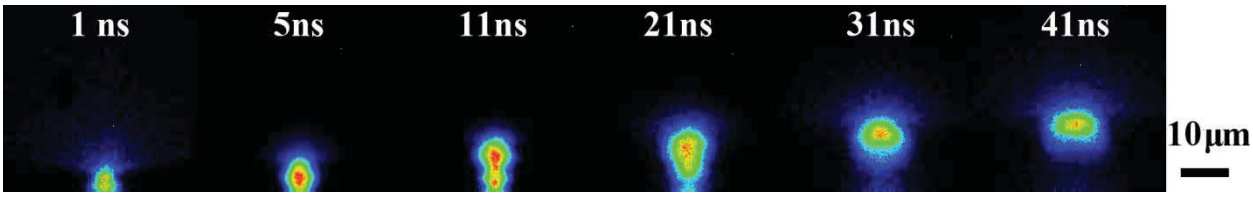

Figure 5.11. Images of plume plasma by fluorescence measurement. Target material: copper; the laser pulse duration: 100fs; the wavelength: 800nm; and the laser fluence: 21J/cm^2.

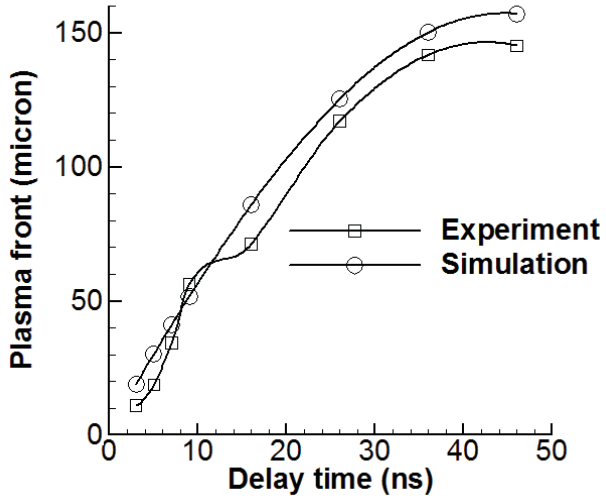

Figure 5.12. Plume plasma front expansion. Target material: copper; the laser pulse duration: 100fs; the wavelength: 800nm; and the laser fluence: 21J/cm^2.

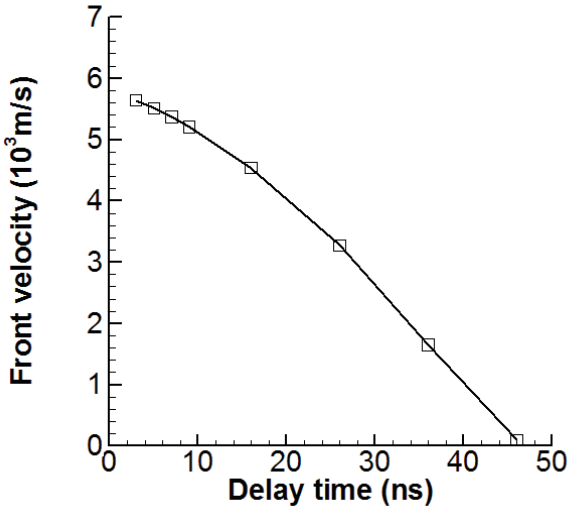

Figure 5.13. Plume plasma expansion velocity. Target material: copper; the laser pulse duration: 100fs; the wavelength: 800nm; and the laser fluence: 21J/cm^2.

5.1.4 Effect of Hot Electron Emission

As one of the key processes for investigating the physics of early stage plasma generation, hot electron emission includes two important emission mechanisms: thermal emission and photoelectric emission. The emission rates of both will increase with temperature. Besides, the photoelectric emission rate will increase with laser intensity. To study the roles of these two mechanisms under different conditions, the electron emission rates for both of them, together with the total emission rates, are calculated at different laser intensities with copper as the target. The calculation results are shown in Fig. 4.14 (a), (b) and (c) for laser pulse width of 100 fs and laser intensity of $5 \times 10^{11} W/cm^2$, and $5 \times 10^{12} W/cm^2$, and $5 \times 10^{13} W/cm^2$, respectively. For $I = 5 \times 10^{11} W/cm^2$, photoelectric emission is dominant at the beginning, because electron temperature is not high enough and thermal emission can be neglected. Starting from around 150 fs, the thermal emission rate increases rapidly together with the surface electron temperature, while the photoelectric emission rate is decreasing because of the drop of the laser intensity. Therefore, the thermal emission rate gradually exceeds the photoelectric emission rate and becomes the dominant mechanism. After 200 fs, only the thermal emission exists

since the laser pulse has ended. During the whole process, the peak of the thermal emission rate is much higher than that of photoelectric emission rate. For $I = 5 \times 10^{12} W/cm^2$, and $I = 5 \times 10^{13} W/cm^2$, the photoelectric emission rate is much higher than the thermal emission rate during laser irradiation, making thermal emission negligible during this stage. After the end of laser pulse, only thermal emission exists, while its emission rate is much lower than the photoelectric emission rate during laser irradiation, and will decrease with time because of the drop of electron temperature. It can be concluded from the simulation results that at low laser intensities ($< 10^{11} W/cm^2$), the thermal emission is the dominant emission mechanism, while the photoelectric emission is more important at high laser intensities ($> 10^{11} W/cm^2$). The hot electron emission is only important for the first several hundreds of femtoseconds, after which it can be neglected.

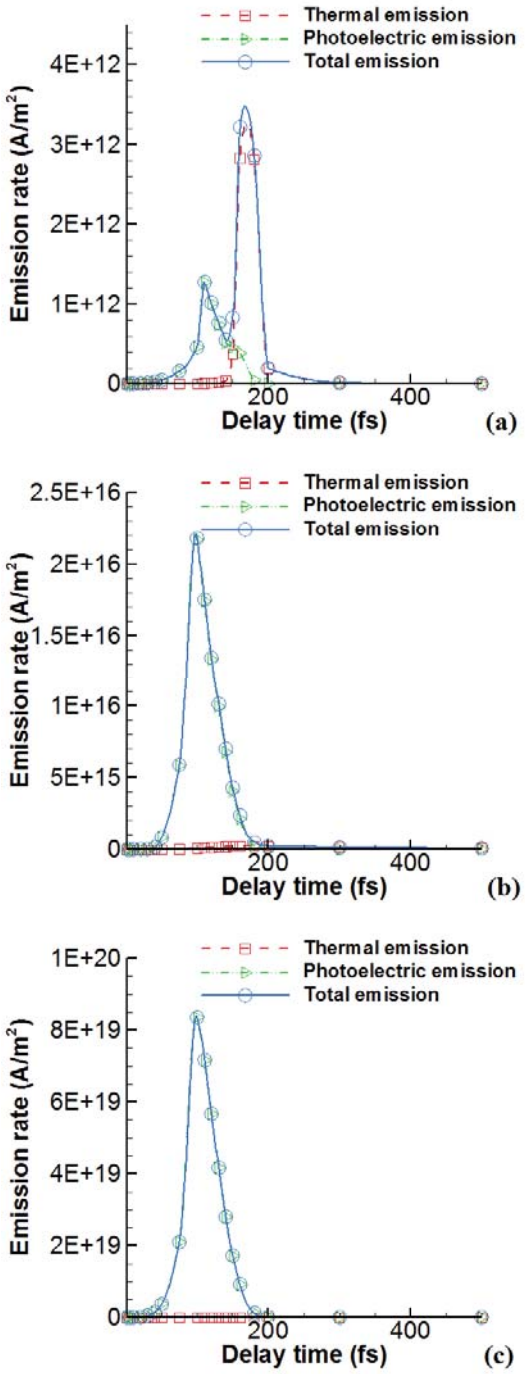

Figure 5.14. Hot electron emission rate at different laser intensities. Target material: copper; the laser pulse duration: 100fs; the wavelength: 800nm; the laser intensity: (a) $I = 5\times10^{11} W/cm^2$, (b) $I = 5\times10^{12} W/cm^2$, (c) $I = 5\times10^{13} W/cm^2$.

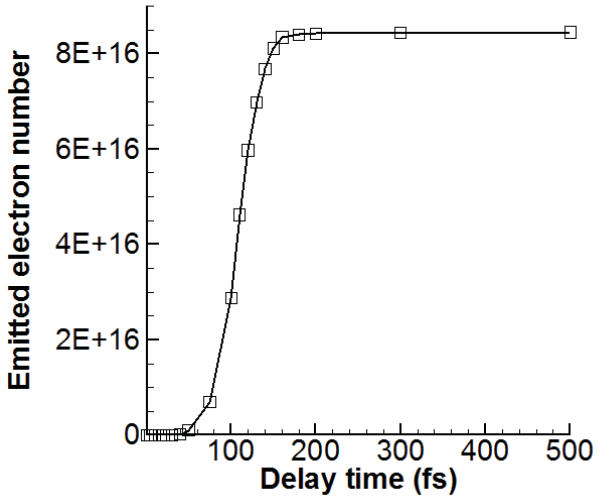

Figure 5.15. Total escaped electron number. Target material: copper, Laser intensity: $I = 5\times10^{12} W / cm^2$.

Fig. 4.15 shows the total emitted electron number during the laser ablation with laser intensity of $I = 5 \times 10^{12} W/cm^2$. The total emitted electron is as many as $8.7\times10^{16}/m^2$, while he total number of conduction electrons in an area of $1m^2$ with several nanometers deep is about 10^{18}. Therefore, the total emitted electrons are significant compared with the electrons inside the target. To further check the importance of hot electron emission and early stage plasma generation for the ultrashort laser-metal interaction, the maximum electron temperatures on the target surface are calculated at different laser intensities without considering the electron emission mechanism and the resultant early plasma, compared with the results involving all the physics. The results are shown in Fig. 4.16. At low intensities range ($I < 5 \times 10^{12} W/cm^2$,), there is no significant difference in the electron temperatures obtained for the two cases. However, when the laser intensity further increases, the electron temperature is overestimated without a consideration of electron emission and early plasma, and the error increases with the laser intensity. At $I = 5 \times 10^{13} W/cm^2$, the electron temperature can be overestimated by as high as 70%. Two main reasons exist for this phenomenon. First, hot electrons will bring their thermal and kinetic energy out of the target when they are ejected out of the target surface. Therefore, the total energy of the electron system inside the target is reduced significantly. Second, the

early stage plasma formed above the target surface can absorb the incident laser energy, and therefore reduces the energy deposited into the metal target. The analysis result reveals that the hot electron emission and early stage plasma are critical to femtosecond laser-metal interaction. The effects of these mechanisms have to be considered to fully understand the physics of ultrashort laser-material interaction.

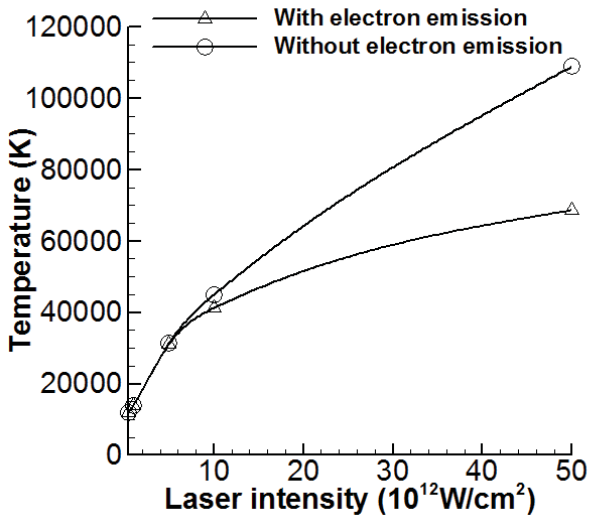

Figure 5.16. Maximum electron temperature on target surface at different laser intensities. Target material: copper; the laser pulse duration: 100fs; the wavelength: 800nm; and the laser intensity: $I = 5\times10^{13} W/cm^2$.

5.1.5 Ablation Rate at High Laser Intensity

Fig. 4.17 shows ablation depth per pulse as a function of laser intensity, for the cases both in air and in vacuum. The pulse duration is 100 fs, and the wavelength is 800 nm, and the target material is aluminum. Experimental data in literatures (in vauum: Nedialkov et al., 2005a, Savolainen et al., 2011; in air: Le Harzic et al., 2005a) are shown to be compared with the simulation results. The detailed parameters used in the simulation and the experiments are summarized in Table 4.1. The pulse duration in Le Harzic et al., 2005a is 120 fs, which is slightly different from the value used in the simulation (100 fs). However, since the ablation depth is not sensitive to the pulse

duration up to 1 ps (Komashko et al., 1999), it is valid to compare these results together. Besides, the focal lens in Savolainen et al., 2011 has a long focal length (25 cm) compared with the others (10 cm). It has been reported that the focal length could affect the absorption of laser beam energy by air breakdown in air (Hu et al., 2011b). However, this becomes the minor effect in vacuum since there is no air breakdown. In the model, the ablation depth is determined by the location where the local temperature exceeds the separation temperature (Vidal et al., 2001). The simulation results show very good agreement with the experimental data. In the low intensity regime ($<10^{13}$W/cm^2), the ablation depths are similar between in air and in vacuum. At moderate intensity (10^{13}W/cm^2 ~ 10^{14}W/cm^2), the ablation depths in vacuum become slightly higher. When the laser intensity further increases, there is a steep increase of the ablation depth in vacuum, and a third ablation regime forms. On the contrary, the ablation depth in air increases slowly with the laser intensity, and tends to saturate as the laser intensity rises to a very high value. The ablation depth in vacuum is 7 times larger than that in air at the laser intensity of 10^{15}W/cm^2.

Table 4.1 Laser and focal lens parameters in the simulation and literatures.

Data	**Pulse duration (fs)**	**Wavelength (nm)**	**Focal length (cm)**
Simulation in this study	100	800	10
Experiment in Nedialkov et al., 2005a (vacuum)	100	800	10
Experiment in Savolainen et al., 2011 (vacuum)	100	800	25
Le Harzic et al., 2005a (in air)	120	800	10

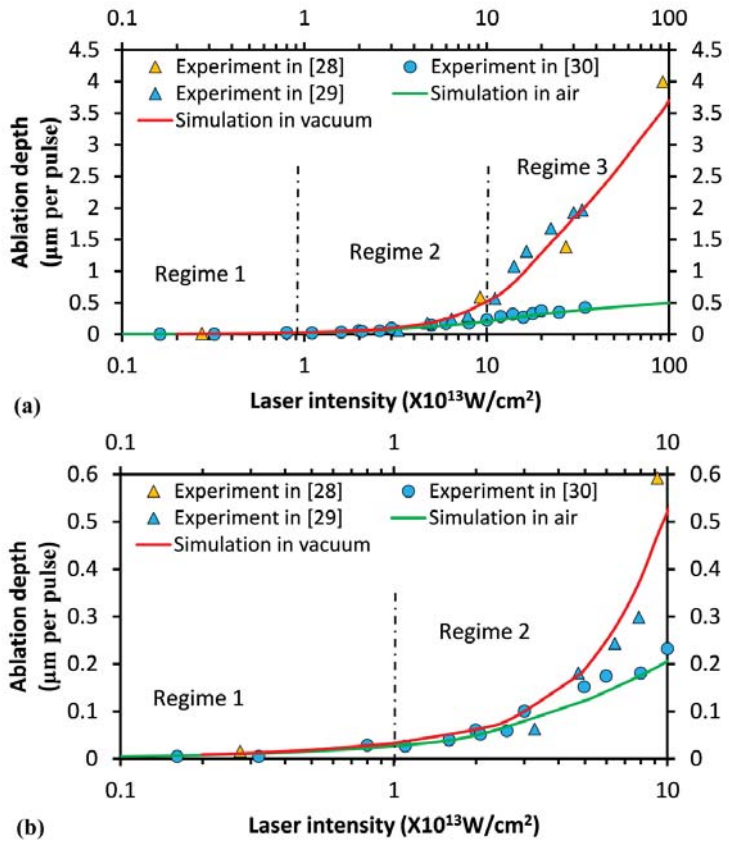

Figure 5.17. Ablation depth per pulse as the function of fluence (a) from low to high laser intensity, and (b) zoom in the low and moderate laser intensity range. Pulse duration of 100 fs, wavelength of 800 nm, target material: aluminum. The experimental data in vacuum is from Nedialkov et al., 2005a, Savolainen et al., 2011, and the data in air is from Le Harzic et al., 2005a.

It has been proved that with increased laser intensity ($> 10^{15}$W/cm^2), the collisions between electrons and ions become less effective, and the collisional absorption model alone fails to explain the level of absorbed laser beam energy experimentally observed by Hansen et al. (1999), Grimes et al.(1999), and Chen et al. (2001). Meanwhile, the collisionless absorption rate increases with laser intensity, and it is possible to become the dominate absorption process in the high intensity regime. Fig. 4.18 reprsents the calculated variation of absorptivity from low to high laser intensity. The absorptivities of the collisional absorption, the collisionless absorption, and the total absorption are compared, and validated by the experimental measurements derived from the reflectivity data in Komarov et al. (2009). The target material is aluminum, the laser pulse duration is

100 fs, and the wavelength is 800 nm. Below moderate laser intensity ($<10^{14}$W/cm^2), the total absorptivity increases with the laser intensity, and is mainly determined by the collisional absorption. The collisionless absorption is negligible in this range. However, as the laser intensity further increases, the collisional absorption rate decreases fast because of the drop of effective collision frequency at high plasma temperature (Edimann et al., 2000). In the mean time, the collisionless absorption rate rises with the increase of the electromagnetic field induced by the laser pulse. It gradually becomes important and dominant in the absorption process. It can be seen that at high laser intensity, the collisional absorption alone significantly underestimates the total absorptivity. At the laser intensity of 10^{15}W/cm^2, the absorptivity is underestimated by 80% by the collisional absorption. This observation agrees with the conclusions in Hansen et al. (1999), Grimes et al.(1999), and Chen et al. (2001) that the collisionless absorption will become the dominant absorption mechanism in the high laser intensity range. By considering the collisionless absorption, the simulation results show a good agreement with the experimental data in a wide range of laser intensity. The switch of the dominant absorption mechanism may have a significant effect on the absorption rate, heat diffusion depth and the ablation depth. Based on the analysis as shown in Fig. 4.18, at high laser intensity, most of the laser beam energy is absorbed by the collisionless absorption, and the total absorptivity increases quickly accordingly. The absorbed laser beam energy can then be dissipated deeper into the target by the electron thermal diffusion, consequently leading to a sudden rise of ablation depth. Therefore, the sudden increase of the ablation depth at high laser intensity can be attributed to the involvement of the collisionless absorption and the resultant deeper penetration depth.

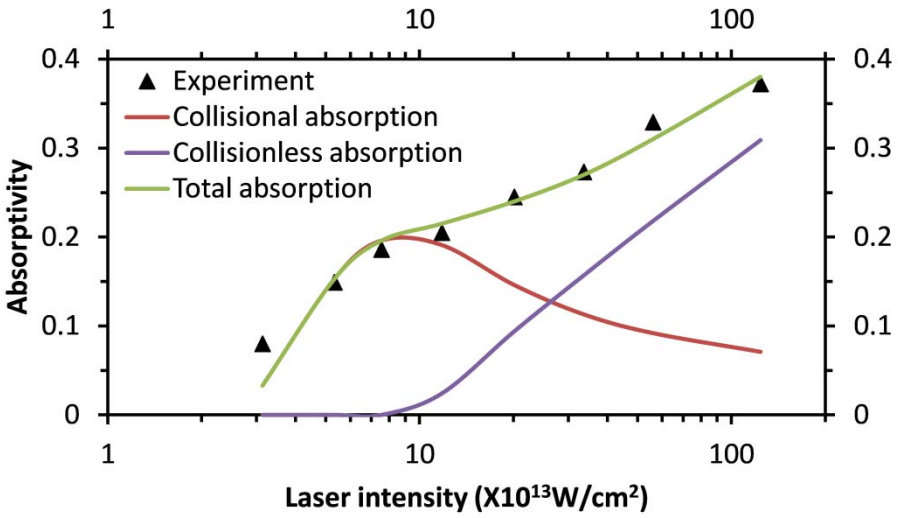

Figure 5.18. Absorptivity of the target at different laser intensity. Pulse duration: 100 fs, wavelength: 800 nm, target material: aluminum. Experimental data is from Komarov et al. (2009).

In the high intensity regime, the ablation depth in air increases slowly with laser intensity, and the ablation rate is much lower than that in vacuum. The dissimilarity between the ablation depth trends in air and in vacuum is attributed to air breakdown and early plasma generation in air. When the laser intensity is high enough, the laser induced air breakdown will occur by MPI. Besides, a strong early plasma will be formed above the target within the pulse duration by surface hot electron emission and the resultant air ionization. This early plasma and air breakdown can both absorb the incident laser beam energy and decrease the energy deposited into the target, thus decreasing the ablation rate significantly. Fig. 4.19 shows the portion of the laser beam energy absorbed by the early plasma and air breakdown as a function of laser intensity. The pulse duration of 100 fs, the wavelength is 800 nm, and the target material is aluminum. The external focal lens has a focal length of 10 cm. It can be seen that the early plasma absorption starts from 10^{14} W/cm^2, while the threshold of air breakdown is around $3X10^{13}$ W/cm^2. Besides, air breakdown is the dominant absorption process, especially in the low laser intensity range. The laser beam energy consumed by air breakdown is over 2 times higher than the loss due to the early plasma absorption.

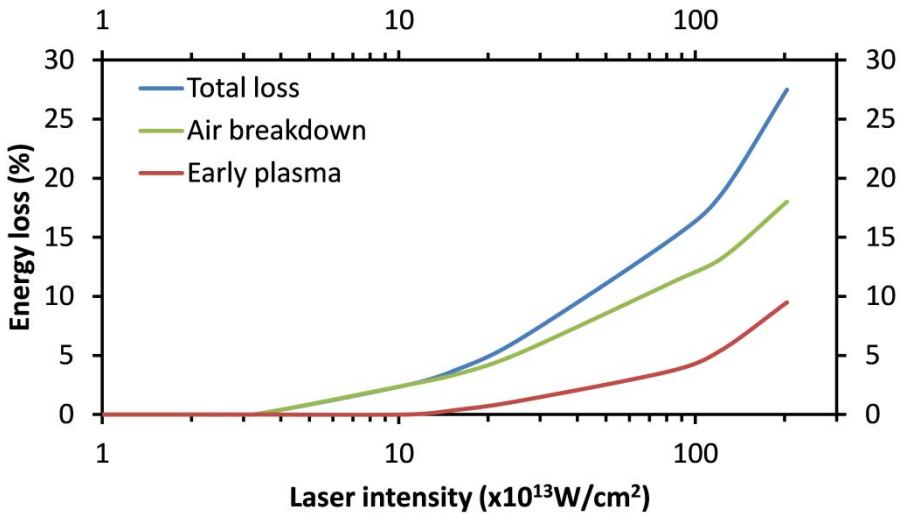

Figure 5.19. Laser beam energy loss due to early plasma absorption. Pulse duration:100 fs, wavelength: 800 nm, target material: aluminum.

Fig. 4.20 compares the energy loss of the incident laser beam in air and in vacuum at different laser intensity with the same laser and lens parameters as the cases above. For the ablation in vacuum, there is no laser induced air breakdown, and the ejected energetic electrons will diffuse freely into the vacuum without any ionization process. The absorption by the hot electrons is the only absorption mechanism of the incident laser beam energy, and the absorption rate is very low because the number density of the electrons in vacuum is small and the collision frequency is low. Therefore, at the same laser intensity, the energy loss of the incident laser beam in vacuum is much lower and negligible, compared with that in air. Accordingly, the laser beam energy deposited into the target material will be much lower in air, leading to a lower ablation depth at high laser intensity. That explains why the ablation rate in air is much lower than that in vacuum, and in the high fluence range, the ablation rate tends to saturate.

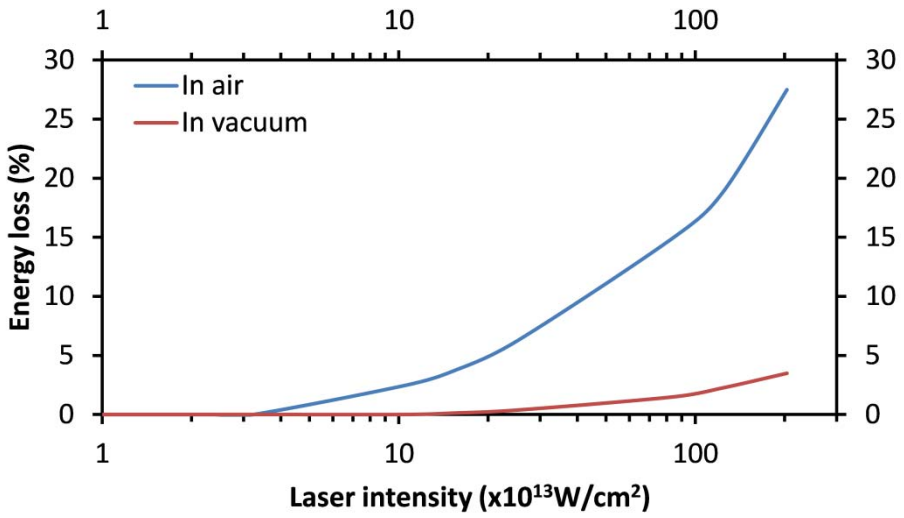

Figure 5.20. The incident laser beam energy loss in air and in vacuum. Pulse duration:100 fs, wavelength: 800 nm, target material: aluminum.

5.1.6 Summary

The early plasma dynamics during ablation of metals have been studied. It is shown that during the evolution of the early plasma, there is a quick expansion and diffusion followed by a slower second expansion, because of the fast diffusion of energetic electrons. The early stage plasma is generated by electron emission and air breakdown within tens of femtoseconds after laser irradiation, while the plume plasma forms by target material ablation after tens of picoseconds. They co-exist and expand together until hundreds of picoseconds when early plasma diffuses into the surrounding and disappears, after which only plume plasma is left.

The analysis of the emission rates for photoelectric and thermal emission at different laser intensities proved that the photoelectric emission is the dominant emission mechanism at high laser intensities, while thermal emission is more important at low intensities. The hot electron emission is important for the first several hundreds of femtoseconds and can be neglected after that. Hot electron emission and the resultant early plasma were shown to be critical to ultrashort laser-metal interaction, especially when laser intensities are high. Without considering such, the maximum electron

temperatures of the target can be overestimated by as high as 70%, at the laser intensity of $5\times10^{13} W/cm^2$.

Femtosecond laser ablation of aluminum from low to high laser intensity has been investigated by a 2D axisymmetric HD model. The ablations in air and in vacuum were compared, and the underlying physics mechanisms were analyzed. It is revealed that at low and moderate laser intensity (below 10^{14}W/cm^2), the ablation depths per pulse in air an in vacuum are similar. In the high laser intensity regime (above 10^{14}W/cm^2), there is a steep rise of the ablation depth in vacuum, while the ablation rate in air increases slowly with laser intensity. At the laser intensity of 10^{15}W/cm^2, the ablation depth in vacuum is 7 times higher than that in air. The steep change of the ablation depth in vacuum is due to the involvement of the collisionless absorption at high laser intensity. At low and moderate laser intensity, the collisional absorption is the dominant mechanism and the total absorptivity increases with laser intensity. At high laser intensity, the collisional absorption is reduced and the corresponding absorption rate drops quickly, while the collisionless absorption increases with laser intensity and becomes the dominant absorption mechanism. At the laser intensity of 10^{15}W/cm^2, the absorption by collisionless absorption is 4 times higher than that of collisional absorption. The low ablation rate at high laser intensity in air is because of strong early plasma-laser interaction. The early plasma absorption occurs at the laser intensity of 10^{14}W/cm^2, and air breakdown initiates from $3X10^{13}$ W/cm^2. It is shown in this study that the air breakdown is the dominant absorption mechanism, compared with the early plasma absorption, which consumes over 70% of the total energy loss of the incident laser beam. Because of the air breakdown and the early plasma generation in air, the absorption in air is much stronger than that in vacuum (9 times higher at the laser intensity of 10^{15}W/cm^2).

5.2 USLP Ablation of Semiconductors

There will be fast ejection of electrons and positive ions during USLP ablation of semiconductors, leading to the creation of an early stage plasma. The early plasma significantly affects the ablation process by interacting with the incident laser beam and

the target surface, and it is of crucial importance to understand its generation mechanisms and evolution dynamics. The fast electron ejection originates from the thermal and photoelectric surface electron emission, while the important ion emission processes include the thermal and non-thermal ejection, known as Coulomb explosion (CE). The two competing mechanisms predominate under different conditions and affect the material removal rate as well as the surface profile (Bashir et al.,2012, Reif et al., 2004). During the ablation process, the emission of electrons from the target surface results in the accumulation of uncompensated positive charges in the surface region, forming a strong electric field in the surface region. When the electric field is strong enough to overcome the bond among the ions, the ions will be ejected out of the target, which is called CE. It has been shown that CE is the major process for the fast ion ejection from the insulator target irradiated by a femtosecond laser (Stoian et al., 2000, Stoian et al., 2002, Reif et al. 2004, Bulgakova et al, 2004, Bulgakova et al., 2005b). However, its occurrence in semiconductors is still under a debate (Roeterdink et al., 2003, Stoian et al., 2004, Roeterdink et al., 2004, Dachraoui et al., 2006b, Dachraoui et al., 2006c, Lenner et al., 2007, Hebeisen et al., 2008, Balling and Schou, 2013). The non-thermal peaks in the time-of-flight spectra and the momentum scaling of the velocities of ejected ions were observed in (Roeterdink et al., 2003, Dachraoui et al., 2006c), which were implicated as the conclusive evidence of the existence of CE. On the other hand, some other studies (Stoian et al., 2002, Bulgakova et al, 2004, Bulgakova et al., 2005b, Stoian et al., 2004, Balling and Schou, 2013) questioned such conclusions in which the electric field strength generated in the semiconductors were considered to be below the critical electric field of CE (Stoian et al., 2002, Bulgakova et al, 2004, Bulgakova et al., 2005b), and the other possible originations of the observed phenomena were proposed, such as double layer effect and desorption (Stoian et al., 2004, Balling and Schou, 2013) Therefore, it requires a further investigation to provide clear evidence of the occurrence of CE in semiconductors. Most existing studies have focused on the relatively low laser fluence range (<10 J/cm^2), where the positive net charges are believed to be able to survive for a long time before becoming compensated by the electrons inside the bulk material. However, the underlying physics in the higher fluence regime require more study, where

the electron emission rate will be much higher and the generated electric field is expected to be stronger, which is one of the critical criteria for the existence of CE.

In this section, the femtosecond laser ablation of silicon in air at high laser fluence is studied both numerically and experimentally. The study focuses on the early stage of the ablation process, including the fast electron and ion ejection, and early plasma generation and expansion. Experimental measurements are carried out for early plasma by a pump-probe shadowgraph technique. To investigate CE at the early stage, the ion ejection, electric field distribution, and ion velocity distribution of silicon are analyzed and compared with the case of ablation of copper.

5.2.1 Validation of the HD Model

In this section, the validation of the integrated model is presented, by comparing its simulation results with experimental measurements and published data in literatures. First, the model is validated in the low laser fluence range. The laser fluence is 0.45 J/cm^2, with the wavelength of 800 nm, and the pulsed duration of 100 fs. The ion yield during the ablation of silicon is summarized in Fig. 4.21. The simulation results compared with the experimental measurements in Stoian et al. (2002) show a good agreement, where the data have been normalized to the same maximum. In this paper, the starting point (t=0) is the moment when the laser pulse just arrives on the target surface. There is no strong ion generation until 10 ps, which indicates that the ultra-fast ion ejection processes like CE do not occur under this fluence. The thermal ejection of ions is the dominant mechanism. At the same time, because of the surface electron emission during the ablation process, uncompensated positive ions will be left near the surface region. As a result, positive net charges will be accumulated in a thin surface layer, forming a strong electric field pointing into the ambient environment. Fig. 4.22 reveals the temporal evolution of the net charge at the target surface. It can be seen that the prediction of the HD model is close to the data in Stoian et al. (2002). The maximum net charge number density is around $3.5X10^{25}m^{-3}$, which is below the minimum concentration ($10^{26}m^{-3}$) (Roeterdink et al., 2003, Silvestrelli et al., 1996) required to overcome the lattice bond by Coulomb repulsion.

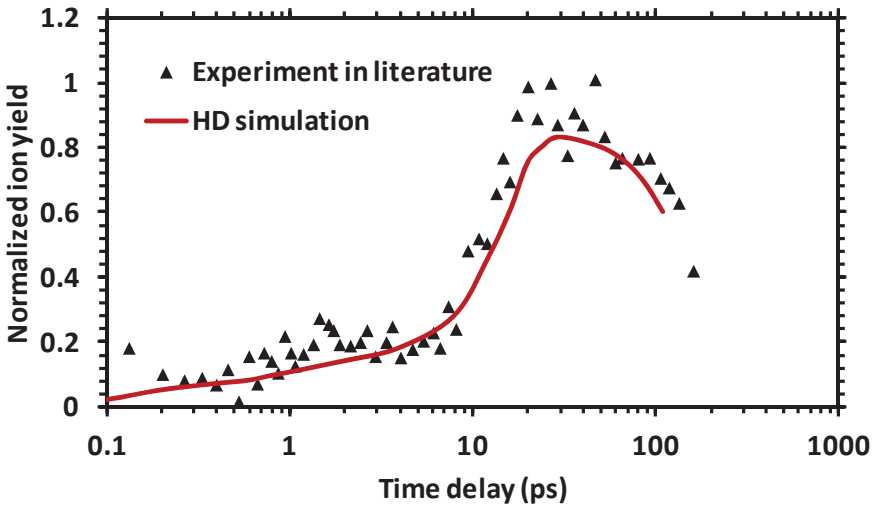

Figure 5.21. Normalized ion yield. The target is silicon. Laser wavelength: 800 nm, pulsed duration: 100 fs, and laser fluence: 0.45 J/cm^2. The experimental measurements are from Stoian et al. (2002).

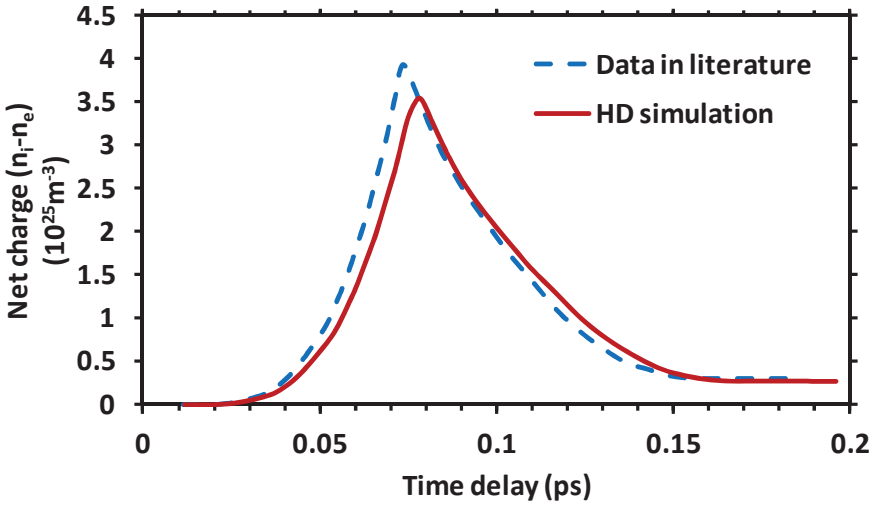

Figure 5.22. Temporal profile of net charge (n_i-n_e) during the ablation process. The target is silicon. The laser wavelength is 800 nm, the pulsed duration is 100 fs, and the laser fluence is 0.45 J/cm^2. The data for validation is from Stoian et al. (2002).

Next, high fluence ablation by the model is validated against the data available in Gordienko et al., 2005, where the pulse duration is 200 fs, the wavelength is 616 nm, and the laser intensity is $3X10^{16}W/cm^2$. Under the irradiation of the laser pulse, the electrons near the target surface will absorb the laser beam energy and be heated to a very high temperature, and then gradually transfer the energy to the lattice by electron-phonon coupling. The temporal profile of the electron temperature at the target surface is shown in Fig. 4.23, It can be seen that the electron temperature is increased to as high as $3X10^6$ K in a short amount of time (0.2 ps), and then it drops quickly to less than $1X10^6$ K within 1 ps. The simulation output of HD model is in good agreement with the data in Gordienko et al., 2005. The spatial distribution of ion number density under the same condition is presented in Fig. 4.24. The snapshot is taken at the time delay of 400 fs. It is revealed that a significant ion ejection has already occurred near the surface region by this moment, which is much earlier than that in the low fluence range. Therefore, an ultra-fast ion ejection process appears to exist in the ablation process at high fluence.

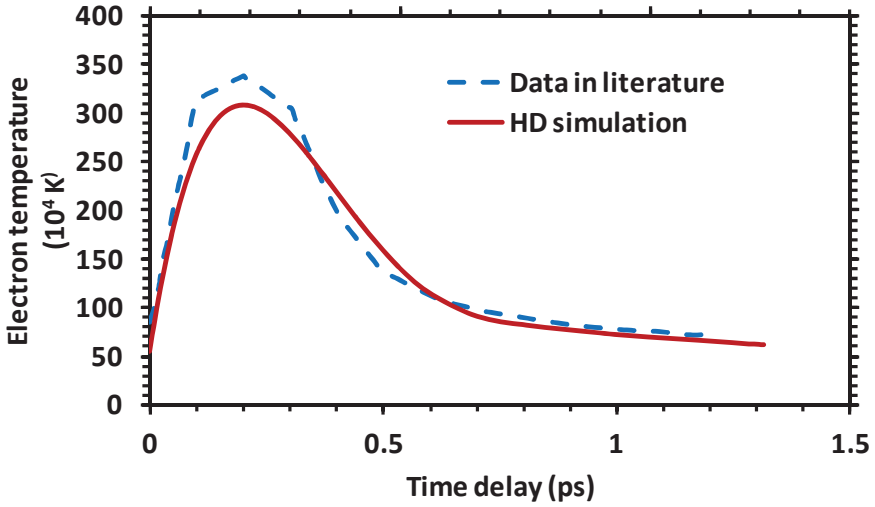

Figure 5.23. Temporal profile of electron temperature at the target surface. Target: silicon, laser wavelength: 616 nm, pulse duration: 200 fs, and laser intensity: $3\times10^{16}W/cm^2$. The data for validation is from Gordienko et al., 2005.

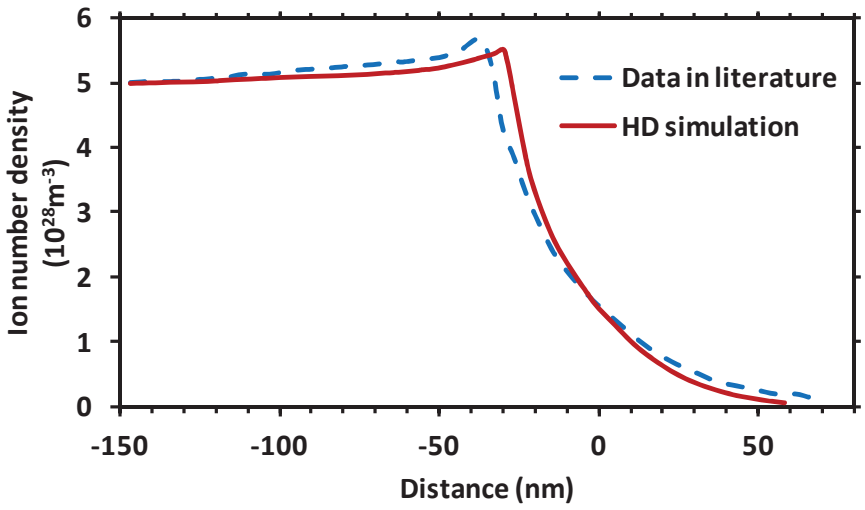

Figure 5.24. Spatial distribution of ion number density at time delay of 400 fs. Target: silicon, laser wavelength: 616 nm, pulse duration: 200 fs, and laser intensity: 3×10^{16}W/cm^2. The data for validation is from Gordienko et al., 2005.

5.2.2 Ablation Rate at High Laser Intensity

Figure 4.25 represents the calculation of the ablation depth from low to high laser fluence, validated by the experimental measurement. The ablation depth shows logarithmic dependence on the laser pulse fluence, and two distinct regimes have been experimentally observed for both metals (Nolte et al., 1997; Momma et al., 1997) and semiconductors (Besner et al., 2005, Hwang et al., 2006). The dependence of the ablation rate could be expressed based on the experimental data by two different logarithmic functions as described by Eqn. (4.1). For silicon, $\delta = 145nm$, $l = 322nm$, $I_{th}^{\ M} = 0.458J/cm^2$, and $I_{th}^{\ H} = 0.637J/cm^2$ (Hwang et al., 2006). The fitting curves of Eqn. (4.1) are compared with the experimental data in Figure 4.25, and a good agreement is shown. In the case of low-fluence ablation (< 2 J/cm^2 for silicon), the number density of hot electrons is so low that energy transfer occurs only within the area characterized by the skin depth. At higher fluences (> 2 J/cm^2 for silicon), the contribution of carrier conduction becomes important and the heat-affected region is defined by the electron-driven heat penetration depth. The simulation results are in good agreement with the experimental data. The two ablation regimes are accurately predicted by the simulation.

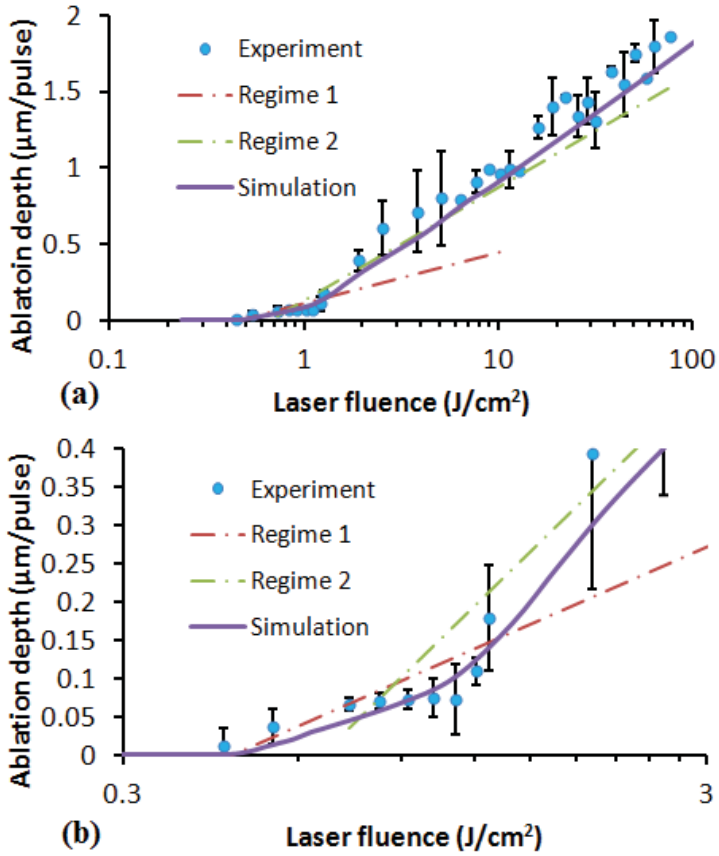

Figure 5.25. Ablation depth vs. laser fluence. (a) From low to high fluence, (b) zoom in low fluence range. Laser pulse duration: 100 fs, wavelength: 800 nm.

The ablation efficiency dependence on the laser fluence predicted by the model is shown in Figure 4.26, which is defined as the ablation volume divided by pulse energy. The experimental measurement is provided for validation, and the simulation results agree with the experimental data very well. It can be seen that the ablation efficiency first increases fast with the laser fluence. It reaches the peak value at the laser fluence around 8 J/cm^2. After that, the ablation efficiency drops quickly when the laser fluence further increases. At the laser fluence of 10 J/cm^2, the ablation efficiency drops by 50 %, compared with the peak value at 8 J/cm^2. This result indicates that the optimum laser fluence for silicon ablation in air is about 8 J/cm^2. The decrease of the ablation efficiency in the high fluence regime (> 8 J/cm^2) is attributed to the strong interaction of the laser pulse with the laser-induced plasma (Lee et al., 2008, Hwang et al., 2006). When the laser fluence is high enough, laser-induced air breakdown will occur, and the strong hot

electron emission from the target surface will generate strong early plasma. The early plasma will significantly absorb the incident laser beam energy, and reduce the laser energy deposited into the target material. Figure 4.27 summarizes the energy loss of the incident laser pulse due to the early plasma absorption. The air breakdown starts occurring at the laser fluence of 3 J/cm^2, and begins absorbing the incident laser energy. The absorption of the air breakdown increases fast as the laser fluence increases. Compared with the air breakdown absorption, the absorption of the silicon plasma (plasma caused by surface hot electron emission) is the minor issue, and can be neglected in the laser fluence range covered in this study. The air breakdown absorption is the dominant mechanism for laser-early plasma interaction as illustrated in Figure 4.27.

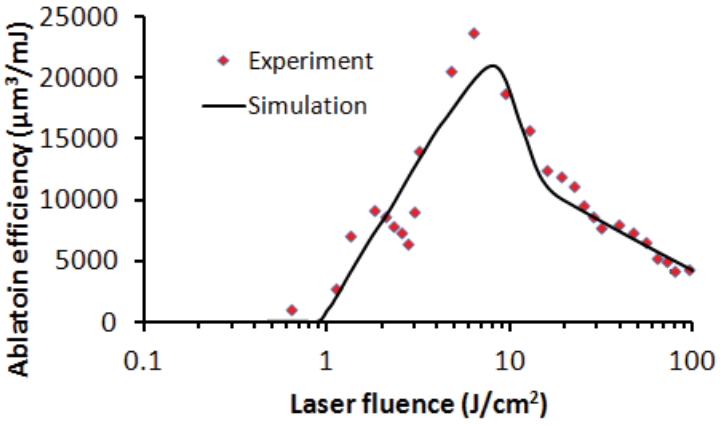

Figure 5.26. Ablation efficiency vs. laser fluence. Laser pulse duration: 100 fs, wavelength: 800 nm.

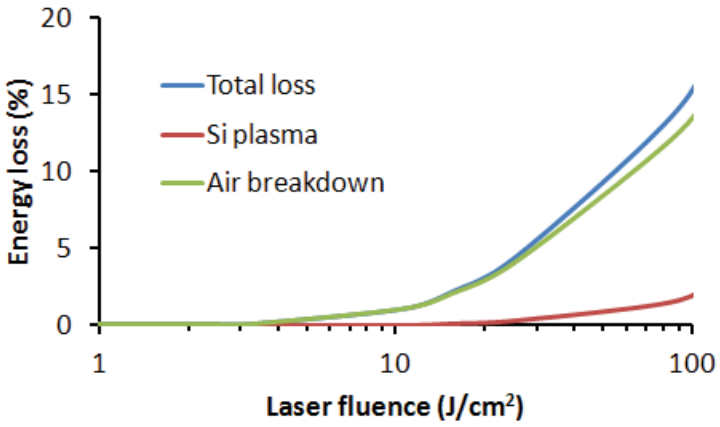

Figure 5.27. Plasma absorption of the incident laser beam energy. Laser pulse duration: 100 fs, wavelength: 800 nm.

5.2.3 Early Plasma Dynamics

The early stage plasma is a unique and important phenomenon for ultrashort laser pulse-material interaction. It is formed by the surface electron emission from the target surface under the irradiation of the ultrashort laser pulse. The ejected hot electrons are energetic enough to ionize the ambient gas, forming the early stage plasma in several or tens of femtoseconds. In some cases when ultra-fast ion ejection occurs, the early plasma also includes the target material ions ejected within tens of femtoseconds. The early plasma could significantly affect the ablation process by absorbing the incident laser beam energy and interacting with the target during its expansion. Therefore, an understanding of the early plasma dynamics is of crucial importance. First, the expansion of the early plasma from silicon target up to hundreds of picoseconds was measured by a shadowgraph measurement, when the laser pulse has the duration of 100 fs, the wavelength of 800 nm, and the laser fluence in the range of 11.2 J/cm^2 to 21 J/cm^2. Figure 4.28 presents the images of early plasma at the laser fluence of 11.2 J/cm^2. A filament (portion A) is formed above the target surface because of the laser induced air breakdown, the location of which does not move during the whole process. From 0 to 70 ps, a plasma indicated as portion B grows and diffuses fast into the air. After its disappearance, another plasma denoted as portion C expanding at a slower speed

becomes noticeable. The plasma front expansions for the cases of 11.2 J/cm^2 and 21 J/cm^2 are summarized in Figure 4.29. The plasma front is defined as the front of the electron cloud. Before 70 ps, the plasma front is determined by the front of portion B and grows very fast. After 70 ps, portion B disappears and the plasma front determined by the front of portion C appears far behind, starting a second expansion. Both portion B and portion C are caused by the electron and ion emission from the target surface and the avalanche ionization of the air (Hu at al., 2011a). However, portion B consists of the charged particles with high kinetic energies, while the emitted particles with low energies will expand and disperse slowly, forming the portion C. Portion B mainly expands in longitudinal direction, while portion C has the similar expansion speeds in longitudinal and radial directions, forming a spherical shape during the expansion.

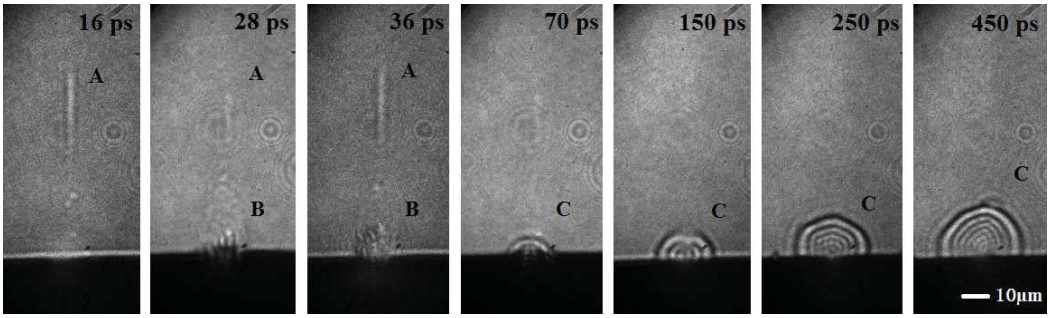

Figure 5.28. Images of early plasma by shadowgraph measurement. Target material: silicon, the laser pulse duration: 100 fs, the wavelength: 800 nm, and the laser fluence: 11.2 J/cm^2.

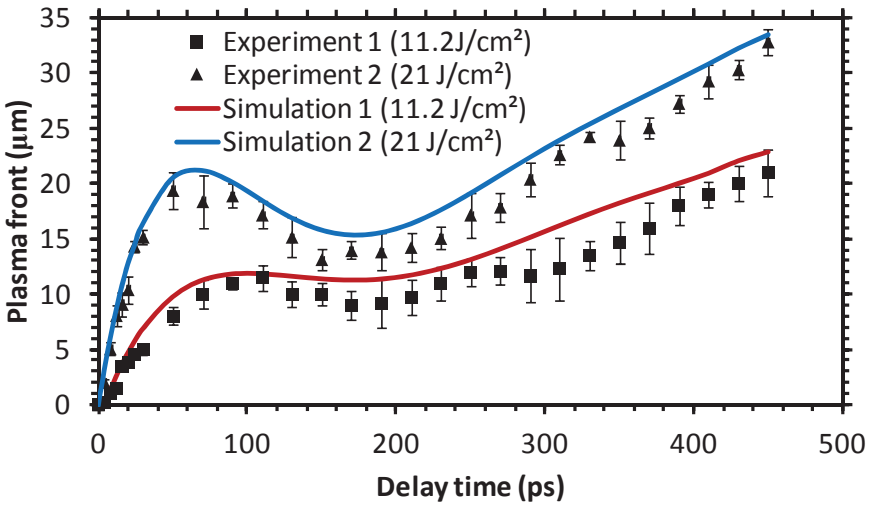

Figure 5.29. Plasma front expansion at the early stage. Target material: silicon, the laser pulse duration: 100 fs, the wavelength: 800 nm, and the laser fluence: 11.2 J/cm^2 for case 1, and 21 J/cm^2 for case 2.

As discussed earlier, the early plasma is mainly generated by the fast particle ejection from the target surface, followed by avalanche ionization of the air. Therefore, to better understand the early plasma properties and dynamics, it is important to investigate the mechanisms of particle ejection and the evolution of different particle species. The ejection of positive ions is of crucial importance because of its direct influence on the material removal rate. Figure 4.30 shows the ion front expansion during the first 100 ps of the ablation of silicon, when the wavelength is 800 nm, the pulse duration is 100 fs, and the laser fluence are 11.2 J/cm^2 and 21 J/cm^2. For comparison, the ion front expansion of copper at the fluence of 21 J/cm^2 is also presented, which is calculated by the numerical model developed in section 4.1. For copper, there is no noticeable ion ejection until around 10 ps. This is because the thermal emission is the dominant ion emission mechanism for metals, and it takes several picoseconds for the lattice to gain enough energy from the electrons. However, for silicon, even in the lower fluence case (11.2 J/cm^2), the ions start to be ejected before 0.2 ps. This is too early for the thermal emission of ions to happen. The target ions undergo an ultra-fast ion ejection mechanism, which could possibly be Coulomb explosion (CE).

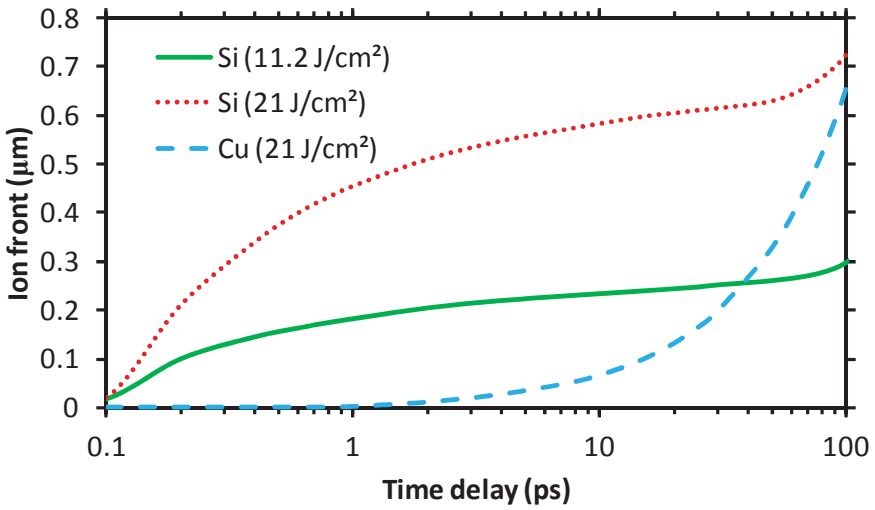

Figure 5.30. Ion front expansion during the ablation process. Target: Si and Cu. Laser wavelength: 800 nm, pulse duration: 100 fs, and laser intensity: 11.2 J/cm^2 and 21 J/cm^2 for silicon, and 21 J/cm^2 for copper.

5.2.4 Coulomb Explosion

It has been widely accepted that CE is the major mechanism for the fast emission of ions during the ultrashort laser ablation of dielectrics (Stoian et al., 2000, Stoian et al., 2002, Reif et al. 2004, Bulgakova et al, 2004, Bulgakova et al., 2005b). Because of the ultra-fast CE, the ions are ejected in the very early stage (tens of femtoseconds) with very high kinetic energies. However, the occurrence of CE in semiconductors has been heavily debated and is still not very clear. One of the key criteria on the trigger ring of CE is that the electric field generated by the accumulation of positive net charge near the target surface should exceed a critical threshold. It is reported in Bulgakova et al, 2004, Bulgakova et al., 2005b that the critical electric field should be $2.65X10^{10}$V/cm^2 for silicon. Figure 4.31 presents the temporal evolution of the electric field at the target surfaces of silicon and copper, when the wavelength is 800 nm, and the pulse duration is 100 fs. The laser fluence is 11.2 and 21 J/cm^2 for silicon, and only the case of higher fluence (21 J/cm^2) is calculated for copper. In Figure 4.31, the electric field of copper is shown after being magnified by 10 times. It can be seen that the maximum electric field of silicon is $3.9X10^{10}$V/m at 11.2 J/cm^2, and $8.4X10^{10}$V/m at 21 J/cm^2, both of which

exceed the critical electric field. However, even at the fluence of 21 J/cm^2, the maximum electric field of copper is only 2.03X10^{9}V/m, which is an order of magnitude lower than the critical value. Therefore, the electric field in silicon satisfies the criteria for CE at the fluence of 11.2 J/cm^2 and above. Besides, the surface electric field increases very fast with the laser fluence, because of the rise of the electron emission rate. On the contrary, CE is inhibited during the ablation of copper even at the laser fluence as high as 21 J/cm^2. It should be noticed that the electric field decreases very fast and drops to below the critical value after 0.15 ps. The drop of the electric field is the result of the ejection of the positive ions, and the compensation from the bulk electrons. Therefore, CE is an ultra-fast process and can only exist within the first 0.15 ps, before the electric field drops to lower than the critical value.

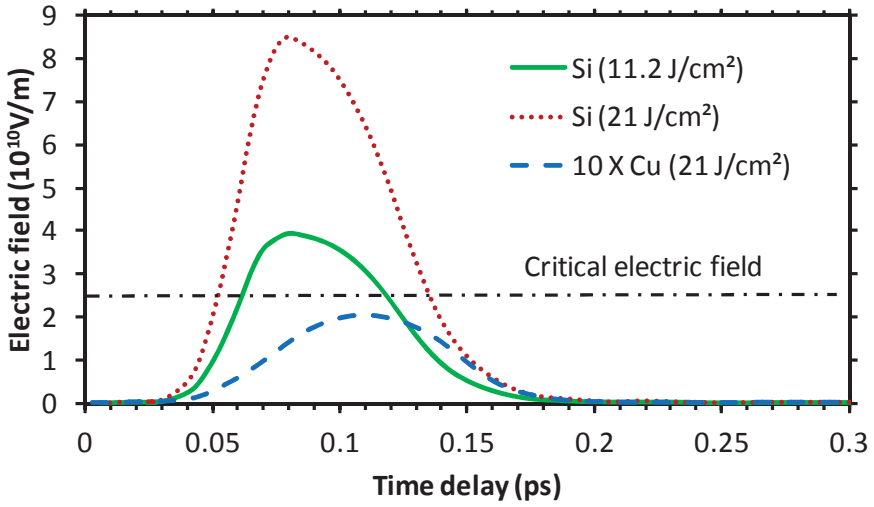

Figure 5.31. Temporal profiles of the laser-induced electric field at the target surface. Target material: silicon and copper. Pulse duration: 100 fs, wavelength: 800 nm, laser fluence: 11.2 J/cm^2 and 21 J/cm^2 for silicon, and 21 J/cm^2 for copper. The electric field of copper is magnified by 10 times.

Figure 4.32 shows the spatial distribution of the electric field inside the silicon target at the time delay of 0.1 ps. It can be seen that the electric field exceeds the critical value in a surface layer of 1.5 nm thick. These analyses above reveal that there is a fast ion ejection process for femtosecond laser ablation of silicon under the fluence above 11.2 J/cm^2, and it satisfies the ignition condition for CE. Besides CE, other mechanisms will also cause the ejection and acceleration of ions, such as double layer effect. Next, other possible ejection processes are analyzed to make sure whether CE is the dominating process.

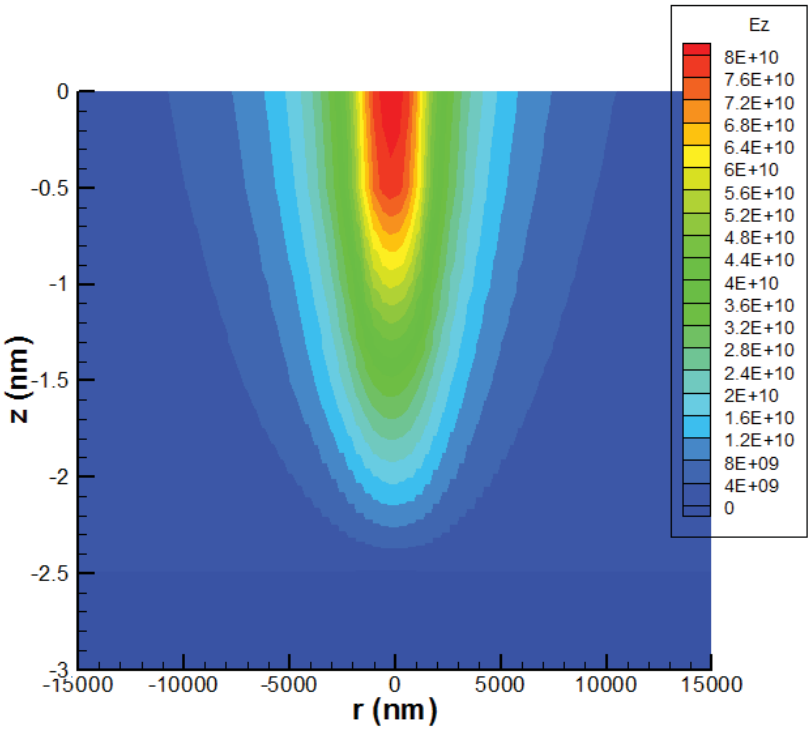

Figure 5.32. Spatial distribution of the electric field component in z direction. Target material: silicon and copper. Pulse duration: 100 fs, wavelength: 800 nm, laser fluence: 21 J/cm^2. Time delay: 0.1 ps.

Besides CE, another mechanism leading to a fast ejection of ions is the double layer (DL) effect (Plyutto et al., 1961, Bulgakova et al., 2000). Because electrons expand faster than ions, a double layer is formed during the expansion of plasma as a result of the

spatial charge separation. The fast electrons in front tend to attract the slow ions behind by Coulomb interaction. Therefore, similar to CE, the double layer effect will accelerate the ions and retard electrons. Besides, it is also an ultra-fast process. It has been reported in (Hu et al., 2011a) that the double layer effect occurs in several picoseconds during femtosecond ablation of copper. One of the distinct differences between CE and double layer effect is that CE results in momentum scaling: P~Z~v, where P is the momentum, v is the velocity, Z is the charge multiplicity of the ions, whereas double layer effect follows the energy scaling: $E \sim Z \sim v^2$, where E is the kinetic energy of the ions. Therefore, to determine the dominant mechanism for ablation of silicon, velocity distributions of different ions at the time delay of 10 ps are illustrated in Figure 4.33 (a) and (b), for the cases of silicon and copper, respectively, where the number of ions is normalized. The laser fluence is 21 J/cm^2, the wavelength is 800 nm, and the pulse duration is 100 fs. For silicon, the velocities of Si^+ and Si^{2+} follow the relation of $v_{Si}^{2+}=1.87v_{Si}^{+}$, while the relation is $v_{Cu}^{2+}=1.3v_{Cu}^{+}$ for copper. It can be seen that it is close to momentum scaling in silicon, while it is more like energy scaling in copper. The slight deviation comes from the influences from other mechanisms. For example, in silicon, besides CE, the double layer effect and thermal ejection also exist, which will contribute to the acceleration of ions. With all evidences and analysis in this section, it can be concluded that for femtosecond ablation of silicon under the fluence above 11.2 J/cm^2, CE does exist and act as the dominant mechanism for fast ion ejection in the very early stage.

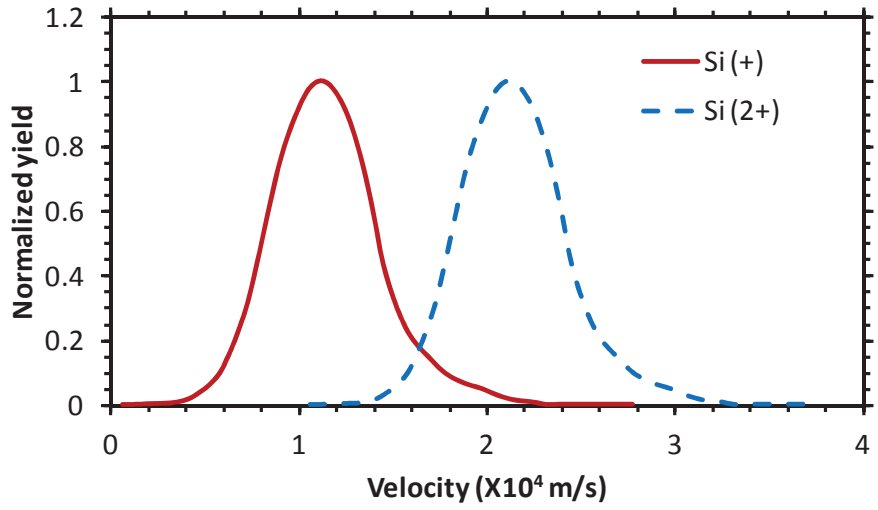

(a)

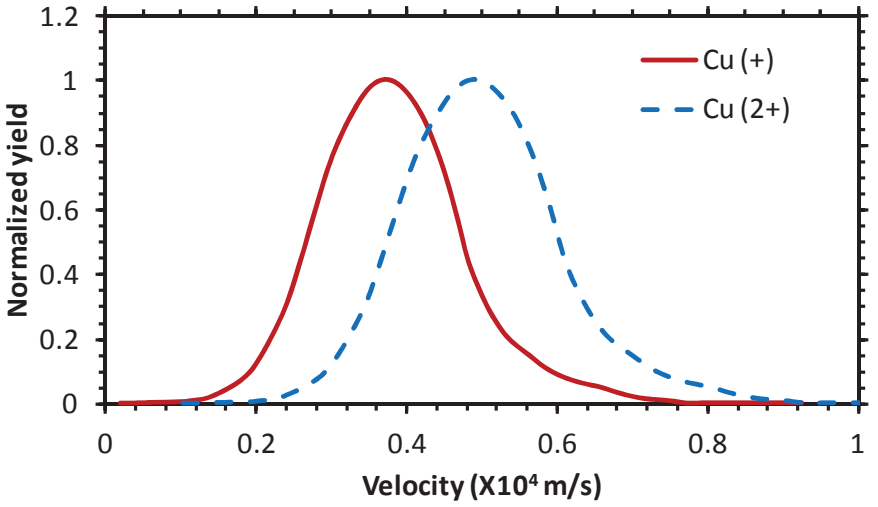

(b)

Figure 5.33. Velocity distribution of different ion species during ablation of silicon and copper. The laser fluence is 21 J/cm^2, the wavelength is 800 nm, and the pulse duration is 100 fs. The time delay is 10 ps.

5.2.5 Summary

In this section, the early plasma dynamics and the ion ejection mechanisms during femtosecond laser ablation of silicon at high fluence in air were investigated by a numerical model and experimental measurements. It is shown that the early plasma has a fast component existing until 70 ps, and a slow portion remaining up to hundreds of

picoseconds. This is caused by the difference of expansion velocities of high energy and low energy particles. The ion emission of silicon starts as early as 0.2 ps, while it is not triggered until 10 ps for copper. The maximum electric fields on the silicon surface are 3.9×10^{10}V/m at 11.2 J/cm^2, and 8.4×10^{10}V/m at 21 J/cm^2, respectively, which are both higher than the critical electric field of CE (2.65×10^{10}V/m). On the contrary, the electric field of copper is one order of magnitude lower. Besides, it was shown that the ion velocities of silicon obey the momentum scaling, while those of copper follow the energy scaling. It is proved that CE does occur during ablation of silicon at the fluence higher than 11.2 J/cm^2. It starts within tens of femtoseconds and only last for about 0.15 ps. However, the ablation of copper does not show the indication of CE at the fluence as high as 21 J/cm^2, and is instead dominated by thermal ejection and double layer effects.

6. DOUBLE-PULSE ABLATION BY USLP: ENHANCEMENT OF ABLATION RATE AND LASER-INDUCED PLASMA

In this chapter, the ultrashort double-pulse ablation of silicon is investigated. An atomistic simulation model is developed to analyze the underlying physics. It is revealed that the double-pulse ablation could significantly increase the ablation rate of silicon, compared with the single pulse ablation with the same total pulse energy, which is totally different from the case of metals. In the long pulse delay range (over 1 ps), the enhancement is caused by the metallic transition of melted silicon with the corresponding absorption efficiency. At ultrashort pulse delay (below 1 ps), the enhancement is due to the electron excitation by the first pulse. The enhancement only occurs at low and moderate laser fluence. The ablation is suppressed at high fluence due to the strong plasma shielding effect. The laser-plasma interaction and the resultant plasma enhancement by ultrashort double-pulse ablation of silicon are investigated. It is found that by carefully selecting inter-pulse delay, the plasma temperature and electron number density can be effectively increased, compared to the case of single pulse ablation. The strong plasma enhancement is observed at long pulse delay (above 20 ps), companied by the ablation rate suppression. At short pulse delay (below 20 ps), strong ablation rate enhancement is observed with no plasma enhancement. The spatial analysis of plasma temperature shows that the second pulse energy is mainly absorbed by the front portion of the plasma, where the temperature is increased the most. The plasma reheating leads to a faster expansion of the plasma.

6.1 Ablation Rate Enhancement

In the past few decades, the femtosecond laser has been proven to be a powerful tool for material processing, due to its unique nature of high peak power density, localized heat-affected zone, and low residual damage. The adoption of temporally separated pulses could induce different laser-material interaction mechanisms, and hence provides new possibilities of further enhancement of material processing. For example, the enhancement of laser-induced breakdown spectroscopy (LIBS) (Liu at al., 2013; Harilal et al., 2013) and surface nanostructures (Sivakumar et al., 2010) have been reported by adopting a double-pulse ablation setup. Semerok et al. (2004) and Povarnitsyn et al. (2009) observed that the ablation rate is strongly suppressed when the time delay is longer than the electron-lattice relaxation time. The possible responsible mechanisms include the suppression of the rarefaction wave by the shock wave induced by the second laser pulse (Povarnitsyn et al., 2009), the drop of heat conductivity at high temperature (Perez et al., 2008), and plasma shielding (Donnelly et al., 2009). The semiconductors possess different carrier dynamics and other properties, and hence could show different phenomena during double-pulse ablation. Spyridaki et al. (2003) and Koudoumas et al. (2004) observed the strong enhancement of the Si ion ejection by double pulse ablation. It was reported that the ablation rate of silicon could be enhanced by double pulse ablation at the pulse delay from several to tens of picoseconds, which is quite different from the case of metals (Singha et al., 2008; Wojakowski et al., 2009; Hu et al., 2007; Choi et al., 2002). However, it is still not clear about the optimum pulse delay for ablation enhancement and the corresponding mechanisms, especially within the ultrashort pulse delay range. In this study, the experimental and numerical investigation of ultrashort double-pulse ablation of silicon is conducted, in order to reveal the underlying physics and seek for the optimal conditions of the ablation process.

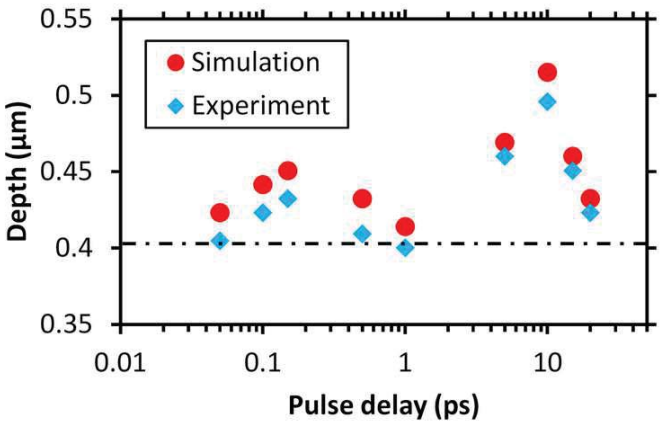

Figure 6.1 Ablation depth at different pulse delay with laser fluence of 1 J/cm^2. Dashed line: single pulse ablation depth with the laser fluence of 2 J/cm^2.

Figure 6.1 shows the dependence of ablation depth per pulse-pair on the pulse delay. The pulse delay is varied from 10 fs to 20 ps, and the laser fluence is 1 J/cm^2. The simulation results show a good agreement with the measurements. The ablation depth per pulse by single pulse ablation with the same total energy is also shown for comparison. It is discovered that the ablation depth of silicon is significantly increased by double-pulse ablation in certain pulse delay ranges, which is quite different from the behavior of metals (Semerok et al., 2004; Povarnitsyn et al., 2009). The enhancement occurs in two pulse delay ranges: the ultrashort pulse delay (below 1 ps) and short pulse delay (1~20 ps). At the pulse delay above 1 ps, the ablation depth first increases with the pulse delay, and then starts to drop after reaching the peak value at around 10 ps, which was also reported by Choi et al. (2002). The similar behavior is also observed at the pulse delay below 1ps, and the enhancement peak is observed at around 150 fs. This phenomenon was not discussed before. Different mechanisms should be responsible for these ablation enhancements at different pulse delays. The ablation enhancement in the delay range from 1 ps to 20 ps should be attributed to the metallic transition of the melted silicon. The thermally melted silicon will have a significant amount of free electrons, and hence stronger coupling with the second laser pulse (Choi et al., 2002; Hu et al., 2007). Figure 6.2 shows the spatial lattice temperature distribution by single pulse ablation at the time

of 1, 10, and 20 ps after the pulse irradiation. They were selected to be the time points before the irradiation of the second pulse, in order to explain the difference in ablation enhancement with different pulse delays. The lattice temperature decreases quickly from the surface into the bulk. The silicon is considered to be melted when its local temperature exceeds the melting point (1687 K). It is revealed that the lattice temperature reaches the maximum value at the delay of 10 ps, and creates the thickest melted layer. In the melted layer, the absorption coefficient is significantly increased due to the increase of free electrons. It is the reason why the strongest enhancement of the ablation rate occurs at around 10 ps delay.

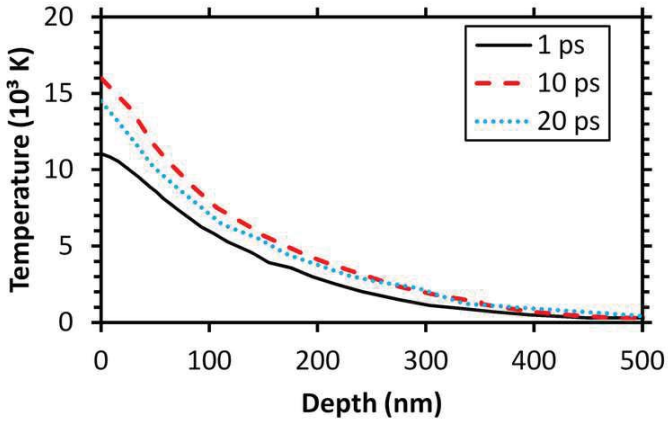

Figure 6.2 Spatial distribution of lattice temperature at the time delay of 1 ps, 10 ps, and 20 ps. Laser fluence: 1 J/cm^2.

From Figure 6.1, it is observed that at the pulse delay shorter than 1 ps, there is another ablation enhancement. The strongest enhancement occurs at the pulse delay around 150 fs. At this early stage, the lattice temperature is still very low and cannot be thermally melted. Therefore, another different mechanism should be responsible for this ablation enhancement. Figure 6.3 shows the evolution of free electron number density (a), surface reflectivity, and absorption coefficient (b) during and after the first pulse irradiation. The first laser pulse will excite the bonded electrons from the valance band to the conduction band, and create a large amount of free electrons. The free electron

number density increases quickly and reaches the peak number at around 130 fs. Gan and Chen (2011) reported that the surface reflectivity will first decrease with the electron number density, reaching the minimum value at around 6×10^{21} cm^{-3}, and then starts to increase again. Therefore, it could be seen in Figure 6.3 (b) that the surface reflectivity first decrease, and then increase, due to the change of free electron number density. On the other hand, the absorption coefficient of the silicon will significantly increase as the increase of free electron number density. The increases of surface reflectivity and absorption coefficient play as opposite roles, since the former reduces the laser energy deposition, while the latter provides an enhancement. From Figure 6.3 (b), it can be seen that the change of surface reflectivity is only about 50%, while the absorption coefficient could be increased by hundreds of times. Therefore, in this process, the change of the absorption coefficient is the dominating mechanism, and thus leads to the enhancement of the energy coupling of the second laser pulse. This conclusion is supported that the maximum ablation enhancement at the time delay when the maximum absorption coefficient is reached. In the mean time, the strong electronic excitation will significantly weaken the interatomic bond and lead to the lattice disorder, finally trigger the non-thermal melting. It could possibly enhance the ablation since the interatomic bonds are weakened and the cold liquid is easier to be ablated than solid. Typically, it is believed that the critical electron density for non-thermal melting is 10^{21}~10^{22} cm^{-3} (Chen et al., 2005). In this study, as shown in Figure 3, the electron number density at the first few hundred has exceeded the critical density, indicating the occurrence of the non-thermal melting. The Stillinger-Weber potential adopted in this study cannot explicitly account for non-thermal melting. To capture this phenomenon, the silicon was set to liquid state (density: 2.53 g/cm^3, and EAM potential was adopted) when the electron number density exceeded $2.74\times10^{21}cm^{-3}$ (Chen et al., 2005). The effect of non-thermal melting was analyzed by calculating the ablation depth with/without the consideration of non-thermal melting. It was found to only increase by 4% after considering the non-thermal melting. Therefore, the lattice disorder by non-thermal melting only makes minor contribution to this phenomenon. The dominating mechanism for ablation enhancement with ultrashort pulse delay should be absorption enhancement induced by electronic excitation.

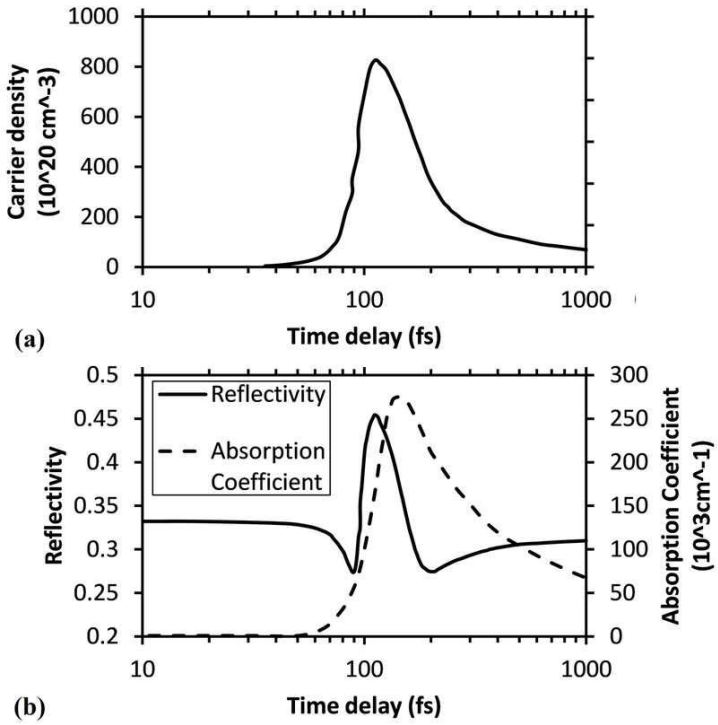

Figure 6.3 Evolution of electron number density (a), surface reflectivity, and absorption coefficient (b) during and after the irradiation of the first pulse at the fluence of 1 J/cm^2.

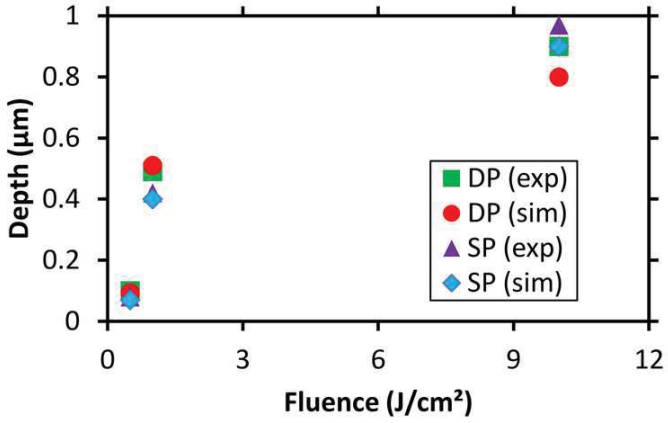

Figure 6.4 Ablation depth by double pulse and single pulse ablation.

The effect of laser fluence on the ablation rate is shown in Figure 6.4. The ablation rates at different laser fluences, with the pulse delay of 10 ps are compared with the single pulse ablations with the same total energy. The simulation results agree with the experimental data very well. It is revealed that the ablation rates are enhanced by double-pulse ablation at low and moderate fluences due to the metallic transition of the melted silicon. However, the enhancement is suppressed at high fluence, which is attributed to the plasma shielding effect. At low and moderate fluences, the laser induced plasma has a low density, and thus does not block the second pulse significantly. However, at the high fluence, the plasma density is very high and can significantly absorb the energy of the incident pulse. At 0.5 J/cm^2, the ablation rate is increased by 16% by double pulse ablation, while it is enhanced by over 20% at 1 J/cm^2. Therefore, the ablation rate is enhanced the most in the moderate fluence range, where the plasma shielding does not come into play, and the absorption enhancement is strong.

6.2 Plasma Enhancement

The laser-induced plasma and laser-plasma interaction are key problems of laser-induced breakdown spectroscopy (LIBS) (Margetic et al., 2000; Eland et al., 2001; Scaffidi et al., 2003; Scaffidi et al., 2006), X-ray emission (Miura et al., 2000; Rousse et al., 2004), high-order harmonic generation (Zhou et al., 1996; Li and Chiu, 2013), fast ignition scheme (Key, 2001; Kodama et al., 2002), and ion acceleration (Clark et al., 2000; Silva et al., 2004). In many applications, it is of essential importance to enhance the plasma intensity, that is, to increase plasma temperature and electron number density. For example, in LIBS, it is critical to enhance the plasma, and thus to increase the plasma emission intensity and the signal/noise ratio. Several different techniques have been developed to enhance the plasma density, such as plasma confinement (Hou et al., 2013; Wang et al., 2012) and double-pulse ablation (Semerok et al., 2004; Scuderi et al., 2005; Piñon and Anglos, 2009; Harilal et al., 2013; Liu et al., 2013; Mildner et al., 2013). The double-pulse technique can be carried out in two different pulse configurations, called orthogonal and collinear, referring to the relative directions of the two laser pulses. It has been proven to be a very effective method of enhancing the intensity of laser-induced

plasma by one order of magnitude or even higher (Semerok et al., 2004; Scuderi et al., 2005; Piñon and Anglos, 2009; Harilal et al., 2013; Liu et al., 2013; Mildner et al., 2013). In the meantime, the enhancement of the yield of ions and nanoparticles was also observed during double-pulse ablation (Amoruso et al., 2004; Amoruso et al., 2007b; Amoruso et al., 2008; Amoruso et al., 2010; Povarnitsyn et al., 2007; Donnelly et al., 2009). Additionally, the collinear double-pulse ablation could also be adopted to control the material removal rate. In general, material removal and plasma enhancement are two competing processes, sharing the incident laser energy. Despite the extensive studies in double pulse ablation, it is still not clear how the laser energy is absorbed by the plasma, and the optimum condition for plasma enhancement and ablation enhancement is still not known.

This study reports the experimental investigation and numerical analysis of the collinear double-pulse ablation of silicon by a femtosecond laser. The plasma emission spectrum was measured by a spectrometer to calculate the plasma temperature and electron number density. An integrated atomistic model was used to help analyze the laser-plasma interaction and plasma dynamics. The effect of inter-pulse delay on the plasma enhancement was investigated, in order to determine the optimal condition for plasma enhancement. The dominating plasma enhancement mechanisms were studied, to explore the potential applications like LIBS, plasma etching, etc.

Figure 6.5 and Figure 6.6 respectively show the time-resolved evolutions of plasma temperature and electron number density by different ablation methods. For double pulse ablation, the laser fluence was 1 J/cm^2 per pulse, and pulse delay was 70 ps. As a comparison, the cases of single pulse ablation with laser fluence of 1 J/cm^2 and 2 J/cm^2 were also studied. The gate width of the ICCD camera was set to be 5 ns in order to measure the transient emission spectral lines at different time points. It is observed that both the plasma temperature and the electron number density decrease slowly after the laser irradiation, due to the plasma expansion and diffusion. By increasing the laser fluence from 1 J/cm^2 to 2 J/cm^2 for single pulse ablation, the plasma temperature is increased by about 18%. By adopting double-pulse ablation, it is further enhanced by 44% and 21% to single pulse ablation with 1 J/cm^2 and 2 J/cm^2, respectively. Similarly,

the double-pulse ablation increased the electron number density by 56% and 23% to single pulse ablation with 1 J/cm^2 and 2 J/cm^2, respectively. It should be noted that the plasma emission intensity is an exponential function of the inverse of the plasma temperature. When the plasma temperature is increased by 10%, the plasma emission intensity can be increased by nearly one order of magnitude in this case. Therefore, the double-pulse ablation could be an effective way of increasing the plasma intensity under certain conditions. It is thus important to study the effect of inter-pulse delay and determine the optimum condition for plasma enhancement.

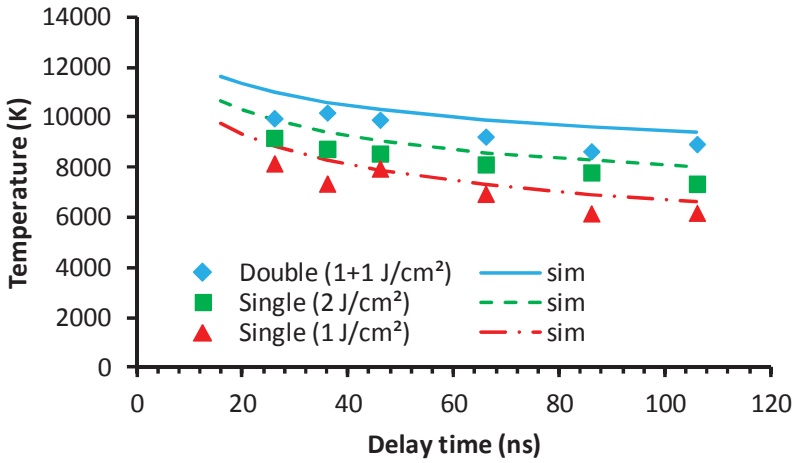

Figure 6.5 Time-resolved plasma temperature evolution after the laser irradiation by double pulse ablation (1+1 J/cm^2, 70 ps) and single pulse ablation (1 J/cm^2 and 2 J/cm^2).

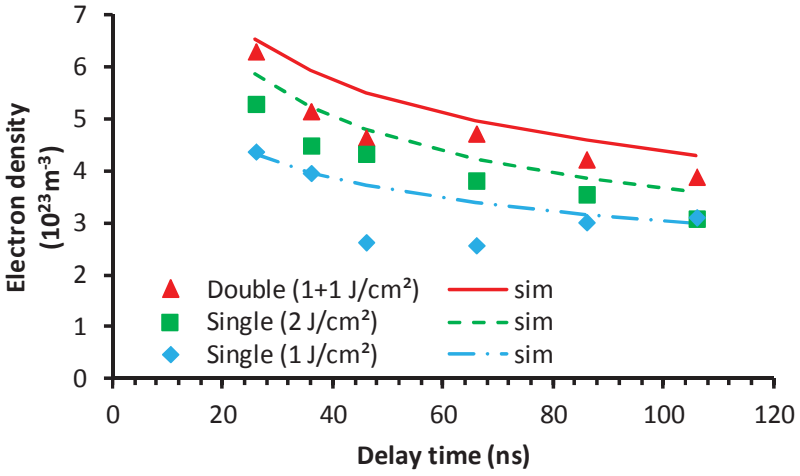

Figure 6.6 Time-resolved electron number density evolution after the laser irradiation by double pulse ablation (1+1 J/cm^2, 70 ps) and single pulse ablation (1 J/cm^2 and 2 J/cm^2).

Figure 6.7 shows the plasma temperature with different inter-pulse delay times. The gate width of the ICCD camera was 10 ns, and therefore the measured plasma temperature was the average value within the first 10 ns. The dash-dotted line represents the plasma temperature by single pulse ablation (2 J/cm^2). It is revealed that the plasma temperature by double pulse ablation remains constant within the pulse delay below 20 ps. Starting from 20 ps, the plasma temperature increases with the inter-pulse delay, reaching the peak value at about 70 ps and then starting to drop. Therefore, by carefully selecting the inter-pulse delay, the double pulse ablation could effectively increase the plasma temperature. Under the conditions used in this study, the optimum inter-pulse delay is about 70 ps, where the plasma temperature could be increased by 29% by double-pulse ablation.

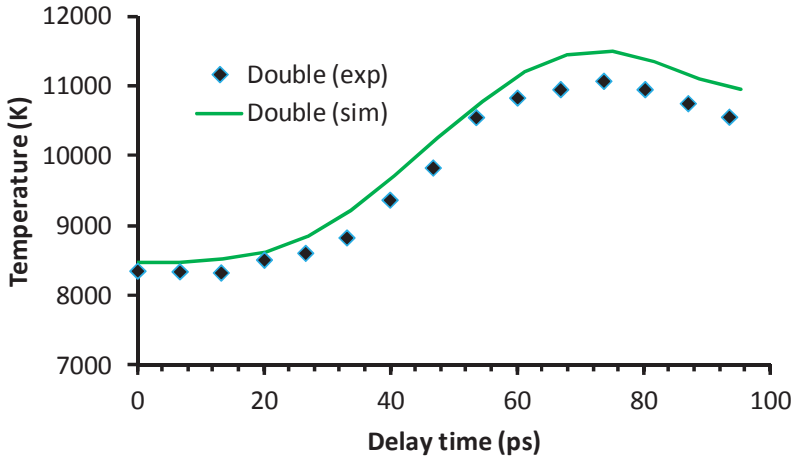

Figure 6.7 Plasma temperature with different inter-pulse delay. Laser fluence: 1 J/cm^2 per pulse. The dotted line is the plasma temperature by single pulse ablation with the fluence of 2 J/cm^2.

The plasma enhancement can be attributed to two possible reasons: plasma reheating by the second pulse and the more removed material coming from the target. To reveal the dominating mechanism, Figure 6.8 shows the time-resolved plasma temperature spatial distribution after the laser irradiation by double pulse ablation (1+1 J/cm^2, 70 ps) and single pulse ablation (1 J/cm^2). At 10 ps, a strong plasma with the peak temperature about 13000 K has been generated by the first pulse and is expanding into the ambient area. At 75 ps, for single pulse ablation, the plasma has expanded to a scale about 2 μm, and the peak temperature has dropped to about 10000 K. For double-pulse ablation, the second pulse irradiation has been terminated at this time. It can be seen that the plasma temperature is higher by about 14% than that of single pulse ablation. Although the whole plasma area has been heated to a higher temperature, the temperature of the front portion is increased the most. There exist two temperature peaks inside the plasma, and the temperature in the front portion is higher than the rear portion, due to the second pulse reheating. This result suggests that the major reason for plasma enhancement is due to the plasma reheating by the second pulse, rather than the more material removal from the target. Additionally, it is observed that most of the energy of the second pulse is

absorbed by the front portion of the plasma. After being heated by the second pulse, the plasma expands much faster than the one generated by single pulse ablation. At 90 ps, the plasma generated by double-pulse ablation expands 20% faster than the one by single pulse ablation. A similar phenomenon has been reported by Corsi et al., (2004) by the shadow graphic measurement of the plasma during double-pulse ns laser ablation. The peak temperature generated by the second pulse is lower than the value by the single pulse at 10 ps. It is because that the energy of the second pulse is absorbed and spread into a larger area. Additionally, a portion of the second pulse energy is consumed to further ionize the plasma. As shown in Figure 6.9, similar to the evolution of plasma temperature, the electron number density in the front portion of the plasma is significantly increased by the second pulse and expands much faster than the case of single pulse ablation.

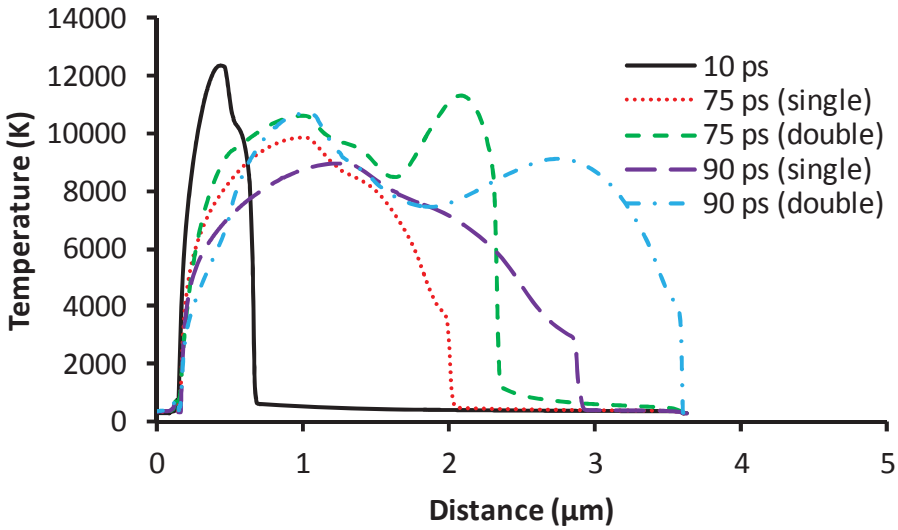

Figure 6.8 Plasma temperature spatial distribution evolution after the laser irradiation by double pulse ablation (1+1 J/cm^2, 70 ps) and single pulse ablation (1 J/cm^2).

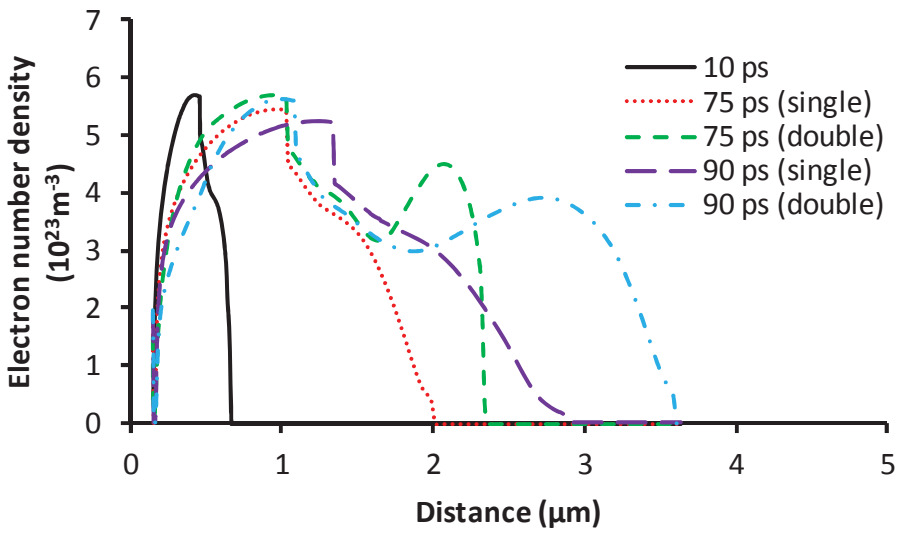

Figure 6.9 Electron number density spatial distribution evolution after the laser irradiation by double pulse ablation (1+1 J/cm^2, 70 ps) and single pulse ablation (1 J/cm^2).

The ablation rates by single pulse ablation (1 J/cm^2 and 2 J/cm^2) and double pulse ablation (1+1J/cm^2, delay: 10 ps and 70 ps) are shown in Figure 6.10. It is revealed that by double pulse ablation with 10 ps delay, the ablation depth is enhanced by 25%. As discussed previous section, 10 ps is the optimum pulse delay for the ablation rate enhancement purpose. If the delay time is set to 70 ps, the ablation is significantly suppressed due to the plasma shielding effect. However, the ablation depth is still higher than the single pulse ablation with 1 J/cm^2, which implies that a portion of the laser-induced energy can still be delivered to the target and contribute to the ablation. Additionally, the heated plasma could also interact with the target surface and help to slightly enhance the ablation. According to the simulation results, around 89% of the non-reflected laser energy is absorbed by the plasma, and only 11% is further delivered into the target material. This result further supports the conclusion that the further material removal by the second pulse only makes a minor contribution to the plasma enhancement at around 70 ps. As mentioned before, the material removal and plasma

enhancement are two competing processes, sharing the incident laser energy. It is not surprising that at the strong plasma enhancement point, the ablation rate is low, and vice-versa.

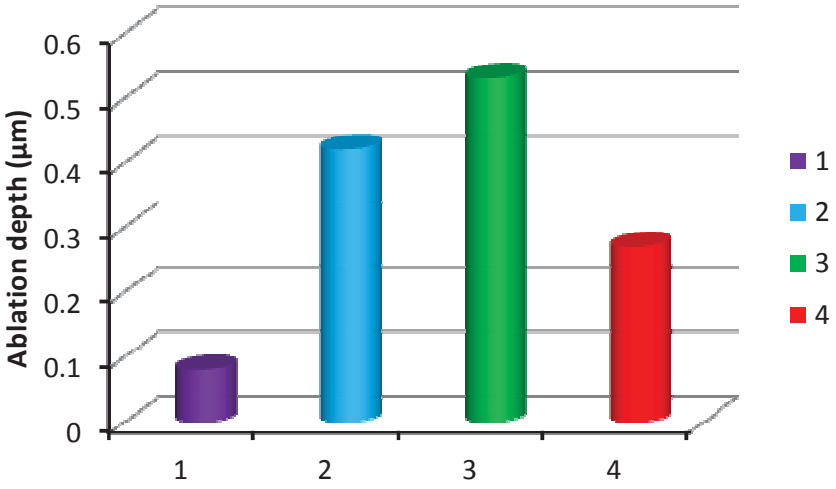

Figure 6.10 Ablation depth at different cases. 1: single pulse ablation (1 J/cm^2); 2: single pulse ablation (2 J/cm^2); 3: double pulse ablation (1+1 J/cm^2, 10 ps); 4: double pulse ablation (1+1 J/cm^2, 70 ps).

6.3 Summary

In summary, it is revealed that unlike the case of metals, the double-pulse ablation could help to enhance the ablation rate of silicon. The enhancement was discovered in two delay ranges, caused by different physical mechanisms. At the time delay longer than 1 ps, the enhancement is due to the metallic transition of the melted silicon, and the resultant higher coupling efficiency of the second laser pulse. The strongest enhancement occurs at around 10 ps, where the thickest melted layer is generated. At the time delay lower than 1 ps, the enhancement is caused by the electron excitation by the first pulse. The excited free electrons significantly increase the absorption coefficient, and confine the energy of the second pulse in a smaller region with higher energy density. The study on the effect of laser fluence shows that the ablation is enhanced at low and moderate laser fluence, but its enhancement is suppressed at high laser fluence, due to the strong

plasma shielding effect. The maximum enhancement occurs at the laser fluence of 1 J/cm^2 and the pulse delay of 10 ps.

The plasma enhancement effect by ultrashort double-pulse ablation was investigated. It was revealed that double-pulse ablation could significantly increase the plasma temperature and electron number density, compared to single pulse ablation with the same total pulse energy. By varying the inter-pulse delay, the plasma temperature first increases with the inter-pulse delay, reaches the peak value at about 70 ps, and then starts to drop. Therefore, under the condition of this study (100 fs, 800 nm, 1J/cm2 per pulse), the optimum inter-pulse delay for plasma enhancement is around 70 ps, where the plasma temperature and electron number density can be increased by over 20%. The spatial analysis of plasma temperature shows that the second pulse energy is mainly absorbed by the front portion of the generated plasma, and hence increases the temperature of front portion. Therefore, the dominating mechanism for plasma enhancement is the plasma reheating by the second pulse, rather than the more material removal from the target. This conclusion is further supported by the fact that at long pulse delay (above 20 ps), the ablation rate is strongly suppressed, due to the plasma shielding effect. Only 11% of the second pulse energy was observed to be delivered into the target in this study case. With short pulse delay (below 20 ps), the plasma is not significantly enhanced, but the ablation depth could be increased a lot.

7. CONCLUSIONS AND FUTURE WORK

This chapter summarizes the conclusions in this ultrashort laser pulse ablation research, as well as proposed future study subjects.

7.1 Conclusions

In this study, 2D axisymmetric comprehensive HD models for femtosecond laser ablation of metals and semiconductors have been developed. The models are combined with TTM, hydrodynamic and QEOS models, and cover the complex physics during laser-matter interaction to simulate the interaction process in a large time scale (from the very beginning to 50 nanoseconds). For laser beams with axisymmetric profiles, this 2D axisymmetric model suffices to describe the three-dimensional behavior. The HD models presented in this research are capable of simulating the ablation process of metals and semiconductors over a wide range of laser intensity (up to 10^{16} W/cm^2), laser wavelength (visible to infrared), and ambient enjoinment (in vacuum and ambient gases).

Experimental setups were established for measurement of both early plasma and plume plasma during USLP ablation. The early stage plasma was measured by a shadowgraphic method in the early stage of ablation up to hundreds of picoseconds, with the time resolution of 1 ps. The plume plasma was also measured by a direct fluorescence measurement. The measurement was carried out up to 50 ns.

The USLP ablation of metals was studied by the developed model and the experimental measurements. It is shown that during the evolution of the early plasma, there is a quick expansion and diffusion followed by a slower second expansion, because of the fast diffusion of energetic electrons. The early stage plasma is generated by electron emission and air breakdown within tens of femtoseconds after laser irradiation,

while the plume plasma forms by target material ablation after tens of picoseconds. Photoelectric emission is found to be the dominant emission mechanism at high laser intensities, while thermal emission is more important at low intensities. Hot electron emission and the resultant early plasma were shown to be critical to ultrashort laser-metal interaction, especially when laser intensities are high. The ablation rates in air and in vacuum over a wide range of intensity were studied and compared. The ablation rates of two cases are similar at low and moderate laser intensity (below 10^{14}W/cm^2). In the high laser intensity regime (above 10^{14}W/cm^2), there is a steep rise of the ablation depth in vacuum, due to the involvement of the collisionless absorption, while the ablation rate in air increases slowly with laser intensity because of strong early plasma-laser interaction. Because of the air breakdown and the early plasma generation in air, the absorption in air is much stronger than that in vacuum (9 times higher at the laser intensity of 10^{15}W/cm^2).

The early plasma dynamics and the ion ejection mechanisms during femtosecond laser ablation of silicon at high fluence in air were investigated by a numerical model and experimental measurements. It is shown that the early plasma has a fast component existing until 70 ps, and a slow portion remaining up to hundreds of picoseconds. This is caused by the difference of expansion velocities of high energy and low energy particles. It is found that the ion emission of silicon starts as early as 0.2 ps, and the maximum electric fields on the surface exceed the critical value of CE. On the contrary, the electric field of copper is an order of magnitude lower than the threshold. Besides, it was shown that the ion velocities of silicon obey the momentum scaling, while those of copper follow the energy scaling. It is proved that CE does occur during ablation of silicon at the fluence higher than 11.2 J/cm^2. However, the ablation of copper does not show the indication of CE at the fluence as high as 21 J/cm^2, and is instead dominated by thermal ejection and double layer effects.

DP ablation and laser-plasma interaction were studied by a self-closed integrated atomistic model. It includes molecular dynamics (MD), Monte Carlo (MC), particle-in-cell (PIC), and beam propagation (BP) method. The plasma emission spectral lines were measured by a spectrometer to calculate the electron number density and plasma temperature. It is revealed that unlike the case of metals, the DP ablation could help to

enhance the ablation rate of silicon. The enhancement was discovered in two delay ranges, caused by different physical mechanisms. At the time delay longer than 1 ps, the enhancement is due to the metallic transition of the melted silicon, and the resultant higher coupling efficiency of the second laser pulse. The strongest enhancement occurs at around 10 ps, where the thickest melted layer is generated. At the time delay lower than 1 ps, the enhancement is caused by the electron excitation by the first pulse. The excited free electrons significantly increase the absorption coefficient, and confine the energy of the second pulse in a smaller region with higher energy density. The study on the effect of laser fluence shows that the ablation is enhanced at low (0.5 J/cm^2) and moderate (1 J/cm^2) laser fluence, but its enhancement is suppressed at high laser fluence (10 J/cm^2), due to the strong plasma shielding effect. The maximum enhancement occurs at the laser fluence of 1 J/cm^2 and the pulse delay of 10 ps. It was revealed that DP ablation could significantly increase the plasma temperature and electron number density, compared to single pulse ablation with the same total pulse energy. By varying the inter-pulse delay, the plasma temperature first increases with the inter-pulse delay, reaches the peak value at about 70 ps, and then starts to drop. Therefore, under the condition of this study (100 fs, 800 nm, 1J/cm2 per pulse), the optimum inter-pulse delay for plasma enhancement is around 70 ps, where the plasma temperature and electron number density can be increased by over 20%. The spatial analysis of plasma temperature shows that the second pulse energy is mainly absorbed by the front portion of the generated plasma, and hence increases the temperature of front portion. Therefore, the dominating mechanism for plasma enhancement is the plasma reheating by the second pulse, rather than the more material removal from the target. This conclusion is further supported by the fact that at long pulse delay (above 20 ps), the ablation rate is strongly suppressed, due to the plasma shielding effect. Only 11% of the second pulse energy was observed to be delivered into the target in this study case. With short pulse delay (below 20 ps), the plasma is not significantly enhanced, but the ablation depth could be increased a lot.

7.2 Recommendations for the Future Work

Based on the current studies, several subjects are proposed for the future work.

- First, since laser-induced plasma dynamics and laser-plasma interaction have been studied, the plasma-target interaction could be studied to seek the possibilities of laser-induced plasma-etching.
- Second, DP ablation has been proven to be very effective to enhance the ablation rate and laser-induced plasma, and thus it is necessary to further investigate and optimize its effect to create super dense plasma for LIBS, plasma etching, etc.
- Third, USLP ablation has been investigated in an intensity range from 10^{12}W/cm^2 to 10^{16}W/cm^2. It can be conjectured that new physical mechanisms will be involved if the intensity is further raised. It is necessary to study the ablation at high laser intensity with a proper numerical model.
- Fourth, the current study investigated the USLP ablation of metals and semiconductors. A further study on USLP ablation of transparent dielectric materials could be conducted, which is one of the promising advantages of USLP.
- Last, the current study focuses on laser material removal processes. A new study on laser surface treatment, such as micro/nano-scale surface structure, texturing could be studied.

LIST OF REFERENCES

LIST OF REFERENCES

Abraham, F.F., and J.Q. Broughton. 1986. Pulsed melting of silicon (111) and (100) surfaces simulated by molecular dynamics. Physical Review Letters. 56:734-737.

Afanasiev Y.V., N.N. Demchenko, V.A. Isakov, I.N. Zavestovskaia, and B.N. Chichkov. 2002a. Threshold characteristics of short and ultrashort laser pulse ablation of metals. Proceedings of SPIE. 4760:424-431.

Afanasiev, Y.V., B.N. Chichkov, V.A. Isakov, A.P. Kanavin, and S.A. Uryupin. 2002b. Generation of acoustic oscillations by short laser pulses in metals. Proceeding of SPIE. 4760:621-632.

Ageev, V.P., A.A. Gorbunov, V.I. Konov, D.S. Lukovnikov, S.V. Mel'chenko, A.M. Prokhorov, and V.F. Tarasenko. 1983. Heating of metals by nanosecond XeCl* laser radiation pulses generating a surface plasma. Sov. J. Quantum Electron. 13(7):954-956.

Agranat, M.B., N.E. Andreev, S.I. Ashitkov, M.E. Veĭsman, P.R. Levashov, A.V. Ovchinnikov, D.S. Sitnikov, V.E. Fortov, and K.V. Khishchenko. 2007. Determination of the transport and optical properties of a nonideal solid-density plasma produced by femtosecond laser pulses. JETP Letters. 85:271-276.

Amoruso, S., R. Bruzzese, N. Spinelli, R. Velotta, M. Vitiello, X. Wang, G. Ausanio, V. Iannotti, and L. Lanotte. 2004. Generation of silicon nanoparticles via femtosecond laser ablation in vacuum. Applied Physics Letters. 84:4502-4504.

Amoruso, S., R. Bruzzese, C. Pagano, and X. Wang. 2007a. Features of plasma plume evolution and material removal efficiency during femtosecond laser ablation of nickel in high vacuum. Applied Physics A: Materials Science and Processing. 89(4):1017-1024.

Amoruso, S., R. Bruzzese, X. Wang, N.N. Nedialkov, and P.A. Atanasov. 2007b. Femtosecond laser ablation of nickel in vacuum. Journal of Physics D: Applied Physics. 40:331-340.

Amoruso, S., R. Bruzzese, X. Wang, and J. Xia. 2008. Ultrafast laser ablation of metals with a pair of collinear laser pulses. Applied Physics Letters. 93:191504.1-191504.3.

Amoruso, S., R. Bruzzese, X. Wang, G. O'Connell, and J.G. Lunney. 2010. Multidiagnostic analysis of ultrafast laser ablation of metals with pulse pair irradiation. Journal of Applied Physics. 108:113302.1-113302.10.

Anabitarte, F., A. Cobo, and J.M. Lopez-Higuera. 2012. Laser-induced breakdown spectroscopy: fundamentals, applications, and challenges. International Scholarly Research Notices Spectroscopy. 2012:1–12.

Anisimov, S.I., B.L. Kapeliovich, and T.L. Perel'man. 1974. Electron emission from metal surfaces exposed to ultra short laser pulses. Soviet Physics - JETP. 39:375-377.

Anisimov, S.I, V.A. Gal'burt, M.F. Ivanov, I.E. Poyurovskaya, and V.I. Fisher. 1979. Analysis of the interaction of a laser beam with a metal. Soviet Physics - Technical Physics. 24:295-299.

Apostolova, T., and Y. Hahn. 2000. Modeling of laser-induced breakdown in dielectrics with subpicosecond pulses. Journal of Applied Physics. 88:1024-1034.

Atanasov, P.A., and N.N. Nedialkov. 2007. Influence of the processing parameters on the ultrashort laser ablation of metals. Proceedings of SPIE. 6346:63462Y.1-63462Y.6.

Axente, E., S. Noël, J. Hermann, M. Sentis, and I.N. Mihailescu. 2009. Subpicosecond laser ablation of copper and fused silica: Initiation threshold and plasma expansion. Applied Surface Science. 255:9734–9737.

Balachninait˙e, O., A. Baškevi˘cius, K. Stankeviciute, K. Kuršelis, and V. Sirutkaitis. 2010. Double-pulse laser-induced breakdown spectroscopy with 1030 and 257.5 nm wavelength femtosecond laser pulses. Lithuanian J. of Phys. 50, 1-5-110 (2010).

Balamane, H., T. Halicioglu, and W.A. Tiller. 1992. Comparative study of silicon empirical interatomic potentials. Physical Review B. 46:2250-2279.

Balling, P. and J. Schou. 2013. Femtosecond-laser ablation dynamics of dielectrics: basics and applications for thin films. Reports on Progress in Physics. 76:036502.1-036502.39.

Bashir, S., M.S. Rafique, and W. Husinsky. 2012. Identification of ultra-fast electronic and thermal processes during femtosecond laser ablation of Si. Applied Physics A: Materials Science & Processing. 109:421–429.

Bechtel, J.H., W. Lee Smith, and N. Bloembergen. 1977. Two-photon photoemission from metals induced by picosecond laser pulses. Physics Review B. 15:4557-4563.

Besner, S., J.Y. Degorce, A.V. Kabashin, and M. Meunier. 2005. Influence of ambient medium on femtosecond laser processing of silicon. Applied Surface Science. 247:163-168.

Besold, G., I. Vattulainen, M. Karttunen, and J.M. Polson. 2000. Towards better integrators for dissipative particle dynamics simulations. Physical Review E: Statistical Physics, Plasmas, Fluids, and Related Interdisciplinary Topics. 62(6):R7611-R7614.

Birdsall, C.K.. 1991. Particle-in-cell charged-particle simulations, plus Monte Carlo collisions with neutral atoms, PIC-MCC. IEEE Transactions on Plasma Science. 19(2):65-85.

Birdsall, C.K., and A.B. Langdon. 2005. Plasma physics via computer simulation. Taylor & Francis.

Born, M. and E. Wolf. 1970. Principles of Optics. fourth edition, Pergamon Press:Oxford.

Broughton, J.Q., and X.P. Li. 1987. Phase diagram of silicon by molecular dynamics. Physical Review B. 35:9120-9127.

Bulgakova, N.M., A.V. Bulgakov, and O.F. Bobrenok. 2000. Double layer effects in laser-ablation plasma plumes. Physical Review E: Statistical Physics, Plasmas, Fluids, and Related Interdisciplinary Topics. 62(4):5624-5635.

Bulgakova, N.M., R. Stoian, A. Rosenfeld, I.V. Hertel, and E.E.B. Campbell. 2004. Electronic transport and consequences for material removal in ultrafast pulsed laser ablation of materials. Physical Review B: Condensed Matter and Materials Physics. 69:054102.1-054102.12.

Bulgakova, N.M., R. Stoian, A. Rosenfeld, I.V. Hertel, and E.E.B. Campbell. 2005a. Surface charging under pulsed laser ablation of solids and its consequences: studies with a continuum approach. Proceedings of SPIE. 5714:9-23.

Bulgakova, N.M., R. Stoian, A. Rosenfeld, I.V. Hertel, W. Marine, and E.E.B. Campbell. 2005b. A general continuum approach to describe fast electronic transport in pulsed laser irradiated materials: The problem of Coulomb explosion. Applied Physics A: Materials Science and Processing. 81:345-356.

Bulgakova, N.M, A. Rosenfeld, L. Ehrentraut, R. Stoian, and I.V. Hertel. 2007. Modeling of electron dynamics in laser-irradiated solids: progress achieved through a continuum approach and future prospects. Proceedings of SPIE. 6732:673208.1-673208.15.

Bulgakova, N.M., V.P. Zhukov, A.Y. Vorobyev, and C. Guo. 2008. Modeling of residual thermal effect in femtosecond laser ablation of metals: role of a gas environment. Applied Physics A: Materials Science and Processing. 92(4):883-889.

Chen, J.K., D.Y. Tzou, and J.E. Beraun. 2005. Numerical investigation of ultrashort laser damage in semiconductors. International Journal of Heat and Mass Transfer. 48:501-509.

Chen, J.K., D.Y. Tzou, and J.E. Beraun. 2006. A semiclassical two-temperature model for ultrafast laser heating. International Journal of Heat and Mass Transfer. 49(1-2):307-316.

Chen, L.M., J. Zhang, Q.L. Dong, H. Teng, T.J. Liang, L.Z. Zhao, and Z.Y. Wei. 2001. Hot electron generation via vacuum heating process in femtosecond laser-solid interactions. Physics of Plasmas. 8(6):2925-2929.

Chen, Z., and S.S. Mao. 2008. Femtosecond laser-induced electronic plasma at metal surface. Applied Physics Letters. 93:051506.1-051506.3.

Cheng, C., and X. Xu. 2005. Mechanisms of decomposition of metal during femtosecond laser ablation. Physical Review B: Condensed Matter and Materials Physics. 72:165415.1-165415.15.

Chichkov, B.N., C. Momma, S. Nolte, F. von Alvensleben, and A. Tünnermann. 1996. Femtosecond, picosecond and nanosecond laser ablation of solids. Applied Physics A: Materials Science and Processing. 63(2):109-115.

Choi, T.Y., D.J. Hwang, and C.P. Grigoropoulos. 2002. Femtosecond laser induced ablation of crystalline silicon upon double beam irradiation. Applied Surface Science. 197-198:720-725.

Chowdhury, I.H., and X. Xu. 2005. Ultrafast double-pulse ablation of fused silica. Applied Physics Letters. 86:151110.1-151110.3.

Clark, E.L., K. Krushelnick, J.R. Davies, M. Zepf, M. Tatarakis, F.N. Beg, A. Machacek, P.A. Norreys, M.I.K. Santala, I. Watts, and A.E. Dangor. 2000. Measurements of energetic proton transport through magnetized plasma from intense laser interactions with solids. Physical Review Letters. 84:670–673.

Cogan, S., E. Shirman, and Y. Haas. 2005. Production efficiency of thin metal flyers formed by laser ablation. Journal of Applied Physics. 97:113508.1-113508.6.

Colombier, J.P., P. Combis, F. Bonneau, R. Le Harzic, and E. Audouard. 2005. Hydrodynamic simulations of metal ablation by femtosecond laser irradiation. Physical Review B: Condensed Matter and Materials Physics. 71:165406.1-165406.6.

Corsi, M., G. Cristoforetti, M. Giuffrida, M. Hidalgo, S. Legnaioli, V. Palleschi, A. Salvetti, E. Tognoni, and C. Vallebona. 2004. Three-dimensional analysis of laser induced plasmas in single and double pulse configuration. Spectrochimica Acta Part B: Atomic Spectroscopy. 59:723–735.

Cottrill, L.A., A. Kemp, M. Tabak, and R.P.J. Town. 2010. Characterization of escaping electrons from simulations of hot electron transport for intense femtosecond laser-target scenarios. Nuclear Fusion. 50(9):095002.1-095002.12.

Couairon, A., and A. Mysyrowicz. 2007. Femtosecond filamentation in transparent media. Physics Reports. 441(2-4):47-189.

Cowley, E.R.. 1988. Lattice dynamics of silicon with empirical many-body potentials. Physical Review Letters. 60:2379-2382.

Craighead, H.. 2006. Future lab-on-a-chip technologies for interrogating individual molecules. Nature. 442:387-393.

Dachraoui, H., and W. Husinsky. 2006a. Fast electronic and thermal processes in femtosecond laser ablation of Au. Applied Physics Letters. 89:104102.1-104102.3.

Dachraoui, H., and W. Husinsky. 2006b. Thresholds of plasma formation in silicon identified by optimizing the ablation laser pulse form. Physical Review Letters. 97:107601.1-107601.4.

Dachraoui, H., W. Husinsky, and G. Betz. 2006c. Ultra-short laser ablation of metals and semiconductors: evidence of ultra-fast Coulomb explosion. Applied Physics A: Materials Science and Processing. 83:333-336.

Davis, K.M., K. Miura, N. Sugimoto, and K. Hirao. 1996. Writing waveguides in glass with a femtosecond laser. Optics Letters. 21(21):1729-1731.

De Falco, S., Interaction laser femtoseconde-métal : étude expérimentale des mécanismes d'ablation et de formation des nanoparticules. 2008. PhD dissertation, Universitéde la Mediterranée (Aix-Marseille II).

Ding, P.J., Q.C. Liu, X. Lu, X.L. Liu, S.H. Sun, Z.Y. Liu, B.T. Hu, and Y.H. Li. 2012. Hydrodynamic simulation of silicon ablation by ultrashort laser irradiation. Nuclear Instruments and Methods in Physics Research B. 286:40-44.

Donnelly, T., J.G. Lunney, S. Amoruso, R. Bruzzese, X. Wang, and X. Ni. 2009. Double pulse ultrafast laser ablation of nickel in vacuum. Journal of Applied Physics. 106:013304.1-013304.5.

Dowden, J.. 2009. The Theory of Laser Materials Processing. Dordrecht: Springer.

Eidmann, K., J. Meyer-ter-Vehn, and T. Schlegel. 2000. Hydrodynamic simulation of subpicosecond laser interaction with solid-density matter. Physical Review E: Statistical Physics, Plasmas, Fluids, and Related Interdisciplinary Topics. 62(1):1202-1214.

Eland, K.L., D.N. Stratis, D.M. Gold, S.R. Goode, and S.M. Angel. 2001. Energy dependence of emission intensity and temperature in a libs plasma using femtosecond excitation. Applied Spectroscopy. 55(3):286-291.

Ellegaard, O., T. Nedelea, J. Schou, and H.M. Urbassekb. 2002. Plume expansion of a laser-induced plasma studied with the particle-in-cell method. Applied Surface Science. 197-198:229-238.

Fisher, D., M. Fraenkel, Z. Henis, E. Moshe, and S. Eliezer. 2001. Interband and intraband (Drude) contributions to femtosecond laser absorption in aluminum. Physical Review E: Statistical Physics, Plasmas, Fluids, and Related Interdisciplinary Topics. 65:016409.1-016409.8.

Fisher, D., M. Fraenkel, Z. Zinamon, Z. Henis, E. Moshe, Y. Horovitz, E. Luzon, S. Maman, and S. Eliezer. 2005. Interband and intraband absorption of femtosecond laser pulses in copper. Laser and Particle Beams. 23(03):391-393.

Fraenkel, M., A. Zigler, Z. Henis, S. Eliezer, and N. E. Andreev. 2000. Measurement of the Energy Penetration Depth into Solid Targets Irradiated by Ultrashort Laser Pulses. Physical Review E: Statistical Physics, Plasmas, Fluids, and Related Interdisciplinary Topics. 61:1899-1903.

Frenkel, D., and B. Smit. 2002. Understanding Molecular Simulation: From Algorithms to Applications. Academic Press.

Furusawa, K, K. Takahashi, H. Kumagai, K. Midorikawa, and M. Obara. 1999. Ablation characteristics of Au, Ag, and Cu metals using a femtosecond Ti:sapphire laser. Applied Physics A: Materials Science and Processing. 69:S359-S366.

Gale, J.D., and A.L. Rohl. 2003. The general utility lattice program (gulp). Molecular Simulation. 29(5):291–341.

Gamal, Y.E.E.-D., M.S.E.-D. Shafik and J.M. Daoud. 1999. Numerical investigation of the dependence of the threshold irradiance on the wavelength in laser-induced breakdown in N2. Journal of Physics D: Applied Physics. 32(4):423-429.

Gamaly, E.G. 2011. The physics of ultra-short laser interaction with solids at non-relativistic intensities. Physics Reports. 508:91-243.

Gan, Y., and J. K. Chen. 2011. Combined continuum-atomistic modeling of ultrashort-pulsed laser irradiation of silicon. Applied Physics A. 105:427-437.

Geindre, J.P., P. Audebert, A. Rousse, F. Fallies, and J.C. Gauthier. 1994. Frequency-domain interferometer for measuring the phase and amplitude of a femtosecond pulse probing a laser-produced plasma. Optics Letters. 19:1997-1999.

Gibbon, P., and A. R. Bell. 1992. Collisionless absorption in sharp-edged plasmas. Physical Review Letters. 68(10):1535-1538.

Ginzburg, V.L. 1962. Propagation of Electromagnetic Waves in Plasma. Gordon and Breach:New York.

Girardeau-Montaut, J.P. and C. Girardeau-Montaut. 1995. Theory of ultrashort nonlinear multiphoton photoelectric emission from metals. Physical Review B: Condensed Matter and Materials Physics. 51:13560-13567.

Gordienko, V.M., I.M. Lachko, A.A. Rusanov, A.B. Savelev, D.S. Uryupina, and R.V. Volkov. 2005. Enhanced production of fast multi-charged ions from plasmas formed at cleaned surface by femtosecond laser pulse. Applied Physics B. 80:733-739.

Grimes, M.K., A.R. Rundquist, Y.-S. Lee, and M.C. Downer. 1999. Experimental identification of "vacuum heating" at femtosecond-laser-irradiated metal surfaces. Physical Review Letters. 82(20):4010-4013.

Guo, C., G. Rodriguez, A. Lobad, and A.J. Taylor. 2000. Structural phase transition of aluminum induced by electronic excitation. Physical Review Letters. 84(19):4493-4496.

Hagiwara, Y., A. Hongo, and M. Obara. 2005. Ablation processing of biomedical materials with femtosecond double pulse lasers through hollow fiber. Proceedings of SPIE. 5714:283-289.

Hansen, C.T., S.C. Wilks, and P.E. Young. 1999. Spectral evidence for collisionless absorption in subpicosecond laser-solid interactions. Physical Review Letters. 83(24):5019-5022.

Harilal, S.S., P.K. Diwakar, and A. Hassanein. 2013. Electron-ion relaxation time dependent signal enhancement in ultrafast double-pulse laser-induced breakdown spectroscopy. Applied Physics Letters. 103:041102.1-041102.4.

Hebeisen, C.T., G. Sciaini, M. Harb, R. Ernstorfer, S.G. Kruglik, and R.J.D. Miller. 2008. Direct visualization of charge distributions during femtosecond laser ablation of a Si (100) surface. Physical Review B: Condensed Matter and Materials Physics. 78:081403(R).1-081403(R).4.

Herring, C., and M.H. Nichols. 1949. Thermionic Emission. Review of Modern Physics. 21(2):185-270.

Hile, C.V.. 1996. Comparisons between Maxwell's equations and an extended nonlinear Schrodinger equation. Wave Motion. 24(1):1-12.

Hora, H.. 1975. Theory of relativistic self-focusing of laser radiation in plasmas. Journal of the Optical Society of America. 65(8):882-886.

Hou, Z., Z. Wang, J. Liu, W. Ni, and Z. Li. 2013. Signal quality improvement using cylindrical confinement for laser induced breakdown spectroscopy. Optics Express. 21:15974-15979.

Hu, W., Y. Shin, and G. King. 2010. Energy transport analysis in ultrashort pulse laser ablation through combined molecular dynamics and Monte Carlo simulation. Physical Review B: Condensed Matter and Materials Physics. 82:094111.1-094111.12.

Hu, W., Y. Shin, and G. King. 2011a. Early-stage plasma dynamics with air ionization during Ultrashort laser ablation of metal. Physics of Plasmas. 18:093302.1-093302.12.

Hu, W., Y. Shin, and G. King. 2011b. Effect of air breakdown with a focusing lens on ultrashort laser ablation. Applied Physics Letters. 99:234104.1-234104.3.

Hu, W., Y. Shin, and G. King. 2012. Characteristics of plume plasma and its effects on ablation depth during ultrashort laser ablation of copper in air. Journal of Physics D: Applied Physics. 45:355204.1-355204.8.

Hu, Z., S. Singha, Y. Liu, and R.J. Gordon. 2007. Mechanism of the ablation of Si<111> with pairs of ultrashort laser pulses. Applied Physics Letters. 90: 131910.1-131910.3.

Huttner, B.. 1994. Optical properties of polyvalent metals in the solid and liquid state: aluminium. Journal of Physics: Condensed Matter. 6(13):2459-2474.

Hwang, D.J., C.P. Grigoropoulos, and T.Y. Choi. 2006. Efficiency of silicon micromachining by femtosecond laser pulses in ambient air. Journal of Applied Physics. 99:083101.1-083101.6.

Inogamov, N.A., S.I. Anisimov, Yu.V. Petrov, V.A., Khokhlov, V.V. Zhakhovskii, K. Nishihara, M.B. Agranat, S.I. Ashitkov, and P.S. Komarov. 2008. Theoretical and experimental study of hydrodynamics of metal target irradiated by ultrashort laser pulse. Proceedings of the SPIE - The International Society for Optical Engineering. 7005:70052F.1-70052F.10.

Itina, T.E., J. Hermann, Ph. Delaporte, and M. Sentis. 2004. Modeling of metal ablation induced by ultrashort laser pulses. Thin Solid Films. 453:513-517.

Itzkan, I., D. Albagli, M.L. Dark, L.T. Perelman, C. Von Rosenberg, and M.S. Feld. 1995. The thermoelastic basis of short pulsed laser ablation of biological tissue. Proceedings of the National Academy of Sciences of the United States of America. 92:1960-1964.

Ivanov, D.S., and L.V. Zhigilei. 2003. Combined atomistic-continuum modeling of short-pulse laser melting and disintegration of metal films. Physical Review B: Condensed Matter and Materials Physics. 68(6):064114.1-064114.22.

Kanavin, A.P., I.V. Smetanin, V.A. Isakov, Yu.V. Afanasiev, B.N. Chichkov, B. Wellegehausen, S. Nolte, C. Momma, and A. Tünnermann. 1998. Heat transport in metals irradiated by ultrashort laser pulses. Physical Review B. 57(23):14698-14703.

Keldysh, L.V.. 1964. Ionizatsiya v pole sil'noi elektromagnitnoi volny (Ionization in field of strong electromagnetic wave). Zhurnal Eksperimental'noi i Teoreticheskoi Fiziki. 47(5):1945-1957.

Kelly, R., and A. Miotello. 1996. Comments on explosive mechanisms of laser sputtering. Applied Surface Science. 96-98:205-215.

Key, M.H.. 2001. Fast track to fusion energy. Nature 412:775-756.

Khishchenko, K.V., M.E. Veysman, N.E. Andreev, V.E. Fortov, P.R. Levashov, and M.E. Povarnitsyn. 2008. Modeling of optical, transport, and thermodynamic properties of Al metal irradiated by intense femtosecond laser pulses. Proceedings of SPIE. 7005:70051S.1-70051S.8.

Kim, J., and S. Na. 2007. Metal thin film ablation with femtosecond pulsed laser. Optics and Laser Technology. 39(7):1443-1448.

Kim, K.Y., B. Yellampalle, J.H. Glownia, A.J. Taylor, and G. Rodriguez. 2008. Measurements of terahertz electrical conductivity of intense laser-heated dense aluminum plasmas. Physical Review Letters. 100:135002.1-135002.4.

Kodama, R. H. Shiraga, K. Shigemori, Y. Toyama, S. Fujioka, H. Azechi, H. Fujita, H. Habara, T. Hall, Y. Izawa, T. Jitsuno, Y. Kitagawa, K. M. Krushelnick, K. L. Lancaster, K. Mima, K. Nagai, M. Nakai, H. Nishimura, T. Norimatsu, P. A. Norreys, S. Sakabe, K. A. Tanaka, A. Youssef, M. Zepf, and T. Yamanaka. 2002. Nuclear fusion: Fast heating scalable to laser fusion ignition. Nature. 418:933-934.

Komarov, P.S., S.I. Ashitkov, A.V. Ovchinnikov, D.S. Sitnikov, M.E. Veysman, P.R. Levashov, M.E. Povarnitsyn, M.B. Agranat, N.E. Andreev, K.V. Khishchenko, and V.E. Fortov. 2009. Experimental and theoretical study of Al plasma under femtosecond laser pulses. Journal of Physics A: Mathematical and Theoretical. 42:214057.1-214057.4.

Komashko, A.M., M.D. Feit, A.M. Rubenchik, M.D. Perry, and P.S. Banks. 1999. Simulation of material removal efficiency with ultrashort laser pulses. Applied Physics A. 69:S95-S98.

Konstantin, V., K.V. Khishchenko, M.E. Veysman, N.E. Andreev, V.E. Fortov, P.R. Levashov, and M.E. Povarnitsyn. 2008. Modeling of optical, transport, and thermodynamic properties of Al metal irradiated by intense femtosecond laser pulses. Proceedings of SPIE. 7005:70051S.1-70051S.8.

Koudoumas, E., M. Spyridaki, R. Stoian, A. Rosenfeld, P. Tzanetakis, I.V. Hertel, and C. Fotakis. 2004. Influence of pulse temporal manipulation on the properties of laser ablated Si ion beams. Thin Solid Films. 453–454:372-376.

Laville, S., F. Vidal, T.W. Johnston, O. Barthelemy, M. Chaker, B.L. Drogoff, J. Margot, and M. Sabsabi. 2002. Fluid modeling of the laser ablation depth as a function of the pulse duration for conductors. Physical Review E: Statistical Physics, Plasmas, Fluids, and Related Interdisciplinary Topics. 66:066415.1-066415.7.

Le Harzic, R., D. Breitling, M. Weikert, S. Sommer, C. Föhl, F. Dausinger, S. Valette, C. Donnet, and E. Audouard. 2005a. Ablation comparison with low and high energy densities for Cu and Al with ultra-short laser pulses. Applied Physics A. 80:1589-1593.

Le Harzic, R., D. Breitling, S. Sommer, C. Fohl, K. Konig, F. Dausinger, and E. Audouard. 2005b. Processing of metals by double pulses with short laser pulses. Applied Physics A. 81:1121–1125.

Lee, S., D. Yang, and S. Nikumb. 2008. Femtosecond laser micromilling of Si wafers. Applied Surface Science. 254:2996-3005.

Lenner, M., A. Kaplan, and R.E. Palmer. 2007. Nanoscopic Coulomb explosion in ultrafast graphite ablation. Applied Physics Letters. 90:153119.1-153119.3.

Li, K.D., and P.M. Fauchet. 1987. Drude parameters of liquid silicon at the melting temperature. Applied Physics Letters. 51:1747-1749.

Li, P., and S. Chu. 2013. High-order-harmonic generation of Ar atoms in intense ultrashort laser fields: An all-electron time-dependent density-functional approach including macroscopic propagation effects. Physical Review A. 88:053415.1-053415.6.

Lima, M.B.S., C.A.S. Lima, and L.C.M. Miranda. 1979. Screening effect on the plasma heating by inverse bremsstrahlung. Physical Review A. 19:1796-1800.

Lin, X., J. Yanga, Y. Suna, and S. Jianga. 2009. Ultra-short laser ablation of dielectrics: Theoretical analysis of threshold damage fluence and ablation depth. Applied Surface Science. 256:130-135.

Liu, X., and S. Osher. 1998. Convex ENO High Order Multi-dimensional Schemes without Field by Field Decomposition or Staggered Grids. Journal of Computational Physics. 142:304-330.

Liu, X., S. Sun, X. Wang, Z. Liu, Q. Liu, P. Ding, Z. Guo and B. Hu. 2013. Effect of laser pulse energy on orthogonal double femtosecond pulse laser-induced breakdown spectroscopy. Optics Express. 21:A704-A713.

Loir, A.S.. 2003. Study of plasma expansion induced by femtosecond pulsed laser ablation and deposition of diamond-like carbon films. Applied Surface Science. 208-209:553-560.

Lorazo, P., L.J. Lewis, and M. Meunier. 2003. Short-Pulse Laser Ablation of Solids: From Phase Explosion to Fragmentation. Physical Review Letters. 91:225502.1-225502.4.

Lorazo, P., L.J. Lewis, and M. Meunier. 2006. Thermodynamic pathways to melting, ablation, and solidification in absorbing solids under pulsed laser irradiation. Physical Review B: Condensed Matter and Materials Physics. 73(13):134108.1-134108.22.

MacDonald, A.H.. 1980. Electron-phonon enhancement of electron-electron scattering in Al. Physical Review Letters. 44(7):489-493.

Mao, S.S., X. Mao, R. Greif, and R.E. Russo. 1998. Simulation of infrared picosecond laser-induced electron emission from semiconductors. Applied Surface Science. 127-129:206-211.

Mao, S.S., X. Mao, R. Greif, and R.E. Russo. 2000a. Simulation of a picosecond laser ablation plasma. Applied Physics Letters. 76(23):3370-3372.

Mao, S.S., X. Mao, R. Greif, and R.E. Russon. 2000b. Initiation of an early-stage plasma during picosecond laser ablation of solids. Applied Physics Letters. 77(16):2464-2466.

Mao, S.S., F. Quéré, S. Guizard, X. Mao, R.E. Russo, G. Petite, and P. Martin. 2004. Dynamics of femtosecond laser interactions with dielectrics. Applied Physics A: Materials Science and Processing. 79:1695-1709

Margetic, V., A. Pakulev, A. Stockhaus, M. Bolshov, K. Niemax, and R. Hergenroder. 2000. A comparison of nanosecond and femtosecond laser-induced plasma spectroscopy of brass samples. Spectrochimica Acta Part B: Atomic Spectroscopy. 55:1771–1785.

Marshall, G.D., M. Ams, and M.J. Withford. 2006. Direct laser written waveguide Bragg gratings in bulk fused silica. Optics Letters. 31:2690-2691.

Mildner, J., C. Sarpe, N. Gotte, M. Wollenhaupt, and T. Baumert. 2013. Emission signal enhancement of laser ablation of metals (aluminum and titanium) by time delayed femtosecond double pulses from femtoseconds to nanoseconds. Applied Surface Science. 302:291-298.

Minoshima, K., A.M. Kowalevicz, E.P. Ippen, and J.G. Fujimoto. 2002. Fabrication of coupled mode photonic devices in glass by nonlinear femtosecond laser materials processing. Optical Express. 10:645-652.

Miotello, A., and R. Kelly. 1995. Critical-assessment of thermal models for laser sputtering at high fluences. Applied Physics Letters. 67:3535-3537.

Miotello, A., and R. Kelly. 1999. Laser-induced phase explosion: new physical problems when a condensed phase approaches the thermodynamic critical temperature. Applied Physics A: Materials Science and Processing. 69:S67-S73.

Miura, E., H. Honda, K. Katsura, E. Takahashi, and K. Kondo. 2000. X-ray emissions from clusters excited by ultrashort laser pulses. Proceedings of SPIE. 3886:320-330.

Miura, K., J. Qiu, H. Inouye, T. Mitsuyu, and K. Hirao. 1997. Photowritten optical waveguides in various glasses with ultrashort pulse laser. Applied Physics Letters. 71:3329-3331.

Momma, C., S. Nolte, B.N. Chichkov, F.V. Alvensleben, and A. Tünnermann. 1997. Precise laser ablation with ultrashort pulses. Applied Surface Science. 109/110:15-19.

More, R.M., K.H. Warren, D.A. Young, and G.B. Zimmerman. 1988. A new quotidian equation of state (QEOS) for hot dense matter. Physics of Fluids. 31:3059-3078.

Mueller, B.Y., and B. Rethfeld. 2013. Relaxation dynamics in laser-excited metals undernonequilibrium conditions. Physical Review B. 87:035139.1–035139.12.

Nanbu, K.. 2000. Probability theory of electron-molecule, ion-molecule, molecule-molecule, and Coulomb collisions for particle modeling of materials processing plasmas and cases. IEEE Transactions on Plasma Science. 28(3):971-990.

Nedelea, T., and H.M. Urbassek. 2004. Parametric study of ion acceleration in a one-dimensional plasma expansion using the particle-in-cell simulation. Physical Review E: Statistical Physics, Plasmas, Fluids, and Related Interdisciplinary Topics. 69:056408.1-056408.8.

Nedialkov, N.N., S.E. Imamova, P.A. Atanasov, G. Heusel, D. Breitling, A. Ruf, H. Hugel, F. Dausinger, and P. Berger. 2004a. Laser ablation of iron by ultrashort laser pulses. Thin Solid Films. 453-454:496-500.

Nedialkov, N.N.. 2004b. Dynamics of the ejected material in ultra-short laser ablation of metals. Applied Physics A: Materials Science and Processing. 79:1121-1125.

Nedialkov, N.N., P.A. Atanasov, D. Breitling, G. Heusel, and F. Dausinger. 2005a. Ablation of metals by ultrashort laser pulses. Proceedings of SPIE. 5830:80-84.

Nedialkov, N.N., S.E. Imamova, P.A. Atanasov, P. Berger, and F. Dausinger. 2005b. Mechanism of ultrashort laser ablation of metals: molecular dynamics simulation. Applied Surface Science. 247:243-248.

Noël, S., and J. Hermann. 2007. Influence of irradiation conditions on plume expansion induced by femtosecond laser ablation of gold and copper. Proceedings of SPIE. 6785:67850F.1-67850F.8.

Nolte, S., C. Momma, H. Jacobs, A. Tünnermann, B.N. Chichkov, B. Wellegehausen, and H. Welling. 1997. Ablation of metals by ultrashort laser pulses. Journal of the Optical Society America B. 14:2716-2722.

Nolte, S., M. Will, J. Burghoff, and A. Tuennermann. 2003. Femtosecond waveguide writing: a new avenue to three-dimensional integrated optics. Applied Physics A: Materials Science and Processing. 77:109–111.

Noya, J.C., C.P. Herrero, and R. Ramírez. 1996. Thermodynamic properties of c-Si derived by quantum path-integral Monte Carlo simulations. Physical Review B. 53:9869-9875.

Pedrotti, F.L., and L.S. Pedrotti. 1993. Introduction to Optics. Englewood Cliffs/Prentice Hall.

Penczak, J., R. Kupfer, I. Bar, and R.J. Gordon. 2014. The role of plasma shielding in collinear double-pulse femtosecond laser-induced breakdown spectroscopy. Spectrochimica Acta Part B: Atomic Spectroscopy. 97:34-41.

Perelomov, A.M., V.S. Popov, and M.V. Terentiev. 1966. Ionization of atoms in an alternating electric field. Zhurnal Eksperimental'noi i Teoreticheskoi Fiziki(Soviet Physics - JETP). 50(5):1393-1409(23:924-934).

Perez, D., and L.J. Lewis. 2002. Ablation of solids under femtosecond laser pulses. Physical Review Letters. 89:255504.1-255504.4.

Perez, D., and L.J. Lewis. 2003. Molecular-dynamics study of ablation of solids under femtosecond laser pulses. Physical Review B: Condensed Matter and Materials Physics. 67:184102.1-184102.15.

Perez, D. and L.J. Lewis. 2004. Thermodynamic evolution of materials during laser ablation under pico and femtosecond pulses. Applied Physics A: Materials Science and Processing. 79:987-990.

Perez, D., L.K. Béland, D. Deryng, L.J. Lewis, and M. Meunier. 2008. Numerical study of the thermal ablation of wet solids by ultrashort laser pulses. Physical Review B. 77:014108.1-014108.9.

Petek, H., H. Nagano, M.J. Weida, and S. Ogawa. 2000. The role of Auger decay in hot electron excitation in copper. Chemical Physics. 251:71-86.

Phuoc, T.X.. 2000. Laser spark ignition: experimental determination of laser-induced breakdown thresholds of combustion gases. Optics Communications. 175(4-6)419:423.

Piñon, V., and D. Anglos. 2009. Optical emission studies of plasma induced by single and double femtosecond laser pulses. Spectrochimica Acta Part B: Atomic Spectroscopy. 64:950-960.

Plyutto, A.A.. 1961. Acceleration of positive ions in expansion of the plasma in a vacuum spark. Soviet Physics – JETP. 12(6):1106-1108.

Povarnitsyn, M.E., T.E. Itina, M. Sentis, K.V. Khishchenko, and P.R. Levashov. 2007. Material decomposition mechanisms in femtosecond laser interactions with metals. Physical Review B. 75:235414.1-235414.5.

Povarnitsyn, M.E., T.E. Itina, K.V. Khishchenko, and P.R. Levashov. 2009. Suppression of ablation in femtosecond double-pulse experiments. Physical Review Letters. 103:195002.1-195002.4.

Povarnitsyn, M.E., T.E. Itina, P.R. Levashov, and K.V. Khishchenko. 2011. Simulation of ultrashort double-pulse laser ablation. Applied Surface Science. 257(12):5168-5171.

Price, D.F., R.M. More, R.S. Walling, G. Guethlein, R.L. Shepherd, R.E. Stewart, and W.E. White. 1995. Absorption of ultrashort laser pulses by solid targets heated rapidly to temperatures 1–1000 eV. Physical Review Letters. 75(2):252-255.

Psaltis, D., S.R. Quake, and C. Yang. 2006. Developing optofluidic technology through the fusion of microfluidics and optics. Nature. 442:381-386.

Qiu, T.Q., and C.L. Tien. 1993. Heat transfer mechanisms during short-pulse laser heating of metals. Transaction of the ASME, Journal of Heat Transfer. 115(4):835-841.

Reif, J., F. Costache, S. Eckert, and M. Henyk. 2004. Mechanisms of ultra-short laser pulse ablation from ionic crystals. Applied Physics A: Materials Science and Processing. 79:1229-1231.

Rethfeld, B., K. Sokolowski-Tinten, D. von der Linde, and S.I. Anisimov. 2004. Timescales in the response of materials to femtosecond laser excitation. Applied Physics A: Materials Science and Processing. 79:767-769.

Roeterdink, W.G., L.B. Juurlink, O.P. Vaughan, J.D. Diez, M. Bonn, and A.W. Kleyn. 2003. Coulomb explosion in femtosecond laser ablation of Si (111). Applied Physics Letters. 82:4190-4192.

Roeterdink, W.G., M. Bonn, and A.W. Kleyn. 2004. Response to "Comment on 'Coulomb explosion in femtosecond laser ablation of Si (111)'" [Appl. Phys. Lett. 85, 694 (2004)]. Applied Physics Letters. 85:696.

Rousse, A., K.T. Phuoc, R. Shah, A. Pukhov, E. Lefebvre, V. Malka, S. Kiselev, F. Burgy, J. Rousseau, D. Umstadter, and D. Hulin. 2004. Production of a keV X-Ray Beam from Synchrotron Radiation in Relativistic Laser-Plasma Interaction. Physical Review Letters. 93:135005.1-135005.4.

Savolainen, J-M., M.S. Christensen, and P. Balling. 2011. Material swelling as the first step in the ablation of metals by ultrashort laser pulses. Physical Review B: Condensed Matter and Materials Physics. 84:193410.1-193410.4.

Scaffidi, J., J. Pender, W. Pearman, S.R. Goode, B.W. Colston Jr., J.C. Carter, and S.M. Angel. 2003. Dual-pulse laser-induced breakdown spectroscopy with combinations of femtosecond and nanosecond laser pulses. Applied Optics. 42(30):6099-6106.

Scaffidi, J., S.M. Angel, and D.A. Cremers. 2006. Emission enhancement mechanisms in dual-pulse LIBS. Analytical Chemistry. 78:24–32.

Schäfer, C., H.M. Urbassek, and L.V. Zhigilei. 2002. Metal ablation by picosecond laser pulses: A hybrid simulation. Physical Review B: Condensed Matter and Materials Physics. 66(11):115404.1-115404.8.

Scuderi, D., O. Albert, D. Moreau, P.P. Pronko, and J. Etchepare. 2005. Interaction of a laser-produced plume with a second time delayed femtosecond pulse. Applied Physics Letters. 86:071502.1-071502.2.

Sebenne, C., D. Bolmont, G. Guichar, and M. Balkanski. 1975. Surface states from photoemission threshold measurements on a clean, cleaved, Si (111) surface. Physical Review B: Condensed Matter and Materials Physics. 12:3280-3285.

Seely, J.F., and E.G. Harris. 1973. Heating of a plasma by multiphoton inverse bremsstrahlung. Physical Review A. 7(3):1064-1067.

Semerok, A., and C. Dutouquet. 2004. Ultrashort double pulse laser ablation of metals. Thin Solid Films. 453–454:501–505.

Serikov, V.V., S. Kawamoto, and K. Nanbu. 1999. Particle-in-cell plus direct simulation Monte Carlo (PIC-DSMC) approach for self-consistent plasma-gas simulations. IEEE Transactions on Plasma Science. 27(5):1389-1398.

Silva, L.O., M. Marti, J. R. Davies, R.A. Fonseca, C. Ren, F.S. Tsung, and W.B. Mori. 2004. Proton Shock Acceleration in Laser-Plasma Interactions. Physical Review Letters. 92:015002.1-015002.4.

Silvestrelli, P.L., A. Alavi, M. Parrinello, and D. Frenkel. 1996. Ab initio molecular dynamics simulation of laser melting of silicon. Physical Review Letters. 77:3149-3152.

Singha, S., Z. Hu, and R. Gordon. 2008. Ablation and plasma emission produced by dual femtosecond laser pulses. Journal of Applied Physics. 104:113520.1-113520.10.

Sivakumar, M., B. Tan, and K. Venkatakrishnan. 2010. Enhancement of silicon nanostructures generation using dual wavelength double pulse femtosecond laser under ambient condition. Journal of Applied Physics. 107:044307.1-044307.3.

Sokolowski-Tinten, K., J. Bialkowski, A. Cavalleri, and D. von der Linde. 1998. Transient states of matter during short pulse laser ablation. Physical Review Letters. 81(1):224-227.

Spitzer, L., and R. Haem. 1953. Transport phenomena in a completely ionized gas. Physical Review. 89:977-981.

Sprangle, P., J.R. Peñano, and B. Hafizi. 2002. Propagation of intense short laser pulses in the atmosphere. Physical Review E: Statistical, Nonlinear, and Soft Matter Physics. 66(4):046418.1-046418.21.

Spyridaki, M., E. Koudoumas, P. Tzanetakis, C. Fotakis, R. Stoian, A. Rosenfeld, and I.V. Hertel. 2003. Temporal pulse manipulation and ion generation in ultrafast laser ablation of silicon. Applied Physics Letters. 83(7):1474-1476.

Stillinger, F.H., and T.A. Weber. 1985. Computer simulation of local order in condensed phases of silicon. Physical Review B. 31:5262-5271.

Stoian, R., D. Ashkenasi, A. Rosenfeld, and E.E.B. Campbell. 2000. Coulomb explosion in ultrashort pulsed laser ablation of Al_2O_3. Physical Review B: Condensed Matter and Materials Physics. 62(19):13167-13173.

Stoian, R., A. Rosenfeld, D. Ashkenasi, I.V. Hertel, N.M. Bulgakova, and E.E.B. Campbell. 2002. Surface charging and impulsive ion ejection during ultrashort pulsed laser ablation. Physical Review Letters. 88:097603.1-097603.1.

Stoian, R., A. Rosenfeld, I.V. Hertel, N.M. Bulgakova, and E.E.B. Campbell. 2004. Comment on "Coulomb explosion in femtosecond laser ablation of Si (111)" [Appl. Phys. Lett. 82, 4190 (2003)]. Applied Physics Letters. 85:694-695.

Stuart, B.C., M.D. Feit, S. Herman, A.M. Rubenchik, B.W. Shore, and M.D. Perry. 1996. Nanosecond-to-femtosecond laser-induced breakdown in dielectrics. Physical Review B: Condensed Matter and Materials Physics. 53:1749-1761.

Sudrie, L., A. Couairon, M. Franco, B. Lamouroux, B. Prade, S. Tzortzakis, and A. Mysyrowicz. 2002. Femtosecond laser-induced damage and filamentary propagation in fused silica. Physical Review Letters. 89:186601.1-186601.4.

Sundaram, S.K., and E. Mazur. 2002. Inducing and probing non-thermal transitions in semiconductors using femtosecond laser pulses. Nature Materials. 1:217-224.

Talebpour, A., J. Yang, and S.L. Chin. 1999. Semi-empirical model for the rate of tunnel ionization of N2 and O2 molecule in an intense Ti:sapphire laser pulse. Optics Communications. 163(1):29-32.

Tas, M.A., E.M. van Veldhuizen, and W.R. Rutgers. 1997. Plasma excitation processes in flue gas simulated with Monte Carlo electron dynamics. Journal of Physics D: Applied Physics. 30(11):1636-1645.

Toxvaerd, S.. 1998. Fragmentation of fluids by molecular dynamics. Physical Review E: Statistical, Nonlinear, and Soft Matter Physics. 58(1):704-712.

Turcu, I.C.E., M.C. Gower, and P. Huntington. 1997. Measurement of KrF laser breakdown threshold in gases. Optics Communications. 134(1-6):66-68.

Tzou, D.Y.. 1995. A unified field approach for heat conduction from micro- to macro-scales. Transaction of the ASME, Journal of Heat Transfer. 117(1):8-16.

Van Driel, H.M.. 1987. Kinetics of high-density plasmas generated in Si by 1.06- and 0.53-μm picosecond laser pulses. Physical Review B: Condensed Matter and Materials Physics. 35:8166-8176.

Vasileska, D., and S.M. Goodnick. 2006. Computational Electronics. Morgan and Claypool Publishers.

Veysman, M.E., M.B. Agranat, N.E. Andreev, S.I. Ashitkov, V.E. Fortov, K.V. Khishchenko, O.F. Kostenko, P.R. Levashov, A.V. Ovchinnikov, and D.S. Sitnikov. 2008. Femtosecond optical diagnostics and hydrodynamic simulation of Ag plasma created by laser irradiation of a solid target. Journal of Physics B: Atomic, Molecular and Optical Physics. 41:125704.1-125704.9.

Vidal, F., T.W. Johnston, S. Laville, O. Barthélemy, M. Chaker, B. Le Drogoff, J. Margot, and M. Sabsabi. 2001. Critical-point phase separation in laser ablation of conductor. Physical Review Letters. 86:2573-2576.

Vinogradov, A.V. and F.S. Faĭzullov. 1977. Role of many-photon and impact ionization in the breakdown of dielectrics by picosecond laser pulses. Soviet Journal of Quantum Electronics. 7:650-652.

Vorobyev, A.Y., and C. Guo. 2005. Direct observation of enhanced residual thermal energy coupling to solids in femtosecond laser ablation. Applied Physics Letters. 86:011916.1-011916.3.

Wan, D.P., J. Wang, and P. Mathew. 2011. Energy deposition and non-thermal ablation in femtosecond laser grooving of silicon. Machining Science and Technology. 15:263-283.

Wang, Z., Z. Hou, S.L. Lui, D. Jiang, J. Liu, and Z. Li. 2012. Utilization of moderate cylindrical confinement for precision improvement of laser-induced breakdown spectroscopy signal. Optics Express. 20:A1011–A1018.

Weng, Y., and M.J. Kushner. 1990. Method for including electron-electron collisions in Monte Carlo simulations of electron swarms in partially ionized gases. Physical Review A: Statistical Physics, Plasmas, Fluids, and Related Interdisciplinary Topics. 42(10):6192-6200.

Whitesides, G.M.. 2006. The origins and the future of microfluidics. Nature. 442:368-373.

Wojakowski, B., O. Suttmann, U. Klug, and R. Kling. 2009. Micromachining with picosecond double pulses on silicon and aluminum. Proceedings of SPIE. 7202, 72020O.1-72020O.10.

Wu, B., and Y.C. Shin. 2006. Modeling of nanosecond laser ablation with vapor plasma formation. Journal of Applied Physics. 99(8):084310.1-084310.8.

Wu, B., and Y.C. Shin. 2007a. A simple model for high fluence ultra-short pulsed laser metal ablation. Applied Surface Science. 253(8):4079-4084.

Wu, B., and Y.C. Shin. 2007b. Two dimensional hydrodynamic simulation of high pressures induced by high power nanosecond laser-matter interactions under water. Journal of Applied Physics. 101(10):103514.1-103514.8.

Wu, B., Y.C. Shin, H. Pakhal, N.M. Laurendeau, and R.P. Lucht. 2007c. Modeling and experimental verification of plasmas induced by high-power nanosecond laser-aluminum interactions in air. Physical Review E: Statistical, Nonlinear, and Soft Matter Physics. 76(2):026405.1-026405.8.

Wu, B., and Y.C. Shin. 2009. A simplified predictive model for high-fluence ultra-short pulsed laser ablation of semiconductors and dielectrics. Applied Surface Science. 255(9):4996-5002.

Yang, J., Y. Zhao, N. Zhang, Y. Liang, and M. Wang. 2007. Ablation of metallic targets by high-intensity ultrashort laser pulses. Physical Review B: Condensed Matter and Materials Physics. 76:165430.1-165430.10.

Yen, R., J. Liu, and N. Bloembergen. 1980. Thermally assisted multiphoton photoelectric emission from tungsten. Optics Communications. 35:277-282.

Zavestovskaya, I.N., O.A. Glazov, and N.A. Menkova. 2007. High power and ultrashort laser pulse ablation of metals: threshold characteristics. Proceedings of SPIE. 6735:673512.1-673512.8.

Zel'dovich, Y.B., and Y.P. Raizer. 2002. Physics of Shock Waves and High-Temperature Hydrodynamic Phenonmena. Dover Publications.

Zeng, X., X.L. Mao, R. Greif, and R.E. Russo. 2005. Experimental investigation of ablation efficiency and plasma expansion during femtosecond and nanosecond laser ablation of silicon. Applied Physics A: Materials Science and Processing. 80(2):237-241.

Zhakhovskii, V.V. , N.A. Inogamov, Yu.V. Petrov, S.I. Ashitkov, and K. Nishihara. 2009. Molecular dynamics simulation of femtosecond ablation and spallation with different interatomic potentials. Applied Surface Science. 255(24):9592-9596.

Zhang, H., D. van Oosten, D.M. Krol, and J.I. Dijkhuis. 2011. Saturation effects in femtosecond laser ablation of silicon-on-insulator. Applied Physics Letters. 99:231108.1-231108.3.

Zhao, X., and Y.C. Shin. 2010. Femtosecond laser drilling of high-aspect ratio microchannels in glass. Applied Physics A: Materials Science and Processing. 104(2):713-739.

Zheng, H.Y., Y.Z. Deng, S.R. Vatsya, and S.K. Nikumb. 2007. A study of balancing the competing effects of ultrashort laser induced plasma for optimal laser machining. Applied Surface Science. 253(7):3408-3412.

Zhigilei, L.V., and B.J. Garrison. 2000. Microscopic mechanisms of laser ablation of organic solids in the thermal and stress confinement irradiation regimes. Journal of Applied Physics. 88:1281-1298.

Zhigilei, L.V.. 2003. Dynamics of the plume formation and parameters of the ejected clusters in short-pulse laser ablation. Applied Physics A: Materials Science and Processing. 76:339-350.

Zhigilei, L.V., and D.S. Ivanov. 2005. Channels of energy redistribution in short-pulse laser interactions with metal targets. Applied Surface Science. 248(1-4):433-439.

Zhou, J., J. Peatross, M.M. Murnane, H.C. Kapteyn, and I.P. Christov. 1996. Enhanced high-harmonic generation using 25 fs laser pulses. Physical Review Letters. 76:752-755.

VITA

VITA

Xin Zhao was born in Yantai, Shandong Province, People's Republic of China. He graduated from Tsinghua University (Beijing, China) with B.S. degree in Physics in 2006 and M.S. degree in Physics in 2008. He joined the School of Mechanical Engineering, Purdue University in 2008, and is currently a Ph.D. candidate in Mechanical Engineering.

His research at Purdue under the direction of Prof. Yung C. Shin focuses on ultrashort laser-matter interaction, laser-induced plasma dynamics, laser-plasma interaction, ultrashort laser micro-machining, ultra-fast pulse laser ablation, continuum/atomistic level simulation, and precision optics.